REPORT No. 36

STALL PROPAGATION

IN A

CASCADE OF

AIRFOILS

A. R. KRIEBEL
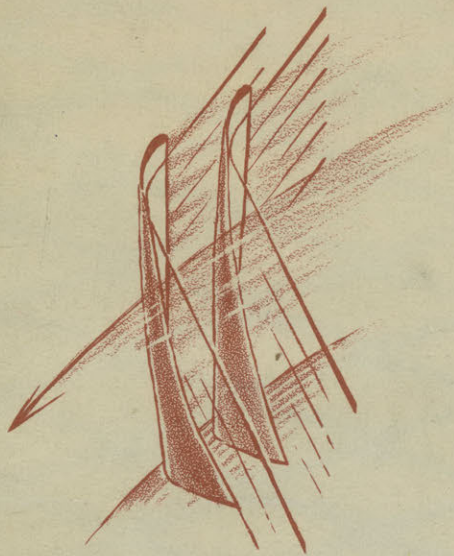
August, 1956

GAS TURBINE LABORATORY

MASSACHUSETTS INSTITUTE OF TECHNOLOGY

CAMBRIDGE · 39 · MASSACHUSETTS

STALL PROPAGATION IN A CASCADE OF AIRFOILS

Anthony R. Kriebel

Gas Turbine Laboratory

Report Number 36

August 1956

Massachusetts Institute of Technology

ACKNOWLEDGMENTS

TABLE OF CONTENTS

ABSTRACT

An experimental investigation of stall propagation in a stationary circular cascade by means of high speed schlieren and interferometer photography is described. This investigation suggests an analytical approach to the problem which is valid only for an isolated blade row in an infinite flow field but which is not restricted to small unsteady perturbations or an assumed simplified cascade geometry. Conditions necessary for the existence of the assumed type of stall cells are described and equations are derived for the velocity of stall cell propagation.

The propagation velocities predicted for the theoretical potential-flow model correlate with all the experimental values measured in an isolated rotor within 15%.

Analysis of the flow model predicts a tendency for the assumed type of stall cell to split with increasing incidence of the mean flow through the blade row which appears to correlate with the experimental observation of a trend for increasing numbers of cells in the rotor.

1 Introduction

The objective of the analytical and experimental work presented herein is the development of a theory which will enable one to predict the flow through a cascade of rigid airfoils, or an isolated blade row of an axial compressor, when the incidence of the fluid on the airfoils is high. It was discovered in the early days of British jet engine development that the flow can be unstable under these conditions and that self-induced periodic disturbances on the flow can develop. The disturbances are caused by the propagation along the cascade, at approximately the relative tangential component of mainstream velocity, of regions where the flow is badly separated from the airfoils. These regions where the blades are severely stalled generally are called stall cells. The problem of stall cell propagation in axial compressors has continued to receive considerable attention since the pioneering analytical treatment by Emmons (Ref. 5) because of its importance as a cause of blade fatigue failure.

The appearance of stall propagation in aircraft gas turbine engines generally occurs in the early stages of the axial compressor during any off-design operating condition in which these stages operate at much higher than design incidence. This condition can arise because of restriction of flow associated with engine acceleration or because of operation at lower than the "design value of reduced engine speed, $N/\sqrt{T}$." Several mechanical devices are in use which tend to prevent the occurrence of rotating stall by lowering the incidence in the first few stages during such off-design operation. However, there are weight penalties and/or aerodynamic losses associated with these devices.

A satisfactory stall propagation theory might lead to: 1) prevention of unsteady flow due to stall propagation when the incidence of the mean flow is high; 2) alteration of the stall cell pattern and/or its velocity of propagation so that for a given cascade geometry and mean flow, the forcing frequency of the blade loading can be chosen by the designer; or 3) prediction of enough information about the unsteady flow so that blades can be designed to withstand the unsteady aerodynamic loading.

However, before such a theory can be achieved, it appears that more must be known about the detailed nature of the flow during stall propagation

in a blade row than has appeared in the literature. Experiments were run in a radial outflow circular cascade installed in a closed circuit wind tunnel in order to take high speed schlieren and interferometer pictures of the flow through a portion of the cascade during stall propagation. Further experiments were run with an isolated rotor of an axial flow compressor. The data taken in these two test rigs suggest certain approximations to the flow which aid in the subsequent analytical treatment of the problem.

The analysis of the general problem of stall propagation in axial compressors is obviously difficult since an unsteady, rotational, three-dimensional flow of a compressible fluid is involved. In order to retain the essential features of the flow but to simplify the problem as much as possible for analytical treatment, the flow is assumed to be two-dimensional and incompressible and limited to the case of an isolated blade row. It is believed that further analysis of this problem is necessary before the much more difficult, three-dimensional and multi-stage problem can be successfully attacked.

There have been several analyses of the problem with the restricting assumptions given above.* The main reason for attempting another analysis of the same problem is the fact that all of the known previous theoretical work has been further restricted by the assumption that the unsteady velocity perturbations are small with respect to the mean flow velocity. From the experimental data presented in Section 4 and in the listed references, this assumption does not appear to be a good approximation, and the present analysis is not restricted to small unsteady perturbations. Moreover, the previous analyses have been based upon rather restrictive representations of an isolated blade row, either as a lifting line or infinitesimally spaced flat plates; whereas, in the present analysis, the chord, spacing, shape, and detailed stall characteristics of the blades are not specified. Finally, none of the theories, except Ref. 19, has offered apparent physical causes which determine the number of stall cells. The analytical flow model used herein appears to present qualitative information in this regard.

---

* These analyses are given in Refs. 5, 12, 18, 19. A brief summary of each is presented in Ref. 19.

From the state of the art at the present time, it appears that the desirable features of a stall propagation theory are predictions for a given cascade geometry of:

a) mean flow incidences at which stall propagation is possible

b) the number of stall cells

c) the velocity of stall cell propagation

d) the magnitude of unsteady aerodynamic forces on the airfoils

Such a theory is the goal toward which the work presented herein is directed.

2 Background

Conditions required for the existence of small perturbation stall propagation and a mechanism by which the stalling of rigid airfoils in cascade can propagate has been clearly explained in Refs. 5 and 19, where the cascade is assumed to consist of infinitesimally spaced flat plates of finite chord which stall at or their trailing edges and between which the flow is one-dimensional. It is apparent that, as is described in these references, the diversion of flow around a stalled airfoil tends to stall the adjacent airfoil on its suction side and unstall the opposite adjacent airfoil. However, in order to apply the analysis of Ref. 19 to calculate the velocity of stall propagation, it is necessary to know an "equivalent chord length" if the airfoils do not stall locally at their trailing edges. In general, from the data presented herein, it appears that the separation of the boundary layer associated with stalling occurs more nearly at the airfoil leading edge during stall propagation and that the flow in the blade passages is rather far from one-dimensional for typical cascade solidities. It was further assumed in Ref. 19 that the performance of a blade; i.e. the "discharge coefficient A," or blade boundary layer displacement thickness, was a function only of local incidence. A result of the analysis based upon these assumptions was that the harmonics of the small perturbation travelled at different velocities and it became necessary to restrict the velocity perturbation upstream of the cascade to a pure sine wave in the analysis in order that it should maintain its shape as it propagated. The sine wave shape does not agree well with experimental data, particularly for small numbers of cells.

In all the previous analyses, the equations of motion were solved for the irrotational motion of the fluid upstream of the cascade with the cascade as a boundary and the cascade characteristics appearing in the boundary conditions. Since the time dependent differential equations are non-linear, the assumption of small unsteady perturbations was necessary in order to linearize and solve the equations. Furthermore, in order to make the boundary conditions continuous, it was necessary to restrict the cascade geometry to infinitesimal blade spacing. The analyses based upon the assumption of small perturbations have yielded valuable information about the qualitative nature of stall propagation, and undoubtedly this assumption is valid for the prediction of the onset of propagation. However, the validity of the analyses in calculating propagation velocities of large amplitude perturbations appears uncertain.

In Ref. 18 an analysis based upon representation of the cascade as a distributed vortex sheet led to the prediction of infinite velocity of propagation for some values of incidence unless an arbitrary "boundary layer phase lag" was included. (This difficulty did not arise in the analyses of Refs. 12 and 19, where the assumption of infinitesimal blade spacing was made also.) From the experimental data and analysis herein, it appears that if the two-dimensional flow between finitely spaced airfoils is considered in representing the cascade during stall propagation, the propagation velocity must be of the same order of magnitude as the free stream velocity even if the "boundary layer phase lag" of the airfoils is zero. As the dimensions of the cascade shrink to zero, similitude requires that V_p remain finite. The present analysis indicates, also, that the stall cells must be regions of high losses and low stagnation pressure in a coordinate system fixed to the stall cell pattern, which is contrary to the assumption of constant stagnation pressure in the "airfoil theory" section of Ref. 18.

Information derived from high speed interferometer pictures of the flow through a portion of a cascade during stall propagation suggests an analytical approach, which does not necessitate the direct integration of the equations of motion and which is not limited to small perturbations, infinitesimal blade chord, or infinitesimal blade spacing and which does not require arbitrary assumptions regarding the location of separation of the boundary layer from the airfoil or the time required for separation.

3 Analysis of Stall Propagation in a Blade Row

3.1 Development of a Vortex Flow Model

3.1.1 Experimental and Mathematical Justification

It is noted in the interferometer pictures of rotating stall in a circular cascade (Figs. 22, 25, 26 and 27) that the vorticity shed downstream from the cascade airfoils appears to be concentrated largely in discrete vortices which accumulate at and depart from the leading and trailing edges of the airfoils as they periodically stall and unstall. Furthermore, the pictures indicate that the airfoils shed a large part of their bound vorticity when they stall out. This appears to be true for all of the circular cascade configurations, Reynolds numbers, and Mach numbers tested. Experimental data and calculations which support these conclusions and which suggest that they may be valid also for the flow through a research compressor assembled as an isolated rotor are presented in Section 4. In general, the data suggest that both the rotor and cascade airfoils which were used in the tests shed vortices during stall propagation similar to the Karman vortex-street shed from a flat plate and that the vortices formed in a manner similar to the vortices formed at the edge of a flat plate moved impulsively from rest normal to its plane, as in the analysis of Ref. 1.

However, the first suggestion that there might be a strong connection between stall propagation and vortex shedding was in Ref. 19, where it was observed experimentally that, as the solidity of the circular cascade was reduced, the frequency of stall propagation approached the Karman vortex-street frequency for an isolated plate as found experimentally in Ref. 6. Similar data for a different configuration of the circular cascade is shown in Fig. 29.

With the above experimental evidence as a basis, it is assumed that during stall propagation, all of the circulation downstream of the cascade is about discrete potential vortices, which are shed from the airfoils when they alter their circulation upon entering or leaving a stall cell. The experimental evidence suggests that if this is done, it should be possible to devise a vortex flow model of stall propagation in a blade row where the vortex shed from the leading edge of a blade moves across the passage and stalls the adjacent blade before moving on downstream with undiminished strength.

There are several advantages which arise from the fact that the hypothetical flow-model is irrotational except at discrete singularities. The most important advantage is that the flow, even though it is unsteady,

is "kinematic;" that is, the equations of motion need not be integrated to solve the flow, since the assumed conditions of irrotationality and incompressibility alone are sufficient. This may be shown from the vector identity,

$$\nabla^2 V = \text{grad div } V - \text{curl curl } V.$$

The continuity equation,

$$\frac{\partial \rho}{\partial t} + \text{div } \rho \, V = 0,$$

shows that div $V = 0$ since ρ is assumed constant. Stokes' and Kelvin's Theorems are not affected by time variation of flow and are sufficient to determine irrotationality. Since all vorticity is assumed to be concentrated at singular points and inside airfoil surfaces, curl $V = 0$ everywhere in the flow field because the singular points are excluded from the field. Consequently, $\nabla^2 V = 0$. La Place's Equation is satisfied at every instant of time, and the flow may be built up by the superposition of the unsteady potential flows about the vortices which are assumed to be shed from the airfoils and convected downstream.

If one examines the effect of a single potential vortex upon the flow about an isolated flat plate, one can obtain qualitative information which is useful in the subsequent analysis of a complete cascade of airfoils.

3.1.2 Effect of a Vortex on the Flow About a Flat Plate

To find the effect of an adjacent potential vortex upon the circulation about a flat plate of chord L in streaming flow, the method used in Ref. 13 to estimate bi-plane wing interference is extended. The two-dimensional flow about a circular cylinder which by the Joukowski transformation can be altered to the desired flow is first considered.

Let $\mathcal{f} = \xi + i\,\eta$ be the complex coordinate in the circular plane and $f(\mathcal{f})$ be the complex potential of the flow before the "disturbance" of the flow by the introduction of the circular cylinder, $|\mathcal{f}| = \frac{L}{4}$. Then after the cylinder is introduced, by the circular theorem of Ref. 13, the complex potential is given by

$$W(\mathcal{f}) = f(\mathcal{f}) + \bar{f}(\frac{L^2}{16\mathcal{f}}) - \frac{i\Gamma_0}{2\pi} \ln \mathcal{f}$$

where $\bar{f}$ denotes the complex conjugate of f and $\Gamma_0/2\pi$ is the circulation about the cylinder.

If $\mathcal{S}_o$ is a stagnation point on the cylinder

$$\frac{dW}{d\mathcal{S}} = 0 \quad \text{when} \quad \mathcal{S} = \mathcal{S}_o = \left(\frac{L}{4}\right)e^{i\theta_o}$$

$$\mathcal{S}_o \cdot \overline{\mathcal{S}}_o = \frac{L^2}{16} \quad , \quad \overline{\mathcal{S}}_o = \frac{L^2}{16\,\mathcal{S}_o}$$

and $f'(\mathcal{S}_o) = u_o - i\,v_o$, $\overline{f}'(\overline{\mathcal{S}}_o) = u_o + i\,v_o$

where u, v are the velocity components at $\mathcal{S}$ in the "undisturbed flow;" i.e. before the cylinder is introduced.

$$\left(\frac{dW}{d\mathcal{S}}\right)_{\mathcal{S}_o} = f'(\mathcal{S}_o) - \frac{L^2}{16\mathcal{S}_o^2}\,\overline{f}'\!\left(\frac{L^2}{16\,\mathcal{S}_o}\right) - \frac{i\,\Gamma_o}{2\pi\,\mathcal{S}_o} = 0$$

$$\frac{\Gamma_o}{2\pi} = -i\,\mathcal{S}_o\,f'(\mathcal{S}_o) + i\,\overline{\mathcal{S}}_o\,\overline{f}'(\overline{\mathcal{S}}_o)$$

$$\frac{\Gamma_o}{2\pi} = -i\,(\xi_o + i\eta_o)(u_o - i\,v_o) + i\,(\xi_o - i\eta_o)(u_o + i\,v_o)$$

$$\frac{\Gamma_o}{2\pi} = -2\,(\xi_o\,v_o - \eta_o\,u_o)$$

$$2i\,\mathcal{S}_o\,[f'(\mathcal{S}_o)] \equiv 2i\,(\xi_o + i\eta_o)(u_o - i\,v_o)$$

$$= 2i\,(\xi_o\,u_o + \eta_o\,v_o) + 2\,(\xi_o\,v_o - \eta_o\,u_o)$$

$$\therefore \frac{\Gamma_o}{2\pi} = -R\left[2i\,\mathcal{S}_o\left\{f'(\mathcal{S}_o)\right\}\right]$$

Let $u_o + i\,v_o \equiv q\,e^{i\psi}$, then $u_o - i\,v_o = q\,e^{-i\psi} = f'(\mathcal{S}_o)$

Substituting into the above equation gives

$$\frac{\Gamma_o}{2\pi} = - R\left[2i \frac{Lq}{4} e^{i(\Theta - \psi)}\right]$$

$$\frac{\Gamma_o}{2\pi} = + 2 \frac{L}{4} q \sin(\Theta - \psi) = 2 \frac{L}{4} v_t$$

where v_t is the velocity tangent to the circle at $\mathcal{S}_o$ in the "undisturbed flow."

Applying the above result to an "undisturbed flow" consisting of a uniform velocity W at the angle β and a potential vortex Γ at (r_1, Θ_1), if one takes the trailing edge of the cylinder to be a stagnation point and places it at the origin; $\Gamma_o/2\pi$ gives the circulation required to maintain the Kutta condition, and

$$\Gamma_o/2\pi = \frac{L}{2} v_t = \frac{L}{2}\left(W \sin\beta + \frac{\Gamma \cos\Theta_1}{2\pi r_1}\right)$$

$$\Gamma_o = \pi L W \sin\beta + \frac{L \cos\Theta_1}{2r_1}\Gamma .$$

The equation above indicates that if the Kutta condition is satisfied, the loci of the vortex Γ for constant cylinder circulation $\Gamma_o/2\pi$ form a bi-polar system of circles. When the Joukowski transformation is applied to the flow, the cylinder becomes a flat plate of chord L and the circles are transformed into curves which pass through the trailing edge of the plate. The dashed curves in Fig. 1 are the loci of the vortex Γ for con-stant plate circulation $\frac{\Gamma_o}{2\pi}$, which is given by

$$\Gamma_o = \pi L W \sin\beta + n \Gamma$$

if the Kutta condition is satisfied. The curve for n = 0 is labeled the neutral line. When the vortex Γ is on the neutral line it induces no velocity at the trailing edge of the plate and has no effect on the cylinder circulation.

The effect of plate camber may be estimated by assuming the plate to be a circular arc which transforms into a circle displaced from the origin as shown in Ref. 16 and indicated in Fig. 2. It can be seen from Fig. 2 that if Θ is the camber of the plate and if ε is the displacement of the circle from the origin, then in the notation of Fig. 2,

$$R - 2\epsilon = R \cos \frac{\theta}{2}, \quad 2a = R \sin \frac{\theta}{2}$$

$$\frac{2a}{\sin \theta/2} - 2\epsilon = \frac{2a}{\tan \theta/2}$$

$$\frac{1}{\sin \theta/2} - \frac{1}{\tan \theta/2} = \frac{\epsilon}{a} = \tan \alpha$$

$$\alpha = \tan^{-1} \left(\frac{1}{\sin \theta/2} - \frac{1}{\tan \theta/2} \right)$$

The solid curve in Fig. 1 is the neutral line for a plate with camber angle $\theta = 30°$. The displacement of the neutral line indicates the manner in which the other curves are displaced by the effect of plate camber.

From Fig. 1 it can be seen that if a vortex is in the vicinity of a plate, the plate circulation is greatest when it is near the trailing edge. Therefore, if a vortex is shed from the leading edge of one of a cascade of airfoils, the circulation about the adjacent airfoil goes through a maximum value just after the vortex passes under its trailing edge. In Figs. 22B, 25 and 26, it can be seen that as the shed vortex Γ approaches the location for maximum Γ_0, the succeeding cascade airfoil stalls out and sheds another vortex Γ. In this simple quasi-steady analysis, only the effect of one shed vortex is considered. However, Fig. 1 indicates that this is the dominating effect, since the vortices shed from the other cascade airfoils do not approach the trailing edge of the airfoil in question so closely. The effect of the vorticity shed from the airfoil itself as its circulation changes is neglected in this simple quasi-steady analysis. However, it appears that one may conclude that there is little tendency for a cascade airfoil to stall until the adjacent shed vortex approaches its trailing edge. A certain amount of time is required for the shed vortex to move to such a location; therefore, infinite propagation velocity is precluded even though the time required for the separation of the boundary layer and accumulation of vorticity is neglected. The qualitative explanation above is a description of a mechanism by which stalling can propagate along a cascade of airfoils. This description indicates which

direction the stalling will propagate and that the velocity of propagation must be of the same order of magnitude as the free stream velocity.

3.1.3 The Trajectory of a Shed Vortex

With the quasi-steady effect of a vortex on plate circulation as determined in the previous section, it should be possible to estimate a velocity of stall propagation along a blade row if the trajectory of the shed vortex can be calculated, and a stall criterion can be established to determine when the succeeding vortex is shed. Although difficulties are encountered which appear to be insurmountable, the attempts made to calculate the shed vortex trajectory are presented briefly so that these difficulties may be pointed out and so that some qualitative information can be derived which is used in the succeeding analysis of Section 3.2.

In the first attempt, the cascade is assumed to be represented by an infinite series of potential vortices as described in Ref. 17 where it was shown that the conjugate complex velocity vector given by the geometry of Fig. 3 is

$$(\overline{W}) \equiv u - i\upsilon = \frac{i\Gamma}{2s} e^{i\lambda} \coth\left(\frac{\pi z}{s} e^{i\lambda}\right)$$

where $z = r\, e^{i\theta} = x + i\, y$ = complex coordinate,

$u + i\, v$ = complex velocity vector.

Values of the real and imaginary parts of the function,

$$e^{i\lambda} \coth\left(\pi e^{i\lambda} \cdot \frac{x}{s}\right) - s/\pi x$$

are tabulated for various values of $\frac{x}{s}$ in Ref. 17. By plotting this data into graphs, it becomes easy to calculate $(u + i\, v)$ at any point $z = x$ in the field near a vortex street at arbitrary angle λ with the vortex at the origin missing. It is assumed that the vortex at the origin is a free vortex, having been shed from its airfoil; and its trajectory is calculated by a stepwise numerical procedure making use of the graphs.

The geometry of Fig. 4 is used in the calculation since this corresponds to the flow geometry of Fig. 22. It is assumed that before the vortex is shed, the effective incidence on all of the cascade airfoils is given by the mean velocity vector W_m, which is the velocity halfway between each vortex (or airfoil). $(\Delta i)a$, the local change from this effective incidence at airfoil (a) is calculated as a function of the location of the

shed vortex. The results are indicated in Table 1, where n is the number of time intervals, $\Delta t = \frac{s}{20\ W_x}$, after the vortex has been shed, and β_a is the local mean air angle at airfoil (a). The location of the shed vortex as a function of n is shown in Fig. 4.

TABLE 1

n	β_a	$(\Delta i)_a$
0	55.5°	0
4	56.0	+ 0.5°
7	55.4	- 0.1
9	57.2	+ 1.7
10	57.8	+ 2.3
11	60.1	+ 4.6

It is noted in Table 1 that $(\Delta i)_a$ is less than 1° until after n = 9. The effect is the same found in Section 3.1.2 for plate circulation as a function of the location of vortex Γ ; that is, neither incidence nor circulation increases rapidly at airfoil (a) until the shed vortex Γ approaches its trailing edge. This qualitative information is used in the subsequent analysis of Section 3.2.

If it is assumed that blade (a) stalls at (n = 11), or when $(\Delta i)_a$ = 4.6° (which gives roughly the same vortex location as observed in Fig. 22 at the time when the succeeding blade stalls), the velocity of stall propagation is $\frac{V_p}{W_x} = \frac{20}{11}$. Similar results were obtained when the calculation was made assuming that alternate blades in the cascade stalled simultaneously (which corresponds approximately to the stall cell pattern of Fig. 22 for 16 cells, 27 blades), and the calculated value for V_p/W_x was $\frac{20}{9}$, about twice the experimental value.

It is concluded that the representation of the cascade used here is too simple to give good numerical answers, since the effect of the presence of the blade at the origin has been neglected after its circulation is shed.

An attempt is now made to include the effect of the blade from which the vortex Γ is shed in calculating the trajectory of the vortex Γ . It will be shown that this effect on the shed vortex is to reduce its transport

velocity when it is near the blade, so as to give smaller values for $\frac{V_p}{W_x}$. The neglected boundary layer time delay further reduces $\frac{V_p}{W_x}$.

In Ref. 10, the following expression is derived for the path of a vortex in streaming flow over a flat plate using the notation of Fig. 5.

$$W\left(r - \frac{L^2}{16r}\right)\sin(\theta-\beta) + \frac{\Gamma_0}{2\pi}\ln\frac{4r}{L} + \frac{\Gamma}{4\pi}\ln\frac{r^2}{r^2 - L^2/16}$$

$$- \frac{\Gamma}{4\pi}\ln\left[1 - \frac{L^2}{8r^2}\cos 2\theta + \frac{L^4}{256\,r^4}\right]^{1/2} = \text{const.}$$

And for the transport velocity components of the vortex in Fig. 5, it was shown that

$$\mu - i\,\upsilon = \frac{\left(\frac{4\varsigma}{L}\right)^2}{\left(\frac{4\varsigma}{L}\right)^2 - 1}\left(\mu' - i\,\upsilon'\right) - i\,\frac{2\Gamma}{\pi L}\cdot\frac{\frac{4\varsigma}{L}}{\left[\left(\frac{4\varsigma}{L}\right)^2 - 1\right]^2}\;;$$

where $z = r\,e^{i\theta} = \varsigma + \frac{L^2}{\varsigma}$, and $\varsigma = r'e^{i\theta'}$. ς, u' and v' are the radius, vector and velocity components in the circular plane or Joukowski transform of Fig. 5. It should be noted *that* as was shown in Ref. 10, the path of a vortex near a flat plate is not simply the Joukowski transform of the path in the circular plane but is given by the "Routh stream function."

If it is assumed that the plate sheds all of its distributed vorticity into the vortex Γ, $\Gamma_0 = 0$; and

$$\mu' = W\cos\beta - W\left(\frac{L}{4r'}\right)^2\cos(2\theta'-\beta) + \frac{\frac{\Gamma}{2\pi L}\sin\theta'}{\frac{r'}{L}\left[1 - \left(\frac{4r'}{L}\right)^2\right]}$$

$$\upsilon' = W\sin\beta - W\left(\frac{L}{4r'}\right)^2\sin(2\theta'-\beta) - \frac{\frac{\Gamma}{2\pi L}\cos\theta'}{\frac{r'}{L}\left[1 - \left(\frac{4r'}{L}\right)^2\right]}.$$

For this simplest case of one vortex near a plate with no circulation, a finite difference method could be used to determine the time required for the vortex to move between two points on its path. However, difficulty arises from the fact that when the vortex is near the plate just after being shed, the assumption of potential flow gives very erroneous results. This effect can be observed in the simpler case of a vortex near a circular cylinder.

In the notation of Fig. 7, the transport velocity components of a vortex Γ near a circular cylinder with no circulation ($\Gamma_0 = 0$) are

$$\overset{\circ}{r} = W \left[1 - (\tfrac{R}{r})^2 \right] \cos (\theta - \beta)$$

$$r \overset{\circ}{\theta} = - W \left[1 + (\tfrac{R}{r})^2 \right] \sin (\theta - \beta) + \frac{\Gamma/2\pi r}{(\tfrac{r}{R})^2 - 1}$$

It can be seen from the second equation that when the potential vortex Γ is near the circle, it moves rapidly around the circle in a counter-clockwise direction. If it is assumed that the cylinder sheds all the vorticity required to satisfy the Kutta condition in streaming flow, $\Gamma_0 = 0$, $\Gamma = 4\pi WR \sin \beta$; and if Γ is near the leading edge of the circle,

$$r \overset{\circ}{\theta} \cong W \sin \beta \left[2 + \frac{1}{(\tfrac{r}{R})^2 \left\{ (\tfrac{r}{R})^2 - 1 \right\}} \right] .$$

Therefore, the initial point of the trajectory of the potential vortex cannot be taken near the leading edge of the airfoil, and the calculation must be started from some arbitrary point away from the airfoil surface. The shape of the trajectory and the time required for the vortex to be convected downstream depend critically upon the initial point chosen, as indicated in Fig. 6, which shows the location of a vortex after several equal time increments for two arbitrarily chosen initial points. Examination of Fig. 8 indicates that near the plate the transport velocity with which the shed vortex moves downstream is less than at points away from the plate. This information is used in the subsequent analysis, which circumvents the difficulty mentioned above and which has been devised to deal with the problem of the convection of a series of vortices shed from a cascade of airfoils.

It is interesting to note that there is a point in the flow about a circle from which the vortex Γ will not move in an ideal fluid (with no dissipation of the vortex).

If $\Gamma_0 = 0$, this point is given by $\theta = \beta + 90°$,

$$\frac{\Gamma}{2\pi RW} = \left[- \left(\frac{r}{R}\right)^3 + \frac{r}{R} \right] \left[\left(\frac{R}{r}\right)^2 + 1 \right] = \left[\left(\frac{r}{R}\right)^3 - \frac{R}{r} \right]$$

For $\beta = 30°$ and $\theta = 120°$, $\overset{\circ}{r} = 0$, and $r\overset{\circ}{\theta}$ is plotted as a function r/R in Fig. 8 for three values of Γ'/Γ_o assuming $\Gamma' + \Gamma_o = 4\pi$ W R sin β.

It appears to be quite difficult to establish a suitable initial point to begin calculating the vortex trajectory and to estimate the time required for the vorticity to be shed from the airfoil surface *and* to accumulate at this point. The problem was solved for a special case in Ref. 1, but the method used appears to be too involved for the problem at hand.

3.2 Analysis of a Vortex Flow Model of Stall Propagation

3.2.1 Derivation of Expressions for Propagation Velocity

Velocity measurements taken during stall propagation indicate that for a given operating condition or mean flow, the unsteady velocity perturbation translates at constant velocity V_p along the cascade, and to a first approximation, the shape of the velocity profile of the unsteady perturbation is maintained constant. In other analyses, previously listed, the assumption was made that the profile is constant and it is also made here, although data which will be presented in Section 4 indicate that this is not always strictly true. With the approximation that each cascade airfoil sheds a discrete potential vortex ($+ \Gamma$) when it enters the stall cell and another ($- \Gamma$) of opposite sign when it leaves the cell, it follows that all the trajectories of vortices (of same sign) shed from the cascade airfoils must be translates of the same curve and separated by the blade spacing(s) along the cascade.

The vortices which have been shed downstream must be arranged in a pattern as shown in Fig. 9. The dashed lines indicate the trajectories of the vortices shed from two succeeding blades. The ($+ \Gamma$) vortices must lie on a line b) which eventually becomes straight downstream of the cascade and the ($- \Gamma$) vortices must be located along a line c) which becomes straight and parallel to line b) downstream of the cascade. The region between lines b) and c) is called the stall cell. Lines b) and c) are of constant shape in time and move relative to the cascade with the velocity of propagation, V_p.

In a coordinate system which is fixed to the stall cell, the blades move down in Fig. 9 with velocity V_p; and the shed vortices move downstream along the stationary path lines b) and c). The flow is steady in time except for the effects due to the finite spacing of blades and shed vortices. It can be seen from Equation (1) that these are local effects confined to an area within approximately one blade spacing of the cascade and one vortex spacing of lines b) and c). Flow is diverted to each side of the stall cell which has the nature of a thick wake.

After they are far downstream of the cascade, the shed vortices are spaced uniformly by a distance (a) along lines b) and c) and move with transport velocity V. ϕ is defined as the angle between each street and the cascade axis, and n is defined as the number of vortex spaces between the streets as indicated in Fig. 9. In Fig. 10 are indicated the velocity triangles associated with the stall cell. The velocity at any point far downstream of the cascade is W_2 plus the induced velocity due to the stall cell (which is the velocity induced by two infinite vortex streets).

If the blades stall out completely when they enter the cell, the strength of the shed vortices will be of the order of magnitude

$$\pm \Gamma = (W_{\Theta_1} - W_{\Theta_2}) \, s$$

From Ref. 7, for a single infinite row of equidistant vortices, each of strength Γ (+ clockwise) at distances a apart, with the origin at a vortex, and the axis of x along the row, the velocity components induced by the vortices are

$$u = \frac{\Gamma}{2a} \; \frac{\sinh\,(2\pi\,y/a)}{\cosh\,(2\pi\,y/a) - \cos\,(2\pi\,x/a)}$$

$$v = \frac{\Gamma}{2a} \; \frac{\sin\,(2\pi\,x/a)}{\cosh\,(2\pi\,y/a) - \cos\,(2\pi\,x/a)} \; .$$

(1)

Therefore,

$$\frac{\partial v}{\partial x} = -\frac{\Gamma}{2a} \cdot \frac{2\pi}{a} \; \frac{\left(\cosh\frac{2\pi y}{a} - \cos\frac{2\pi x}{a}\right)\cos\frac{2\pi x}{a} - \sin^2\frac{2\pi x}{a}}{\left(\cosh 2\pi\,y/a - \cos 2\pi\,x/a\right)^2}$$

and for $\mathcal{U}_{max}$

$$\cosh \frac{2\pi y}{a} \cos \frac{2\pi x}{a} - 1 = 0$$

$$\cos \frac{2\pi x}{a} = \frac{1}{\cosh \frac{2\pi y}{a}}$$

$$\sin \frac{2\pi x}{a} = \sqrt{1 - \cos^2 \frac{2\pi x}{a}} = \frac{\sqrt{\cosh^2 \frac{2\pi y}{a} - 1}}{\cosh \frac{2\pi y}{a}}$$

$$= \tanh \frac{2\pi y}{a}$$

$$V_{max} = \frac{\Gamma}{2a \sinh 2\pi y/a}$$

Therefore, far downstream, the maximum lateral velocity (normal to lines b) and c)) the vortex streets can induce on each other is,

$$\mathcal{U}_{max} = \frac{\Gamma}{2a \sinh 2\pi n} ;$$

where na is the distance between lines b) and c). If $n > 1$

$$\mathcal{U}_{max} = \frac{W\Theta_1 - W\Theta_2}{500} \cdot \frac{s}{a}$$

and may be neglected.

The basis for taking $n > 1$ is derived from the hot wire data taken downstream of the isolated rotor where it is noted that the cells always cover at least two blade spaces. This appears to be true in general for stall cells in rotors. In the interferometer pictures from the circular cascade, Figs. 22B, 25, 26, it is notes that $n \cong 1$; however, the downstream flow field extends only two or three blade chords from the circular cascade, so the initial assumption of an infinite downstream field is not valid for the circular cascade.

More than a distance (a) from the vortex streets the longitudinal velocity induced by them may be neglected outside the cell, while inside the cell, from Equation (1),

$$V_1 = \Gamma/a.$$

The resultant transport velocity of each downstream vortex is V as shown in Figure 10.

Solving for the velocity of propagation V_p from Fig. 10, one finds

$$V_p = W_{\Theta_2} - \frac{V_1}{2}\sin \phi - (W_{x_2} - \frac{V_1}{2} \cos \phi) \tan \phi$$

$$V_p = W_{\Theta_2} - W_{x_2} \tan \phi \tag{2}$$

and if $\phi \cong 0$, $\quad V_p \cong W_{\Theta_2}$

This same result can be obtained easily by noting the parallelogram in the velocity diagram of Fig. 10 and solving for the equal and opposite side from V_p. One advantage of the assumed vortex flow model is that V_p can be calculated away from the cascade without solving for the detailed nature of the flow in or near the cascade except in so far as this affects the angle ϕ. It is observed that V_p and the angle ϕ are uniquely dependent if the downstream velocity W_2 is given and if $n > 1$. V_p does not depend explicitly on the physical size or shape of the stall cell or the magnitude of the velocity perturbation. Since the angle ϕ has been observed experimentally to be small in many cases, Equation (2) indicates that the fair experimental agreement between V_p and W_{Θ_2} which has been noted by other observers is an immediate consequence. However, in the analysis to follow, the only assumption regarding the angle ϕ is that it is not a large negative angle. Reasons for this assumption will be given.

To continue the analysis, the following variables are defined:

$$N \equiv \frac{V_1 \cos \phi}{W_{x_2}}$$

$$M \equiv \Gamma / \Gamma_o \qquad = \frac{\text{shed vorticity}}{\text{bound vorticity}}$$

$$X \equiv \frac{W_{x_1}}{W_{x_2}}$$

$Y \equiv$ the fraction of the downstream periphery covered by the stall cell

$$= \frac{na/\cos \phi}{d}$$

It is assumed that the circulation around a blade away from the cell is given by

$$\Gamma_o = s(W_{\Theta_1} - W_{\Theta_2}) \tag{3}$$

Then $V_i = \dfrac{\Gamma}{a} = \dfrac{M\Gamma_o}{a} = M \dfrac{s}{a} (W_{\Theta_1} - W_{\Theta_2}) = \dfrac{N W_{x_2}}{\cos \emptyset}$

$$\frac{s}{a} = \frac{N}{M (X \tan \beta_1 - \tan \beta_2) \cos \emptyset} \tag{4}$$

The time average continuity equation gives

$$d \cdot W_{x_1} = (d - \frac{na}{\cos \emptyset}) W_{x_2} + \frac{na}{\cos \emptyset} (W_{x_2} - V_i \cos \emptyset)$$

$$X - 1 = Y (1 - N) - Y$$
$$X = 1 - YN \tag{5}$$

Solving from Fig. 10 for the velocity with which the vortices move along lines b) and c), one finds

$$V_a = \frac{W_{x_2}}{\cos \emptyset} - \frac{V_i}{2} .$$

Since the frequency with which vortices pass downstream points on lines b) and c) must be the same as the frequency with which vortices are shed onto the lines,

$$\frac{s}{a} = \frac{V_p}{V_a} = \frac{W_{\Theta_2} - W_{x_2} \tan \emptyset}{\dfrac{W_{x_2}}{\cos \emptyset} - \dfrac{V_i}{2}} = \frac{(\tan \beta_2 - \tan \emptyset) \cos \emptyset}{1 - \dfrac{N}{2}} \tag{6}$$

Eliminating $\dfrac{s}{a}$ from Equations (4) and (6) gives

$$(\tan \beta_2 - \tan \emptyset) \cos^2 \emptyset = \frac{N - N^2/2}{M (X \tan \beta_1 - \tan \beta_2)} \equiv K. \tag{7}$$

From the velocity diagram for an isolated rotor in Fig. 11, it can be seen that

$$X \tan \beta_1 - \tan \beta_2 = \tan \alpha_2.$$

This relationship is valid only for an isolated rotor with no upstream whirl velocity $(C_{\theta_1} = 0)$.

It is noted that since the shed vortices are convected downstream, $N < 2$. Also, the range of M must be limited to

$$0 < M < 1.$$

The curves of K versus N for $M(X \tan \beta_1 - \tan \beta_2)$ assumed constant are parabolas. Curves of K versus $\tan \phi$ for β_2 assumed constant are almost straight for $|\tan \phi| < 0.2$, as shown in Fig. 12, which is a plot of K versus $\tan \phi$ for $\beta_2 = 30°$ and $50°$. (Experimental values of β_2 for the isolated rotor from which data were taken in Section 4 fall between $30°$ and $50°$.)

A diagram of K versus N and K versus $\tan \phi$ with the intercepts and peaks labeled is shown in Fig. 13. It is indicated that for a given value of K, there are either two or zero solutions for the angle ϕ (and V_p). However, solutions which are physically possible appear to lie on the positive side of the peak of the K versus $\tan \phi$ curve, $(\tan \phi > \tan \beta_2 - \sec \beta_2$ in Fig. 13), since experimental values of ϕ presented in Section 4 fall between $-15°$ and $+19°$, and since all known experimental values of V_p are less than W_{θ_1}. Qualitative reasoning based on the results of Section 3.1.2 indicates that a blade has little tendency to begin to stall until the vortex shed from the preceding blade approaches the trailing edge. If time $T = s/V_p$ is required for the vortex to be formed and shed from a blade and to approach the trailing edge of the succeeding blade when it begins to stall, T is also the time required for the vortex to move from points 1) to 2) in Fig. 9. Since it has been shown that the velocity of the shed vortex is less when it is near the blade than when it is downstream (for an isolated blade and vortex) and since there is a boundary layer time delay required for the vortex to be formed, it would appear that large negative values for ϕ are impossible for typical cascade geometries. This precludes the possibility of infinite propagation velocity, since from Equation (2) for $V_p \rightarrow \infty$, $\phi \rightarrow -90°$.

It is assumed henceforth that

$$\tan \beta_2 - \sec \beta_2 < \tan \phi < \tan \beta_2,$$

which is equivalent to assuming that

$$0 < V_p < W_{\theta_1}$$

as shown in Fig. 13. Since in this range of ϕ, K versus tan ϕ can be roughly approximated by a straight line which passes through the intercepts (tan β_2, 0), (0, tan β_2); it can be seen from the geometry of Fig. 13 that

$$\frac{V_p}{W_{x_2}} \cong K \cong \frac{N - N^2/2}{M \,(X \tan \beta_1 - \tan \beta_2)} \,. \tag{8}$$

Or, for an isolated rotor

$$\frac{V_p}{W_{x_2}} \cong \frac{N - N^2/2}{M \tan \alpha_2}$$

$$\frac{V_p}{W_{\theta_2}} \cong \frac{N - N^2/2}{M \tan^2 \alpha_2}$$

The above approximation should be sufficient for the general relationship existing between the variables to be given by Equation (8). If $N \cong 1$, there is small net axial flow through the blades in the stall cell since lines b) and c) in Fig. 9 are path lines and the mass flow into the cell through the blades must be equal to the axial flow in the cell downstream. It is assumed that the blades in the stall cell must lose most of their circulation if $N \cong 1$, and as a result $M \cong 1$.

Experimental values of N appear to be close enough to unity for the assumption that $N = 1$, since the variation of K with N is small for N near unity as shown in Fig. 13, (if $3/4 < N < 1$, $.47 < \frac{K}{\tan \alpha_2} < .50$).

For an isolated rotor ($C_{\theta_1} = 0$) and for ($M = N = 1$), Equation (8) becomes,

$$\frac{V_p}{W_{x_2}} \cong K \cong \frac{\cotan \alpha_2}{2}$$

$$\tag{9}$$

$$\frac{V_p}{W_{\theta_2}} \cong \frac{\cotan^2 \alpha_2}{2}$$

Equation (9) gives an approximate prediction of the propagation velocity for the type of stall cell assumed based upon the approximation that K versus tan ϕ is linear. However, if $M = N = 1$, Equation (7) can be solved for

$\tan \phi$, and a better answer can be obtained without recourse to this approximation.

If $M = N = 1$, Equation (7) becomes

$$\tan \beta_2 - \tan \phi = \frac{1 + \tan^2 \phi}{2(X \tan \beta_1 - \tan \beta_2)}$$

$$0 = \tan^2 \phi + 2(X \tan \beta_1 - \tan \beta_2) \tan \phi + 1 - 2 \tan \beta_2 (X \tan \beta_1 - \tan \beta_2)$$

$$\tan \phi = -(X \tan \beta_1 - \tan \beta_2)$$

$$\pm \left[(X \tan \beta_1 - \tan \beta_2)^2 - 1 + 2 \tan \beta_2 (X \tan \beta_1 - \tan \beta_2) \right]^{1/2}$$

$$= \tan \beta_2 - X \tan \beta_1 \pm \left[(X \tan \beta_1 - \tan \beta_2)(X \tan \beta_1 + \tan \beta_2) - 1 \right]^{1/2}$$

$$= \tan \beta_2 - X \tan \beta_1 \pm \sqrt{(X^2 \tan^2 \beta_1 - \tan^2 \beta_2 - 1)}$$

$$\frac{V_p}{W_{x_2}} = \tan \beta_2 - \tan \phi = X \tan \beta_1 \mp \sqrt{X^2 \tan^2 \beta_1 - \tan^2 \beta_2 - 1}$$

$$\frac{V_p}{W_{x_1}} = \tan \beta_1 \mp \sqrt{\tan^2 \beta_1 - \frac{\tan^2 \beta_2 + 1}{X^2}} \qquad (10)$$

The plus sign for the radical in Equation (10) is discarded since it implies that $\tan \phi < \tan \beta_2 - \sec \beta_2$.

Therefore,

$$\frac{V_p}{W_{\theta_1}} = 1 - \sqrt{1 - \left(\frac{W_2}{W_{\theta_1}} \right)^2} \quad \text{and}$$

$$\qquad (11)$$

$$\frac{V_Q}{U} = \sqrt{1 - \left(\frac{W_2}{W_{\theta_1}} \right)^2} = \frac{\text{stall pattern RPM}}{\text{rotor RPM}}$$

for an isolated rotor, since $W_{\theta_1} = U$, and $V_Q = U - V_p$.

If it is assumed that an isentropic pressure coefficient may be used outside the stall cell, then

$$C_p \equiv \frac{p_2 - p_1}{1/2 \, \rho \, W_1{}^2} = 1 - \left(\frac{W_2}{W_1}\right)^2$$

$$C_p = 1 - \left(\frac{W_{x_2} \cos \beta_1}{W_{x_1} \cos \beta_2}\right)^2 = 1 - \frac{1}{X^2} \cdot \frac{1 + \tan^2 \beta_2}{1 + \tan^2 \beta_1}$$

$$X^2 (1 - C_p) = \frac{1 + \tan^2 \beta_2}{1 + \tan^2 \beta_1}$$

Therefore, substituting in Equation (10),

$$\frac{V_p}{W_{x_1}} = \tan \beta_1 - \sqrt{\tan^2 \beta_1 - (1 + \tan^2 \beta_1)(1 - C_p)}$$

$$\frac{V_p}{W_{x_1}} = \tan \beta_1 - \sqrt{\tan^2 \beta_1 - (1 - C_p) - \tan^2 \beta_1 + C_p \tan^2 \beta_1}$$

$$= \tan \beta_1 - \sqrt{\frac{C_p}{\cos^2 \beta_1} - 1}$$

$$= \tan \beta_1 - \sqrt{\frac{p_2 - p_1}{1/2 \, \rho \, W_{x_1}{}^2} - 1} \quad , \qquad (12)$$

Or, using coefficients as defined in Reference 2,

$$\phi \equiv \frac{1}{\tan \beta_1}$$

$$\psi = \frac{p_2 - p_1}{1/2 \, \rho \, C_{\theta_1}{}^2}$$

$$\frac{V_p}{W_{x_1}} = \frac{1}{\phi} - \sqrt{\frac{\psi}{\phi^2} - 1} \quad .$$

Equations (11) and (12) indicate that stall cells of the type assumed ($N = M = 1$, $0 < V_p < W_{\theta_1}$) are impossible unless $W_2 < W_{\theta_1}$ or $C_p > \cos^2 \beta_1$.

If $W_2 = W_{\theta_1}$, $V_p = W_{\theta_1}$ and $\tan \phi = \tan \beta_2 - \sec \beta_2$, as indicated in Fig. 13 and $C_p = \cos^2 \beta_1$. It is interesting to note that this corresponds to the propagation velocity predicted in Ref. 19 for a simplified cascade

geometry and entirely different type of stall cell, where the upstream velocity perturbation was assumed to be a sine wave of small amplitude and many blade chords wave length. In Ref. 19, for this type of cell, it was shown that

$$\frac{V_p}{W_{x_1}} = \frac{2(1 - C_p)}{\sin 2 \beta_1}.$$

If $C_p = \cos^2 \beta_1$,

$$\frac{V_p}{W_{x_1}} = \frac{2 \sin^2 \beta_1}{2 \sin \beta_1 \cos \beta_1} = \tan \beta_1$$

$$V_p = W_{\theta_1}.$$

The preceding analysis of Section 3.2.1 indicates that this is a limiting value, and that for the assumed type of finite amplitude stall cells to exist, $C_p > \cos^2 \beta_1$.

It is assumed in the preceding analysis that all of the downstream circulation is about concentrated vortices. The implication is that: 1) the wakes shed from the blades outside the cell are thin enough or mix soon enough to be neglected, and 2) this is also true for the blade wakes in the cell (or that the velocity through the blades in the cell is small enough that the vorticity shed inside the cell can be neglected). The assumption of $M = 1$, together with that above, implies that the blades outside the cell have no drag and those inside the cell have no lift. It is assumed that the analysis is valid for more than one cell if they are spaced far enough apart so that Equation (3) remains valid, since the cells induce no velocity on each other except for their blockage effect on the main flow which is considered in the analysis.

Since in a coordinate system fixed to the stall cell pattern of Fig. 9, the flow is steady and the streamlines are straight and parallel downstream, the static pressure is constant downstream. There is a "head loss" in the stall cell determined by the velocity defect there, just as in the case of a bluff body wake; and the fraction of the downstream periphery covered by stall cells could be expressed by a time average loss coefficient of stagnation pressure. The qualitative nature of the flow for $(M = N = 1)$ is similar to

the flow about a flat plate translating along the cascade at velocity V_p and blocking the flow through a portion of it.

3.2.2 Analysis of Model for Small Perturbations

It is noted that Equation (7) gives a relationship between the three parameters (M, N, ϕ) and was developed without any assumptions regarding blade stall characteristics other than the assumption of discrete vortices downstream. If another independent equation can be derived between M, N and ϕ, by specifying the dynamic blade stall characteristics, V_p can be determined as a function of N only, or the stall cell amplitude.

For small perturbations, M and N can be related to lift and drag coefficients since for an isolated airfoil,

$$\text{lift} = \rho \; W \; \Gamma_o = 1/2 \; \rho \; W^2 . L . C_L$$

$$= \frac{C_L W}{2} . L$$

The assumption is made, as in Ref. 18, that for a cascade of airfoils also

$$= \frac{C_L W}{2} L,$$

where W is the local mean velocity and Γ_o the bound vorticity at an airfoil. $M(N, \phi)$ can be determined independently of Equation (5) if C_L is a known function of local mean air angle β as determined by the local incidence.

It is difficult to determine W and β at the airfoils near the cell for arbitrary values of N because the shape of lines b) and c) in Fig. 9 must be known. (This difficulty disappears for $N \cong 1$, since for small flow through the cell one can assume the blades shed all their vorticity; and M = 1 regardless of the shape of the cell, as in the previous analysis.) However, if $N \ll 1$, lines b) and c) must be straight even near the cascade, and it becomes possible to determine W and β by restricting the amplitude of the stall cell to a small perturbation.

For the velocity induced by a straight vortex street of finite length, Equation (1) indicates that, except in the immediate vicinity of the street, it may be considered as a distributed sheet of strength per unit length $\frac{\Gamma}{a}$; therefore, with the notation of Fig. 14, the velocity components induced by an element of length dx are:

$$du = -\frac{\Gamma}{2\pi a} \cdot \frac{dx}{r} \sin \Theta$$

$$dv = \frac{\Gamma}{2\pi a} \cdot \frac{dx}{r} \cos \Theta.$$

For a sheet of finite length, as in Fig. 15:

$$u = -\frac{\Gamma}{2\pi a} \int_{x_1}^{x_2} \frac{y\, d\, x}{x^2 + y^2} = \frac{\Gamma}{2\pi a} (\tan^{-1} \frac{x_1}{y} - \tan^{-1} \frac{x_2}{y})$$

$$v = \frac{\Gamma}{2\pi a} \int_{x_1}^{x_2} \frac{x\, d\, x}{x^2 + y^2} = \frac{\Gamma}{4\pi a} \left[ln\, (x_2^2 + y^2) - ln\, (x_1^2 + y^2) \right]$$

$$u = \frac{-\Gamma}{2\pi a} \cdot \delta$$

$$v = \frac{\Gamma}{2\pi a} \cdot ln\, \frac{r_2}{r_1}$$

(13)

It follows that the velocity induced at the blade in the center of the stall cell, V_{ic}, as shown in Fig. 16, is parallel to the streets and equal to $\frac{\Gamma}{2a}$ if $m \gg n$. For various assumptions of C_L (β), one might assume that the blades in the stall cell have a circulation corresponding to W and β at the blade in the center of the cell, and calculate V_p as a function of N.

However, rather than assuming C_L (β) and proceeding as above, one can start with an assumption regarding the angle ϕ which appears to be supported experimentally. Values of M which correspond to values of N as determined by the dynamic stall characteristics restrict K versus N to an "operating line" similar to the dashed curve of Fig. 13. As $N \rightarrow 0$, $M \rightarrow 0$; and Equation (8) becomes indeterminate. However, if it is assumed that ϕ must remain small as $N \rightarrow 0$ for the reasons given on page 19, (in Section 4 for $N \cong 3/4$, $-15° < \phi < 20°$) the type of dynamic blade stall characteristics which satisfy this requirement can be determined as follows.

It is assumed that the M versus N curve must pass through the two points (0, 0) and (1, 1) in Fig. 13, and an intervening M versus N

relationship is sought which gives small angles ϕ for $N \ll 1$. It is seen that $M = N^p$ is a convenient function to work with. From Equation (7) values of ϕ are calculated as a function of N for various values of p and for typical experimental values of α_2 and β_2 from the isolated rotor. It is shown in Section 4 that for each of two rotor-stagger angles λ tested, α_2 and β_2 were essentially constant in the range of β_1 for which there was rotating stall and that for

$$\lambda = 52° \begin{cases} \alpha_2 \cong 37° \\ \beta_2 \cong 50° \end{cases} \text{ and for } \lambda = 30° \begin{cases} \alpha_2 \cong 40° \\ \beta_2 \cong 30° \end{cases}$$

The result of calculating $\tan \phi$ versus N for $.05 < N < .2$ and various values of p using the above values for α_2 and β_2 are shown in Table II, where it is observed that for small perturbations on the assumed flow ($N \ll 1$) and small angle ϕ, $p \cong 1$ and $M \cong N$.

TABLE II

for $(\beta)_0 = 50°$ $(\alpha_2)_0 = 37°$

N	p = 0 $M=N^0$	tan ϕ	p = .7 $M=N^{.7}$	tan ϕ	p = .85 $M=N^{.85}$	tan ϕ	p = 1 $M=N$	tan ϕ	p = 1.2 $M=N^{1.2}$	tan ϕ
.05	1	1.1	.12	.47	.08	.24	.05	Imaginary	.04	Imaginary
.10	1	.9	.20	.41	.14	.21	.10	- .1	.06	"
.20	1	.8	.32	.32	.25	.20	.20	0	.14	"

for $(\beta_2)_0 = 30°$ $(\alpha_2)_0 = 40°$

N	p = 0 $M=N^0$	tan ϕ	p = .6 $M=N^{.6}$	tan ϕ	p = .7 $M=N^{.7}$	tan ϕ	p = .85 $M=N^{.85}$	tan ϕ
.05	1	.5	.16	.20	.12	.08	.08	- .22
.10	1	.45	.25	.16	.20	.06	.14	- .19
.20	1	.37	.38	.02	.32	-.10	.25	- .65

Furthermore, it is noted from Equation (7) that if $N \ll 1$ (such that $N^2/2$ may be neglected), the same solution for ϕ and V_p results if $M = 2N \ll 1$ as for $M = N = 1$. It appears, therefore, that for small perturbations, and small angles ϕ, the percentage of vorticity the airfoils shed upon entering

a stall cell must be approximately equal to the percentage of downstream axial velocity defect in the stall cell. Therefore, the reason that small perturbation stall cells are not commonly observed may be that a compressor blade generally is thin, stalls from its leading edge during stall propagation, and must shed a large percentage of its bound vorticity. This description appears to apply to the dynamic stall characteristics of the airfoils used in Section 4 although in quasi-steady flow they exhibit a continuous C_L versus i curve even in stall as indicated by Figs. 18, 23, 46 and 53. It is shown in Section 4.1.4 that the airfoils display stall characteristics during stall propagation which depart considerably from their quasi-steady stall characteristics. It is felt that the sudden increase of i as the airfoils enter a stall cell causes them to stall abruptly from their leading edges for the reason given on page 56, even though they stall "gently" with a slow (quasi steady) increase of i.

A qualitative reason that a compressor blade should not shed a small vortex from its leading edge during stall propagation was indicated in Ref. 1, where it was shown that for a flat plate moved impulsively from rest normal to its plane, vortices must form at the edges of the plate (if infinite velocity is precluded) and that during the initial formation of these edge vortices, similitude of the flow requires them to grow until they are not small in proportion to the width of the plate. Of course, the stronger the vortex shed from a cascade blade, the greater is the tendency for the adjacent blade to stall as the vortex moves past it and the greater the tendency for stall propagation; however, there is no apparent reason why propagation of small perturbations should not occur excpet that this appears to be precluded by the dynamic stall characteristics of the airfoils.

Since small perturbation stall cells which are two-dimensional (hub to tip in a rotor) and stable have never been observed experimentally to the knowledge of the author, the analysis is pursued no further. The discussion above is offered as a qualitative speculation (not an attempt to prove) that small perturbation, two-dimensional stall cells cannot exist.

3.2.3 Prediction of a Trend for the Number of Cells

The vortex flow model used in the analysis appears to offer an explanation for the general trend toward larger numbers of cells with increasing

throttling of flow as indicated by the experimental data. The experimental results indicate that with further throttling of the flow through an isolated rotor after the formation of one stall cell, the cell first grew wider (n increased in Fig. 9), then two cells appeared and grew wider, etc. until four cells appeared and surging flow began. The vortex flow model indicates that if m is finite in Fig. 16, the velocity induced by the stall cell at the blade in the center of the cell, $(V_i)_c$, decreases as $\frac{n}{m}$ increases. This effect can be shown qualitatively by assuming the lines b) and c) to be entirely straight. Then from Equation 13 , if $m \gg n$

$$(V_i)_c = \frac{\Gamma}{a} \ (1/2 - \frac{n}{2\pi m}).$$

As $\frac{n}{m}$ increases, $(V_i)_c$ decreases faster than near the edges of the cell, there is more flow through the center of the cell than near the edges, and the blade at the center of the cell tends to unstall, thereby splitting the cell into two cells which become distributed axisymmetrically around the rotor.

It does not appear possible to predict when a stall cell will split as $\frac{n}{m}$ increases without detailed information regarding the dynamic stall-unstall characteristics of the airfoils and the shape of the cell (lines b) and c) in Fig. 9). The estimated relationship between $\frac{n}{m}$ and $(V_i)_c$ above does not indicate much effect on $(V_i)_c$ until $\frac{n}{m} > 1/3$. The measured effect is much greater and is described in Section 4.

3.2.4 Summary of Analysis

By making use of experimental data in order to develop a simplified analytical flow model, a theory of stall propagation in an isolated blade row has been developed which appears to be based upon fewer restrictive assumptions than some of the earlier analyses. In the analysis, a restriction is imposed upon nature of the stall cells. Although the approximation to the actual observed flows appears to be valid for all the blading, geometrical configurations, and flow conditions for which experiments were run, it is unknown how valid the approximation is in general. It is suggested that the approximation regarding the nature of the cells might be widely applicable to continuous cascades of thin airfoils, where the flow extends many blade chords downstream of the cascade.

It should be noted that in the preceding analysis no proof of existence, equilibrium, or stability is given for the assumed flow model. The experimental data in Section 4 are offered in lieu of mathematical proof.

4 Experimental Investigation of Rotating Stall

4.1 Investigation in a Circular Cascade

4.1.1 Description of Apparatus and Procedure

With the sponsorship of the National Advisory Committee for Aeronautics, a circular radial-outflow cascade was designed and installed in the closed circuit wind tunnel at the Gas Turbine Laboratory during 1953. The cascade was designed specifically for investigation of rotating stall and is described in detail in Ref. 9. In Fig. 17 is shown a schematic view of the test section which includes a ring of variable angle guide vanes with which the air inlet angle to the test cascade, β_1, can be continuously varied. Some dimensions of the test cascade are:

radius to guide vane trailing edges 7.2" to 6.7" (varies

with β_1)

radius to blade leading edges and measuring stations 1 and 2 respectively:

for Configuration A; 7.91, 7.69, 8.94 inches

for Configuration B; 8.66, 8.44, 9.69 inches

blade chord .96 inches

blade span 1.71 inches

blade profile NACA 65(12)10 as changed by circular transformation

number of blades = 54, 27, 18, 9 = giving nominal solidities $\sigma = 1$,

1/2, 1/3, 1/6

simulated linear cascade 65(8)10, mean line a = 1.0

Some advantages of the cascade geometry are:

1) The flow is two-dimensional through the cascade neglecting the wall boundary layers.

2) Optical measurement of the flow through a portion of the cascade is possible.

3) A continuously rotating stall pattern can be established, which is not possible for a finite length linear cascade.

Some disadvantages are:

1) Because of the radial flow, the pressure distribution about the airfoils is not precisely the same for a given pressure rise through the cascade as in a rotor or linear cascade. As described in Ref. 9, a correc-

tion was made for this effect by designing the cascade through the conformal transformation of one linear cascade such that the adverse pressure gradient on the suction side of the airfoils in the transformed, circular cascade was approximately equal to that for a second linear cascade which was simulated. It was found that the circular transformation of a linear NACA 65(12)10 cascade gave approximately the same adverse pressure gradient on the circular cascade blades at the design point as for a linear NACA 65(8)10 cascade. The data for the linear cascade pressure distributions were taken from Ref. 8. The degree of success of this procedure is indicated in Section 4.1.4 where the pressure distribution about the circular cascade blades is calculated and compared with those from Ref. 8 for one value of i.

2) The flow field downstream of the cascade is necessarily rather short which appears to have a pronounced effect on the rotating stall cell pattern as discussed in Section 5.

In Ref. 19, an experimental investigation of rotating stall in the circular cascade is described, which was conducted to determine the detailed nature of the flow and to ascertain the effects of Mach number, Reynolds number, mean incidence, and cascade solidity on the propagation of stall cells in the cascade. The experimental work described here is a continuation of this investigation. The procedures and instrumentation are largely the same as described in Ref. 19 except for the use of the Gas Turbine Laboratory portable Mach-Zehnder interferometer and a piezoelectric crystal pressure pickup described in Section 4.1.4.

The purpose of the present investigation is to extend the above data to include the effects of lower cascade stagger angle, of higher mean incidence to the cascade, and of increased clearance between guide vanes and test cascade. Quantitative measurement of the pressure field in a portion of the cascade during stall propagation is also attempted by means of high frequency interferometer pictures.

All of the tests in Ref. 19 were made with a cascade stagger angle λ fixed at $43°$. The highest angle to which the guide vanes could be turned gave an entering air angle β_1 to the cascade of $69°$; therefore, the highest mean flow incidence angle, i, possible was $26°$. Stall propagation started

at $i = 20°$. In Ref. 14, it was observed that stall propagation existed in a rotor plus guide vane axial compressor stage for $34° < i < 47°$ (relative to the rotor at mean radius). Therefore, it was deemed desirable to alter the linkages to the guide vanes to permit greater incidences to the circular cascade. It was noted in the schlieren pictures presented in Ref. 19 that during stall propagation in the circular cascade, when an airfoil stalled some of the fluid from the separated boundary layer was washed around the leading edge of the succeeding airfoil before it stalled. In hope of decreasing this effect, to increase further the incidence on the cascade airfoils, and to observe any other effects on the nature of the flow, the stagger angle of the cascade was changed from $43°$ to $31°$. For the altered guide vane linkages and reduced stagger angle, the range of i was from $13°$ to $53°$. With these two alterations, the following data, similar to that presented in Ref. 19, were taken at the reduced stagger angle and over a greater range of incidence during stall propagation.

Throughout Section 4.1, C_p is defined as the ratio of time average static pressure rise through the cascade to the dynamic pressure of the flow entering, $\dfrac{\bar{p}_2 - p_1}{1/2 \, \rho_1 W_1^2}$, where $\bar{p}_2$ and p_1 are wall static pressures as measured by the average of three equally spaced taps at measuring station 2 and three at station 1. It was determined that each of the boundary layers on the cascade walls was less than one-eighth inch thick before the onset of stall propagation and they are neglected henceforth.

In all the series of schlieren and interferometer photographs such as Fig. 19 and Fig. 25, time is from right to left. All the schlieren photographs were taken at 5000 per second and all the interferometer photographs at 6000 per second.

4.1.2 Experimental Results - Configuration A

Pressure coefficient C_p as a function of β_1 for cascade solidity of unity is shown in Fig. 18 for two levels of Reynolds number Re_1. The conventional $(C_p)_{max}$ is at $\beta_1 = 46°$ in Fig. 18. Subsequent hot wire data and schlieren pictures indicate that periodic stall propagation occurred at the peaks in the curve where β_1 was $54°$, $62°$, $68°$, and for β_1 greater than $79°$. On each side of the peaks the stall cells gradually became

intermittent and of lower amplitude, and between the peaks the flow was relatively steady in time. Visual observation of the flow through the schlieren apparatus for values of β_1 between the peaks of Fig. 18 showed that the flow was completely separated from the suction side of the airfoils.

As β_1 was varied, the mass flow through the test section was held approximately constant; therefore, Reynolds number and Mach number increased with β_1 for each curve plotted, as indicated in Fig. 18.

It is noted in Fig. 18 that there was a distinct effect on C_p caused by change of Reynolds number for $58° < \beta_1 < 74°$. At the lower Reynolds numbers propagation no longer occurred at the band of β_1 centered at $62°$ and the band at $68°$ became narrower. When the Reynolds number was decreased to 50,000 both of these bands disappeared; but propagation at the $54°$ band became more violent and periodic, and the band at $79°$ was not affected noticeably.

Schlieren photographs of the flow were taken in each of the bands of β_1 for which there was stall propagation. The same equipment was used as in Ref. 19, the five inch portable schlieren apparatus of the Gas Turbine Laboratory altered to use an Edgerton Germashausan and Grier type 501 stroboscopic light source and a General Radio Corporation 35 mm. camera. Sections of each of these four films are shown in Fig. 19.

The velocity of propagation and the number of cells in each band of β_1 were determined from the films above and hot wire velocity measurements made upstream of the cascade at 7.69 inches radius. This data is presented in Fig. 20 together with values of V_p/C_{r_1} predicted for a circular cascade by the equation on page 42 of Ref. 19. (Values for β_2 used in this equation were determined by extrapolation from the values measured in schlieren photographs before the onset of stall propagation as was done in Ref. 19.)

Traverses of the hot wire across the span of the cascade airfoils indicated that the flow was two-dimensional for all the bands except for β_1 greater than $79°$ where the velocity fluctuations were about twice as great near the walls as in the center of the blade span. Typical hot wire traces taken at $r = 7.69$ inches for the four bands of propagation are shown in Fig. 21. The hot wire equipment used was a Flow Corporation model HWB hot wire anemometer and another similar unit with hot wires of .003 mm.

diameter and .04" length.

By careful examination of the negatives from which Fig. 19 was made, one can discern the wakes from the upstream guide vanes. It was attempted to make one wake more visible by heating a turning vane with soldering iron filaments brazed to each end. However, no effect could be noticed in the pictures. In Fig. 19A, during the first band of β_1 for which there was propagation, neither these wakes nor the fluid from the adjacent separated airfoils were washed over the leading edges of the airfoils during stall propagation. In Fig. 19B, a turning vane wake just barely flicked over the leading edge of each blade before it stalled and not much of the separated fluid from the adjacent blade was washed over. In Fig. 19C, the same wake as in Fig. 19B crossed back and forth over the leading edge of each blade and more of the separated fluid was washed over. In Fig. 19D, the wakes cannot be detected. It is probable that the wakes and separated fluid injected into the blade boundary layers had an effect on the time required for the blades to stall. This may have caused the great increase of propagation velocity from Fig. 19A to Fig. 19B. This effect is more evident when $\frac{V_p}{c_{\theta_1}}$ is calculated, rather than $\frac{V_p}{c_{r_1}}$. For the bands in order of increasing β_1, $\frac{V_p}{c_{\theta_1}}$ was .13, .26, .28, .25. Thus, $\frac{V_p}{c_{\theta_1}}$ increased by a factor of two from the first to the second band and then remained virtually constant.

Because the stall cells were not all precisely the same size and shape for a given mean flow, there is an uncertainty in measuring V_p and the number of cells. It is believed that the uncertainty in determining the number of cells was less than five for the first band, three for the second and third, and zero for the last band at 71°. The uncertainty in V_p is about 12% for the last band, 8% for the first and less for the other two as indicated in Fig. 20.

When half the blades were removed from the cascade, this being the only alteration, the following experimental results were obtained for configuration A, at a value of $\sigma = 1/2$.

Pressure coefficient C_p versus β_1 is plotted in Fig. 18 so that comparison can be made with the data for σ of unity. It is observed that for $\sigma = 1/2$ there was a mean pressure drop through the cascade for some values of β_1. Hot wire traces showed that the first band of β_1 for

which there was stall propagation was at $54°$ and was very narrow. The signals were never periodic, but were intermittent with occasional lapses to high frequency turbulence. For $60° < \beta_1 < 64°$ a periodic signal was observed as shown in Fig. 21E. For $64° < \beta_1 < 79°$ there were low amplitude, unperiodic fluctuations in the flow which became more distinct for $\beta_1 < 79°$. Traverses of the hot wire indicated that the velocity fluctuations were two-dimensional and periodic only for $60° < \beta_1 < 64°$. In the $54°$ band, velocity fluctuations existed only in the center third of the blade span and for $\beta_1 < 79°$ only in outer thirds of the span near the walls.

Schlieren pictures were taken for $\beta = 60°$ and a section of the film is shown in Fig. 22A. From the film and hot wire traces the number of cells and their velocity of propagation were determined and are indicated in Fig. 20. In Fig. 22A, the wakes from two of the guide vanes are visible. (They have been darkened to aid in reproduction.) From the motion of these wakes it is apparent that the unsteady fluctuations in the flow are large. It is observed that the wakes briefly cross over the leading edges of the cascade blades as they fluctuate. In Figs. 19 and 22A, the boundary layer appears to separate from near the leading edges of the airfoils when they stall and to reattach when they unstall.

When the Reynolds number was lowered below $50,000$ for a value of $\sigma = 1/2$, the velocity fluctuations became non-periodic and of very low amplitude for all the bands of β_1 where stall propagation had existed at higher Reynolds numbers.

In Fig. 22B is seen a section of an interferometer film taken for the same flow geometry as Fig. 22A, although Re_1 and M_1 are higher for Fig. 22B, being $333,000$ and $.47$ respectively. The bands in Fig. 22B indicate lines of constant mean air density, which correspond to lines of constant pressure if isentropic flow can be assumed and lines of constant velocity magnitude where the time rate of change of velocity can be neglected. The striking feature of Fig. 22B is the distinct appearance of the vortices shed from the leading and trailing edges of the airfoils.

4.1.3 Experimental Results - Configuration B

To determine the effect of interference between guide vanes and test cascade, the radii of the test cascade and the static pressure taps

for measuring p_1 and p_2 were increased three quarters of an inch to configuration B. This effectively doubled the clearance between the blade rows and shifted their relative angular position approximately three degrees about the axis of the test section.

In Fig. 23 is plotted C_p versus β_1 for configuration B and σ of unity. Comparison with the corresponding C_p curve for configuration A from Fig. 18 indicates that the increased clearance had no pronounced qualitative effect upon C_p, although values of C_p were generally greater for configuration B. The bands of β_1 where stall propagation existed were shifted a few degrees, which was probably caused by the angular shift of the blade rows from configuration A to B through the effect of the turning vane wakes on the dynamic stall characteristics of the cascade airfoils. There were also detailed effects on the flow caused by the increased clearance. Periodic, two-dimensional stall propagation existed at $\beta_1 = 57°$ and $63°$. Low amplitude, low frequency, unperiodic fluctuations existed for $50° < \beta_1 < 53°$ and for $\beta_1 > 78°$. Flow was relatively steady between the peaks of β_1 in Fig. 23, as was described for Fig. 18. Fig. 24 shows three interferograms of the flow at incidences where the flow was comparatively steady. Interferometer pictures were taken at $\beta_1 = 57°$ and $64°$ and are presented in Fig. 25A, B. The number of stall cells and their velocity of propagation as determined from these pictures are shown in Fig. 23.

When the cascade was assembled with 27 blades ($\sigma = 1/2$), it was found that stall propagation existed for $53° < \beta_1 < 68°$. However, the perturbations were two-dimensional and periodic only for $56° < \beta_1 < 66°$. It was found that decreasing the Reynolds number made the fluctuations less periodic and of lower amplitude. Interferometer pictures were taken for $\beta_1 = 58°$, $61°$ and $64°$, and are presented in Fig. 25A, B, C. (The pictures for $\beta_1 = 61°$ are used to calculate the pressure field during one cycle of the motion in Section 4.1.4.) The following data apply to Fig. 26:

Fig.	$\beta_1°$	Number of Cells	V_p/C_{r_1}	V_p/C_{θ_1}	C_p	Re_1	M_1
26A	58	15-16	.78	.42	.25	266,000	.30
26B	61	19-20	.87	.43	.15	235,000	.37
26C	64	14-15	1.00	.45	.13	200,000	.31

The cascade was reassembled with 18 blades ($\sigma = 1/3$) and it was found that periodic two-dimensional stall propagation existed only for narrow bands of β_1 about $57°$ and $70°$. Interferometer pictures at these two values of β_1 are shown in Fig. 27A, B and the following data apply to them:

Fig.	β_1	Number of Cells	V_p/C_{r_1}	V_p/C_{θ_1}	C_p	Re_1	M_1
27A	57	7-8	1.27	.83	.15	255,000	.31
27B	70	18	1.47	.91	.058	264,000	.32

When the cascade was assembled with nine blades ($\sigma = 1/6$), it was found that hot wire traces upstream of the cascade indicated only varying amplitude high frequency velocity fluctuations as β_1 was increased. At $\beta_1 = 57°$, however, the fluctuations appeared to be intermittently periodic and interferometer pictures were taken as shown in Fig. 28. The frequency with which the blade stalls in Fig. 28 is approximately 790 C.P.S., $Re_1 = 250,000$ and $W_1 = 292$ ft/sec.

In Ref. 6 is described an experimental investigation of the Karman vortex shedding of a flat plate at high incidence i. It was found that for $20° < i < 60°$

$$.164 < \frac{f\ L\ \sin i}{W} < .150,$$

where f is the frequency at which vortices were shed from one edge of the plate. The result of calculating $\frac{f\ L\ \sin i}{W}$ from the preceding data for configuration B and plotting versus σ is shown in Fig. 29. It is observed that, as was shown by a similar plot for $\lambda = 43°$ in Ref. 19, the frequency with which a blade stalls during stall propagation in the cascade appears to approach the Karman vortex shedding frequency of the isolated flat plate as the solidity of the cascade is decreased.

4.1.4 Determination of Flow Properties from Interferograms

From interferometer photographs of a two-dimensional flow, it is possible to determine the pressure field by conventional procedures. The purpose here is to determine the pressure distribution around the circular cascade airfoils and to estimate the strength of the shed

vortices during stall propagation. Also, the pressure distribution before the onset of stall propagation is compared with that of the simulated linear cascade.

The use of interferometry to obtain quantitative information about two-dimensional pressure fields which are unsteady in time is no more difficult in principle than for steady flows, but practical difficulties are encountered in the photography and direct pressure measurement required. As used here, the properly adjusted interferometer produces fringes or bands, such as those in Fig. 26, which indicate lines of constant density. No indication is given in the interferogram of the density level, but only the absolute value of the density differences between fringes. The sign of the density change between fringes is determined from the schlieren pictures and from a qualitative knowledge of the flow. It is necessary to determine independently the value of density at some point in the interferogram at the instant the picture was taken. This is done by the determination of two other independent fluid properties at the point, pressure and entropy. The entropy is assumed constant everywhere in the interferogram (except in the cores of the vortices) and is evaluated upstream of the cascade where the flow is relatively steady and fluid properties can be measured conveniently. The static pressure fluctuations with time are measured at a point in the interferogram with a miniature crystal pressure pickup.

Interferometer

A portable Mach Zehnder interferometer with five inch diameter optical elements, shown in Fig. 30, was used in this study. A detailed discussion of the design and operation of this instrument is given in Ref. 3. Only brief mention of its use will be made here with special reference to the present application.

Fig. 31 is a schematic diagram of the interferometer. Apertures of 1/16 and 3/32 inches diameter were used at the focal point of the collimating lens causing the light to emerge from the lens as a parallel beam. At the first splitting plate the beam is divided into two halves which pass respectively through and around the test section before being recombined at the second splitting plate. The fact that one beam does not traverse the

test section window is compensated for by including in its path two glass plates which are optically similar to those of the test section. The resulting beam is focused on the film. The image produced on the film depends on a comparison between the two optical path lengths.

With no flow in the test section, and a small angular displacement between the splitting plates, a series of parallel interference fringes results. If these bands are originally spaced infinitely far apart, by setting the mirrors exactly parallel, any fringes which appear in the flow picture will be lines of constant density. Some loss of accuracy results from imperfections in the optical elements precluding infinite band spacing. The interferometer optics, test section windows, and compensating plates combined gave a minimum of one fringe instead of the zero number of fringes implied by perfect optics and exactly parallel mirrors.

As shown in Fig. 31, a concentrated light source is required. The source used was an experimental xenon-filled lamp, a photograph of which is shown in Fig. 32. It is capable of flashing for approximately one microsecond at rates of 60 to 8,000 per second when used with the Edgerton, Germeshausen and Grier Type 501 Stroboscopic Modulator. Its small size, large amount of light flux, reliability, and long life made it very satisfactory. The light was filtered to give the monochromatic light necessary to the interferogram evaluation using an interference filter which passed a band of wavelengths 100 $\overset{o}{A}$ wide centered at 4,500 $\overset{o}{A}$.

Pressure Measurement

A miniature crystal pickup capable of sensing high amplitude, high frequency pressure fluctuations is shown in Fig. 33. It is a piezo-electric, barium-titanite crystal in the shape of a hollow cylinder 0.12" long by 0.09" O.D. It is inserted in a drilled hole in one of the optical flats at a measuring point midway between two airfoils shown in Fig. 26B. It is mounted flush with the inner surface and senses the wall static pressure. A drop of glue in the end of the cylinder acts as a safety valve and seals the crystal so that when the test section pressure is applied to its outside surfaces, hoop tension stresses are produced which cause mechanical strains and the accumulation of electrical charge on its inner and outer cylindrical surfaces; a voltage results which is sent through a high

impedance amplifier and displayed on an oscilloscope. Since the impedance of the circuit is not infinite, the charge produced on the crystal faces "leaks off" which prevents its use in measuring low frequency pressure fluctuations.

To determine the rise time of the pickup to a step change in pressure, it was mounted in the wall of a shock tube which is described in Ref. 4. The response of the pickup to a step change of 7.2 psi in pressure and 96°F in temperature is shown in Fig. 34, which indicates that the rise time was less than .05 millisecond, more than adequate for the intended use.

To calibrate the pickup, determine its sensitivity to temperature and observe how quickly electrical charge leaked from the faces of the crystal, a device described in Ref. 11 was used rather than the shock tube because of its convenience and reliability. The device makes of a rotating valve to switch a small test chamber between two large tanks of air at different pressure levels. The crystal and a previously calibrated catenary diaphragm pressure indicator, described in Ref. 11, were subjected to the pressure produced in the test chamber, and the traces shown in Fig. 35 were produced on a dual beam oscilloscope. The diaphragm pressure indicator is insensitive to temperature and has a frequency response which is flat from zero to greater than 20,000 c.p.s. Calculation of an estimated rate of charge leakage from the crystal indicates that the gradual drop in the trace of Fig. 34 (after the rise to the step change in pressure) was predominately the effect of heat conduction into the crystal after the shock wave passed over it and not charge leakage. Since the frequency of the pressure signal to be measured is approximately 600 c.p.s. and the amplitude $\pm$ 1 psi (which corresponds to a $\pm$ 10°F isentropic variation in temperature), it is concluded from a comparison of the traces in Fig. 35 that the crystal is adequate for measuring this signal and that the distortion due to charge leakage and temperature sensitivity can be neglected. It was determined that the mean of the high frequency transient oscillations in Fig. 35 were a measure of the tank pressures which permitted the diaphragm indicator trace to be calibrated. The crystal trace was calibrated by comparing the amplitudes of the high amplitude, high frequency, transient portion of the two traces so that temperature and leakage effects could be neglected during the calibration.

A convenient method of synchronizing the pressure trace on the oscillo-scope with the interferometer photographs is to project both on the same film as in Fig. 26B. With the oscilloscope set so as to suppress the time (horizontal) axis and with the film stationary, the pressure trace is focused on one half the film and set above a convenient reference line in the interferogram, the wire which connects the trailing edges of the blades. With the film in motion, and the time axis thus provided, synchronization is complete. Thus, to determine the amplitude of the pressure fluctuation at the measuring point in an interferogram, it is only necessary to locate the intersection of the wire and trace. Since the crystal does not record a steady pressure, this fluctuating component of pressure must be added to the time mean static pressure measured with a wall static pressure tap directly opposite the crystal location (a 1/8 inch diameter hole drilled in the opposite optical flat). The scale in Fig. 26B indicates the value of the mean pressure and the magnitude of the fluctuating component at the measuring point.

For pressure variations small with respect to the mean pressure, (in the present case $0.9/18$), the maximum error incurred in assuming the pressure at the measuring point to be equal to the mean pressure is small (5%). Of course, it was necessary to first measure these fluctuations to determine whether or not they could be ignored. Pressure distributions other than for Fig. 26B were calculated neglecting the pressure fluctuations at the measuring point.

Measured Pressure Distributions

The most common ordinate in use in the presentation of pressure distributions from steady flows in cascades seems to be $S = \dfrac{P_o - P_{local}}{1/2 \, \rho \, W_1^2}$

That this is also a meaningful parameter for use in unsteady flows may be shown as follows:

In an unsteady flow $\dot{\phi} + p + \dfrac{\rho v^2}{2} = \text{constant} = (p_o)_{-\infty}$ where $\phi \equiv$ velocity potential. If one integrates with respect to time over one cycle and requires that $\dot{\phi}$ make no net contribution for this period (otherwise the time mean value of $(p + \frac{1}{2} \rho \, v^2)$ becomes monotonically increasing or decreasing),

$$\int p \, dt + \int \frac{1}{2} \rho \, v^2 \, dt \equiv C \, T = \left(p_o\right)_{-\infty} \cdot T$$

$$\frac{\int \left(p + \frac{1}{2} \rho \, v^2 \right) dt}{T} = C = \int \frac{p_o dt}{T} = \text{time mean } p_o = \left(p_o\right)_{-\infty}$$

Therefore, for an unsteady flow,

$$S \equiv \frac{\left(p_o\right)_{-\infty} - p}{\frac{1}{2} \rho \, W_1^2} = \frac{\dot{\phi} + \frac{1}{2} \rho \, v^2}{\frac{1}{2} \rho \, W_1^2}$$

Although in a steady flow, S must always be positive, the above discussion shows that in an unsteady flow, S may be negative in certain regions and periods in which $\dot{\phi}$ is a large negative quantity.

The pressure distribution corresponding to each of the ten frames of Fig. 26B for one period $\mathcal{T}$ of the motion are shown in Fig. 36. Generally, they bear little relation in form to the conventional graphs of pressure distribution. This is to be expected, however, for not only is the flow unsteady, but the effect of vortices in the field represents a major departure from conventional flow. Figs. 36-3, -8, -9 show negative values of S. The circled data points in Fig. 36 are obtained from the interferogram fringes of Fig. 26B and by interpolating half fringes between them.

At the beginning of the cycle (frame 1 of Fig. 26B), the blade has shed a counter-clockwise vortex from its trailing edge, and the vortex shed from the leading edge of the preceding blade is coming into view. This latter vortex should have a strong effect upon the blade circulation according to the analysis of Section 3.1.2. One would expect from this analysis that in order for the Kutta condition to be maintained, the circulation around the blade in frame 3, Fig. 26B, must be large. This is verified qualitatively from the pressure distribution of Fig. 36-3 and from Fig. 38, a graph of C_n versus $t/\mathcal{T}$ as determined from the pressure distributions of Fig. 36. On the other hand, the blade circulation decreases as the vortex leaves its leading edge and the effect on the blade pressure distribution is clearly indicated in Fig. 36.

Local incidence angles at the blade were estimated from the schlieren

pictures of Fig. 22A, which show the wakes of the upstream nozzles darkened somewhat for reproduction purposes. These estimated values of i are plotted in Fig 39 versus t/γ . The error caused by the motion of the wakes and the difference in clearance between blade rows in Figs. 22 and 26 is neglected. Using a common time axis t/γ , one may plot C_L as calculated from Fig. 38 versus i from Fig. 39 for information about time lags between local incidence and C_L. Such a plot is shown in Fig. 40 which indicates that a phase lag does exist between i and C_L. This is the usual result, and the explanation seems to be that the presence of a counter-clockwise vortex near the trailing edge has a negative effect on the blade circulation compared to its effect after having been washed downstream and vice versa for the leading edge vortex as shown in Section 3.1.2.

The pressure trace in Fig. 26B clearly shows the presence of the shed vortex. At the beginning of the cycle, when vortices are oriented so as to cause low velocity at the measuring point, the trace indicates high static pressure. At about the fifth frame, when a vortex is quite close to the pressure pickup and oriented such that the velocity is high there, the trace indicates low static pressure.

The magnitude of the blade force calculated from the sequence of Fig. 37 varied from 3 to 7.5 lbs. Although the blade force in the chord direction was calculated, these forces were small enough to be neglected. Hence the normal force is approximately equal to the blade vector force.

With the above experimental information, one can also show the "Böen effect", which is that in the unsteady growth of lift on a wing accompanying a sudden increase in the angle of attack, an increase in the value of maximum lift occurs. Since in Ref. 8, a graph of lift coefficient versus incidence is given, these results may be compared with those of Fig. 40, At an incidence angle of 20° (for which the steady state C_L is a maximum = 0.68 from Ref. 8), Fig. 41 gives values of 0.71 and 1.45 for C_L during the unsteady flow. The maximum value of C_L from Fig. 41 is 2.1. There is some error involved in this comparison since both C_L and C_N are based on the average upstream dynamic head rather than the instantaneous local value; however, the above calculations appear to demonstrate that there is considerable departure from their quasi-steady stall characteristics by the airfoils in question during stall propagation as discussed on page 27.

In order to verify the design technique used to simulate a linear cascade with the circular cascade, the airfoil pressure distribution was calculated for $\beta = 46.4°$ from Fig. 24. The pressure distribution for the equivalent linear cascade (NACA 65-810) is given, for certain combinations of solidity, incidence, etc. in Ref. 8. To compare the two distributions it is only necessary to reduce the circular cascade distribution to that of a linear cascade, using the transformation given in Ref. 9

$$\frac{q_2}{q_1} = \frac{v_2}{v_1} \cdot \frac{r_2}{r_1}$$

where

      q = velocity in the linear cascade

      v = velocity in circular cascade

      r = radius

   $(\quad)_1$ = entry

   $(\quad)_2$ = arbitrary location along the blade in the radial direction

Of course, the comparison must be made for equal values of σ, λ, i, etc. Thus, in Fig. 37, the transformed pressure distribution corresponding to $\beta_1 = 46.4°$ has been compared to the appropriate distribution of Ref. 8. This comparison indicates some success in the attempt in the design of the circular cascade to duplicate the pressure gradients on the suction side of the blades. The apparent difference in blade loading is to be expected from the circular transformation.

Estimation of Strength of Shed Vortices

It is possible to estimate the strength of a vortex moving past a point where the pressure is measured as in Fig. 26B. An advantage of this method is that no measurement is required near the core of the vortex where losses are high, and the strength of an "equivalent potential vortex" can be estimated.

The variation of p, static pressure at the origin, when an isolated vortex Γ moves along a line (y = constant) with the free stream velocity U in an infinite field, can be determined in a coordinate system fixed to the vortex and is given by

$$\frac{p_\infty - p}{\frac{1}{2} \rho U^2} = \frac{\left(\frac{\Gamma}{2\pi a U}\right)^2}{\frac{x^2}{a^2} + 1}$$

where the coordinates of the vortex are $(x, y = a)$.

An estimate of the circulation about an airfoil can be made by using the Kutta relationship,

$$L = \rho W \Gamma_o ,$$

and substituting approximate measured values of L, ρ and W. Applying these two relationships to the ninth frame of Fig. 26B, in which the blade circulation is nearly minimum, (and neglecting the effect of adjacent blades) gives an estimated ratio of blade circulation Γ_o to shed vortex strength Γ of .19. However, because of the inaccuracies involved in this calculation, a direct examination of the interferometer pictures probably yields as good an answer. In Figs. 25 and 26, it is observed that after the airfoils stalled there was virtually no difference in fluid density at points which are at the same chordwise position on the airfoil but on opposite sides. Neglecting the local time rate of change of velocity and losses, this indicates that the pressure and velocity were almost equal at these points and that the circulation about the airfoil must have been small. Therefore, it appears that the circular cascade airfoils shed nearly all of their bound vorticity when they stalled as assumed in the analysis of Section 3.2.1.

4.1.5 Discussion of Results

The experimental results from the circular cascade indicate that stall propagation occurred for narrow bands of mean incidence during which the blades periodically shed nearly all their bound vorticity in the form of discrete vortices. It appears that the airfoils consistently stalled from their leading edges during stall propagation and that between stall cells the flow reattached to the suction side of the airfoils.

Although the washing of the guide vane wakes over the cascade airfoils had an influence on the flow as discussed on page 33, this does not appear to be the reason for the distinct bands of β_1 at which propagation occurred. The effect of Reynolds number on stall propagation was pronounced at some mean incidences but not at others. There was no pronounced effect

on C_p caused by the increase of clearance between blade rows for σ of unity but V_p increased and the number of cells decreased.

The analysis of Ref. 19 predicts that the effect of increased clearance is to decrease V_p but that V_p should increase for fewer cells. The present analysis indicates that the effect of decreasing the extension of the flow field downstream of the circular cascade, which was associated with the increase of clearance, should have caused a tendency for the number of cells to increase. The fact that the number actually decreased indicates that the effect of increased clearance was more important than the effect of decreased downstream field in determining the number of cells in this case.

It is noted that for configuration B, $\frac{V_p}{C_{\Theta_1}}$ was essentially constant for each value of σ but increased as σ decreased. It is probable that this increase was caused in part by the effect of a decreased number of boundary layer time delays (associated with blade stalling). Furthermore, from Fig. 4 it can be seen that the induced effect of the circulation about airfoil a) upon the shed vortex σ tends to decrease its transport velocity. This effect tends to decrease V_p as σ increases independently of the effect of boundary layer time delay. The frequency of stall propagation appears to have approached the Karman vortex frequency for an isolated plate as σ decreased.

It was observed during the experimental work with the circular cascade that some of the stall cell patterns were sensitive to small disturbances on the flow. For instance, in one case (for $\sigma = 1$), stall propagation could be prevented by the insertion of a 1/8 inch diameter hot wire probe upstream of the cascade. On the other hand, at one time during the testing, eight of the fifty-four cascade blades failed and were washed downstream and no pronounced effect was observed on stall propagation except that the flow was slightly less periodic than with uniform blade spacing. Therefore, the stability of the stall cell patterns and the effect on stall propagation of destroying the axial symmetry of the flow appears to vary a great deal with mean flow condition in the circular cascade. No hysteresis or time delay effect could be discerned between the stall cell patterns in the circular cascade and the guide vane setting (incidence).

4.2 Investigation in an Isolated Rotor

4.2.1 Description of Apparatus and Procedure

This investigation was undertaken to extend the available experimental information about the detailed nature of flow through an isolated rotor during stall propagation. The equipment used was virtually the same as described in Ref. 14, where a similar investigation was made for a guide vane-rotor and a guide vane-rotor-stator combination. Fig. 41 is a schematic diagram of the research compressor showing the measuring stations.

The essential dimensions of the single stage axial compressor used in this investigation are:

Hub-tip ratio	0.75
Tip radius	11.63 inches
Mean radius	10.27 inches
Blade chord	1.51 inches (no taper)
Camber angle θ	30.3°
Linear twist, root to tip	9.7°

The blades were a circular arc camber line, with an NACA 0010 thickness distribution (10% maximum thickness at 30% chord).

The rotor blades were unshrouded and the fastening, as shown in Fig. 58, allowed the stagger angle to be easily changed. The constant area annulus extended 29.8 inches upstream and 36.5 inches downstream of the rotor. Radial air flow entrance was through screens. The outflow annulus was a diverging cone. The inner wall cone could be traversed, thereby varying the exit annulus area and throttling the flow.

Three rotor configurations shown in Fig. 43 were tested.

Configuration	Mean Radius Stagger	Mean Radius Solidity
A	30°15'	1.02
B	30°15'	0.51
C	52°45'	1.02

Except where indicated, the rotor was operated at 1500 rpm (U = 134 ft/sec) at mean radius for all configurations.

The relative inlet velocity during stall propagation was 140 to 160 ft/sec, which resulted in a Reynolds number based on the blade chord of 110,000 to 150,000.

The conventional instrumentation consisted of inner and outer wall static pressure taps at five axial positions (C, E, F, FG and G in Fig. 41), kiel probes, a five-hole probe which was used for yaw measurements and sphere-static probes. The pressure measurements were read on an inclined water manometer. The five-hole probe was nulled with the use of a Statham gauge.

The probes used for measuring unsteady velocities were 0.00015 inch diameter by 0.044 inch long tungsten hot wires. The d.c. circuits of two constant current hot wire anemometers were used. The voltage signals from the hot wires were applied directly to a Dumont 304 dual beam oscilloscope. The amplifier and standard calibration procedure of the anemometer* for high frequency fluctuations was not useable, since large, low frequency fluctuations were being investigated. Drift in the d.c. circuitry caused differences in the hot wire calibrations immediately before and after a run of 1/2 hour length as great as 25%. The calibration which came closest to being consistent with the steady-state readings before stall propagation started was used. It is felt that the accuracy is sufficient to indicate certain trends in the data which will be discussed.

Since the hot wire signal indicates only the component of velocity normal to it (over a wide range of angles within a small percentage correction), total velocity, axial component, or tangential component were measured by orienting the wire along radial, tangential, or axial directions respectively (assuming that the radial velocity component can be neglected).

An unsteady angle measuring probe was developed during this investigation. As shown in Fig. 44, it consists of a tube which slips over a standard hot wire probe. The tube is sealed at the end and has two small holes drilled 120° apart at its mid section, similar to a standard cylindrical yaw probe. A thin wall is soldered inside the tube near the hot wire to reduce turbulence.

---

*Model HWB, manufactured by Flow Corporation, Cambridge, Massachusetts.

If the probe is not nulled in a streaming flow, there is flow through the probe which the hot wire senses. This probe is sensitive to low velocities and it can be nulled within $\pm$ 2 degrees. Its response is fast enough to indicate stall cells passing by it. Since the downstream velocity profiles during stall propagation were approximately square wave shapes, one could null the probe by observing the scope trace and thereby measure the angle of flow, either inside or outside the stall cells.

To obtain permanent records of the oscilloscope traces, a Polaroid Corporation camera and a strip film camera were used. The latter is a camera without a shutter but with a constant speed film drive. The number of stall cells or $\emptyset$, the angle at which the cells extended downstream, was determined by the relative displacement of two traces recorded on strip film of hot wires located at different tangential or axial stations.

The stall cell frequency was determined by synchronizing a sine-wave voltage from a frequency generator on the x-axis input with the hot wire velocity signal on the y-axis input of the oscilloscope.

All probe readings except wall static pressures are values at the mean radius unless a radial traverse is indicated. Unsteady static pressure readings are at the outer wall and were measured with two inductance type electrical pressure gauges described in Ref. 15.

4.2.2 Experimental Results - Configuration A

The time average pressure coefficient C_p as determined by the average of the inner and outer wall static pressures and the upstream relative head is plotted in Fig. 45 versus β_c, where

$$C_{P_{CG}} \equiv \frac{P_G - P_C}{\frac{1}{2} \rho W_c^2} \quad \text{and} \quad C_{P_{EF}} \equiv \frac{P_F - P_E}{\frac{1}{2} \rho W_c^2} .$$

Pressures were measured at the stations indicated. W_c and β_c were determined by measuring C_c with a sphere static probe.

The number of stall cells and their velocity of propagation is given in Fig. 46, together with values of V_p predicted in Ref. 19, for no downstream pressure fluctuations,

$$\frac{V_p}{C_x} = \frac{2 \, (\, 1 - C_{pCG})}{\sin 2 \, \beta_c \, (\frac{Ln\pi}{d \, \cos \beta_G} + 1)} \, ,$$ $$\left(n \, \equiv \, \text{number of cells} \right)$$

and the values predicted in Ref. 12 which are the same as in the "channel theory" of Ref. 18 for no phase lag,

$$\frac{V_p}{C_x} = \frac{1}{\sin 2 \, \beta_c} \, .$$

In Fig. 47 are shown unsteady wall static gauge pressures measured at stations E and FG. It is observed that the upstream fluctuations are consistently several times as large as those downstream.

A series of hot wire traces corresponding to measurement of $C_{\theta G}$ and C_{xG} are shown in Fig. 48. Traces for C_{xG} and C_{xE} are shown in Fig. 49. The apparent difference in the average values of C_{xG} and C_{xE} in Fig. 49 is probably due to error in calibration of the hot wires due to "d.c. drift" in the hot wire circuitry as discussed previously, since these values must be constant because of continuity.

In Fig. 50, are given the results of calculating $(W_{\theta G})_o$ and $(W_{\theta G})_i$ from the hot wire traces of Fig. 48. In Fig. 51 are $(C_{xG})_o$ and $(C_{xG})_i$ as calculated from Fig. 49 and C_{xC} from sphere static probe readings.

The measured values of $(C_{xG})_o$ are less than C_{xC} for $\beta_c < 58°$ in Fig. 51. This does not appear to be physically possible because of the blockage effect of the cells. It is felt that again this is a calibration discrepancy since C_{xC} must be the average value of C_{xG} because of continuity. Using this fact, the value of $(C_{xG})_o$ estimated for the hot wire trace at $\beta_c = 56.7°$ is 95 ft/sec. Since all of the data indicate that $(C_{xG})_o$ is essentially constant with throttling except for extremely high values of β_c, it is probably a good approximation to take $(C_{xG})_o$ as constant and equal to 95 ft/sec as indicated in Fig. 51.

$(\alpha_G)_o$, as measured by the hot wire angle probe, β_G as determined by a standard five-hole yaw probe, and $(\beta_G)_o$ are plotted versus β_c in Fig. 52. $(\beta_G)_o$ was calculated from an average value of $(\alpha_G)_o$, 40°, and $(C_{xG})_o$ taken as 95 fps.

From Fig. 50 it is determined that $(W_{\theta G})_i$ was greater by four to eighteen percent than $(W_{\theta G})_o$ (as β_C increases). This result correlates with the experimental observation that the stall cell angle ϕ was negative and smaller than $-15°$ for all the stall cell patterns of configuration A.

4.2.3 Experimental Results - Configuration B

To determine the effect of blade spacing, half the blades of configuration A were removed resulting in configuration B. The number of cells and their propagation velocity are shown in Figs. 65 and 66 which indicate that periodic one and two cell patterns existed for only a narrow range of high incidences for configuration B.

4.2.4 Experimental Results - Configuration C

To ascertain the effect of blade stagger angle, the stagger was increased 22 1/2° from configuration A to configuration C and comparative data taken. The measured results are indicated in the following figures.

Fig. Number	Results Plotted versus β_C	Corresponding Fig. No. for Configuration A
53	C_{pCG} and C_{pEF}	45
54	number of cells, V_p, and predicted V_p	46
55	hot wire traces of C_{xE} and C_{xG}	49
56	1) C_{xC} measured by sphere static probe	51, 52
	2) $(C_{xG})_o$ and $(C_{xG})_i$ as calculated from Fig. 55	
	3) $(C_{xG})_o = 76$ fps as calculated from Fig. 42	
	4) β_G as determined with standard five-hole yaw probe	
	5) $(\alpha_G)_o$ as measured with hot wire angle probe	
	6) $(\beta_G)_o = 45.3°$ calculated taking average $(\alpha_G)_o = 37.5°$ and average $(C_{xG})_o = 76$ fps	

Fig. 42 shows a strip film record of a hot wire trace of axial velocity measured at station G while the throttle was continuously opened

so that the compressor operating condition changed from two, to one, to zero cells. For $(C_{xG})_o$, the trace is at the top edge of the film for the entire strip. During this strip film, which took about five seconds, d.c. amplifier drift was negligible. (The calibration was checked immediately after the run, and it had not changed during the run.) The value of $(C_{xG})_o$ is observed to be almost constant and is. calculated to be 76 fps, which compares well with the average of the values from the hot wire traces of Fig.55.

For configuration C, the angle ϕ between the stall cells and rotor axis was determined from the measurement of phase lag between two traces of hot wires inserted at stations G and K. It was determined that for the one cell pattern $\phi = 19°$ and for the two cell pattern $\phi = 16°$. The error of measurement probably was less than 10%.

4.2.5 Comments on Compressor Operation

Just before rotating stall started as the throttle was closed, a "mushy" flow, as it has been called, was observed near the hub and tip as indicated by a "hashy" hot wire trace. A very weak rotating stall might have been present at the hub for configuration C. The relative magnitudes of the mush at 1/4 inch from the hub and rotating stall of one cell can be seen from hot wire traces of Fig. 57 for configuration C. The mush was less than 1/5 the amplitude of rotating stall and was not investigated further. Rotating stall measurements were taken through the operating range until surge started. Although unperiodic propagation could still be observed along with the surge (since surge was of much lower frequency), no attempt was made to take data and separate the two effects. The variation of velocity fluctuation with axial distance from the rotor was measured at one operating condition for configuration A as is shown in Fig. 59. It is noted that the amplitude of the velocity fluctuations decreased rapidly with distance upstream but that they persist much farther downstream. At station K, 26 inches downstream, the amplitude of the fluctuations are about 1/2 those at station G.

Upon throttling the flow, rotating stall always started as two cells, then as the flow was increased, the two cells changed to one. However, if the axial symmetry of the flow was destroyed by placing an

obstacle (such as the observer's hand) in the inlet or outlet of the compressor, the one cell pattern could be forced to appear before the two cell pattern as the flow was throttled.

If the compressor were operated at a value of β_C where the number of stall cells changed, the cell pattern sometimes shifted back and forth between the two numbers of cells.

Radial traverses of the hot wire during stall propagation indicated that the flow was fairly two-dimensional for all the observed stall cell patterns, although in some cases an estimated 25% smaller fluctuation in velocity was observed at the hub.

To determine the effect of Reynolds number on rotating stall character-istics, the rotor speed was held at 500, 750, 1000, 2000, and 2500 RPM, and the flow throttled. A comparison of the number of cells and propagation velocity at three speeds is shown in Figs. 60 and 61 as functions of β_C. "Constant geometry" runs were made for two constant throttle settings and rotor RPM variation. The results of these runs and the previous are shown in Fig. 62, a plot of the number of cells and β_C as a function of Re_C. As indicated in these figures, there is a hysteresis effect between the number of cells for some values of Re_C and β_C. The data points at minimum β_C indicate the onset of stall propagation and the points at maximum β_C indicate the end of periodic stall propagation. (For higher values of β_C high frequency velocity disturbances and surge existed.) The data plotted in Figs. 60, 61 and 62 indicate that there was not much effect of Reynolds number above 100,000 or 1500 RPM, but that for lower values the range of β_C for which periodic propagation existed is shifted up. As Reynolds number was lowered, the one cell and then the two cell patterns disappeared, but there was not much effect upon propagation velocity. It was found that there was virtually no difference in $C_{P_{CG}}$ at corresponding values of β_C for 500 RPM and 1500 RPM.

Axial velocity profiles as determined from measurements made with a standard five-hole yaw probe for configuration C are shown in Fig. 63. They indicate that there is some error involved in assuming mean radius measurements to be representative but that this error is less during than before the onset of stall propagation. The difference in area under the

profiles measured during stall propagation indicates the error inherent in using a standard five-hole probe in an unsteady flow.

4.2.6 Discussion of Results

The hot wire measurements of Figs. 49 and 55 indicate that the downstream axial velocity profile can be approximated with a square wave which changes with throttling only along the abscissa. That is, $(C_{x_G})_o$ and $(C_{x_G})_i$ in Figs. 50 and 56 remain essentially constant with β_C and of approximately 4/1 ratio, but the number of cells and the width of the cells change such that their blockage effect increases continuously with throttling. The data appears to correlate with that from Ref. 2 in indicating that during stall propagation the velocity triangles outside stall cells were nearly the same as for $C_{p_{max}}$ (before the onset of stall propagation).

The unsteady pressure measurements of Fig. 47 indicate that the fluctuations were several times as great one inch upstream of the rotor as they are 5.6 inches downstream. (When a pressure gauge was inserted seven inches downstream at station G, virtually no fluctuations could be observed in the trace.) As a stall cell approached the upstream gauge, the static pressure at this point rose to a value greater than the absolute total head far upstream but less than the total head relative to a coordinate system fixed to the stall cell pattern. The static pressure then dropped as the stall cell passed by the gauge. There was a pressure drop through the rotor in the stall cells. This qualitative description of the pressure field is predictable from the flow model used in the analysis of Section 3.2 from a consideration of the velocities induced by the stall cell in a coordinate system fixed to the stall cell pattern.

The hot wire traces for C_{x_E} in Figs. 49 and 55 indicate that as β_C increased, the cells grew wider and that the axial velocity profile just upstream of the rotor changed shape as they grew wider. The "sag" in the profile caused by the blockage of stall cell changed from a spike form for a thin cell to a double spike indicating that there was more flow through the center of the wide cell than near its edges. Since the trace did not ever go to zero (the minimum value being 25 ft/sec), in no case was there flow reversal at station E during stall propagation. This fact was verified independently of the calibration of Figs. 49 and 55 by quickly pulling

the hot wire at station E out of the compressor and observing that for zero
air velocity the trace went considerably lower than the minimum displacement
for the "double spike" wave form during stall propagation. A check was also
made by quickly turning the wire 90° from a tangential to axial direction
and observing the same result as above for zero velocity normal to the wire.
The number of cells is observed to increase after the double spike form
appeared, which suggests that the double spike form split into two cells,
a tendency predicted by the preceding analysis. From the strip film
trace of Fig. 42, it is observed that the opposite sequence occurred when
the flow was increased through the rotor running at constant RPM. At first
there were two stall cells 180° apart, then the cells gradually moved to-
gether forming a double spike pattern and then a single spike pattern.

The hot wire traces of Figs. 42, 49 and 55 show that the shape of
the stall cell pattern is not perfectly constant in time or axisymmetric
(as assumed in the analysis for a given mean flow and even number of cells).
This fact appears to explain why one cell of a two cell pattern might split
and thus form a three cell pattern as the flow is throttled instead of both
cells splitting simultaneously. However, the trend for the observed shapes
of the stall cell pattern with throttling appears to correspond qualitatively
with the trend predicted by the analysis of Section 3.2.3.

In Figs. 65 and 66 $\frac{V_p}{C_{x_c}}$ and $\frac{V_Q}{U}$ as functions of β_c are compared for
configurations A, B, and C, and for data from Ref. 2. It is observed that
all stall cell patterns observed herein revolved at .48 U < V_Q < .59 U,
or approximately half wheel speed. In Fig. 65, V_p increased slightly when
the solidity of the cascade was reduced in agreement with the trend ob-
served in the circular cascade.

Not much effect on propagation velocity occurred with the change of
stagger angle or with Reynolds number change above 100,000. However,
the number of cells was greatly affected by the change of solidity, of
stagger, and of Reynolds number below 100,000.

The propagation velocities predicted by the small perturbation
theories of Ref. 12, Ref. 18 (no phase lag), and Ref. 19 as shown in
Figs. 46 and 54 appear to overestimate the experimental values by as much
as 50%. The correlation of the data with the theory of Ref. 19 appears

to be well described by the correlation predicted on page 24 of that reference.

> "The values of propagation velocity predicted when the boundary-
> layer delay is neglected should be larger than those obtained
> experimentally, with the difference most pronounced for the
> case of disturbances covering only a few airfoils when the
> boundary-layer delay will have an important effect. An increase
> in the wave length of the stall cells should be accompanied by
> an increase in propagation velocity, if other variables are
> unchanged."

The effect of number of cells on propagation velocity as predicted in
Ref. 19 appears to be borne out quite conclusively by the data plotted in
Figs. 46 and 54.

In Fig. 64 is plotted versus β_C, the function

$$A = \text{discharge} \quad \text{coefficient} \equiv \frac{\cos \beta_C}{\cos \beta_G (1 - C_{P_{CG}})^{1/2}}$$

The values of β_G were those determined with the standard yaw probe. In
Refs. 5 and 19 it was predicted that small perturbation stall cells may
form when the slope of this curve passes through the origin. There seems
to be fair agreement from Fig. 64 with this prediction.

Is is observed in Figs. 45 and 53 that the slopes of the curves of
C_p versus β_C for configurations A and C both approached zero when stall
propagation occurred.

In Ref. 2 tests were made with a rotor of solidity equal unity,
28.5° stagger, NACA 65(12)10 airfoils, and hub-tip ratio of 0.9. As shown
in Fig. 66, there is overall qualitative agreement between the data for
configuration A and that in Ref. 2. Stall propagation started at nearly
the same incidence and V_Q/U was nearly the same, but there were differences
in the number of cells and the measured pressure fluctuations. In Ref. 2
it is reported that the pressure fluctuations downstream were about 60%
of those upstream. In the present investigation, they are found to be three
to five times as great upstream as downstream; however, the gauges are
closer together than in Ref. 2, and the cells extend more uniformly from
root to tip than the two and three cell patterns of Ref. 2.

5 Correlation of Analytical and Experimental Results

Verification of the assumptions made in the analysis appears from the following experimental results:

1) From Figs. 19, 22, 25, 26 and 27, it is observed that during stall propagation the blades in the circular cascade shed discrete vortices upon entering or leaving stall cells and lose nearly all their bound vorticity when they enter the cells.

2) From the approximate square wave shape of the velocity profiles downstream of the rotor during stall propagation, as indicated by the hot wire traces of Figs. 49 and 55, it appears that the vortex flow model of Section 3 may be used to represent the actual flow through the rotor. Furthermore, the square wave shape of the downstream velocity profiles tends to support the idea that the rotor blades stalled from their leading edges as the blades in the circular cascade are observed to have done. In Ref. 7, page 66, it is shown that the rate at which vorticity is shed from an airfoil is $V^2/2$ where V is the free stream velocity at the separation point of the boundary layer. Since immediately downstream of the rotor blades the vorticity is observed to have been concentrated along the stall cell boundaries, it might be argued that in order for the blades to have shed vorticity quickly enough to have established this pattern, the point at which the boundary layer separated must have been located where V was large, near the leading edge. The validity of this speculation is not essential, however, since the present analysis is independent of the location of separation.

3) The observation from Section 4.2 that the ratio of downstream axial velocity outside the cell is about four times as great as inside indicates that the approximation of $N = M = 1$ in the analysis may be a reasonable one in view of the discussion on page 20 which indicates that this approximation is not critical to the resulting prediction for V_p.

In the present analysis, an approximation is made for the flow far downstream of a continuous blade row during stall propagation. The results of the analysis indicate why some observers have found incongruous experimental results from linear cascades of finite length as reported in private communication with the author. It appears that, as was first

described in Ref. 18, the blade stall-unstall characteristics depend strongly on the nature of the unsteady flow induced upon them by the downstream flow pattern. In a linear cascade of finite length, the downstream flow pattern is quite different from that for a continuous circular cascade or a rotor. Even though there may be many blades in the linear cascade, a fully developed, translating, downstream flow pattern as described in the analysis is precluded by the end wall effects. Therefore, the present analysis is valid only for an infinitely long linear cascade, or an isolated rotor, where the downstream flow field extends far from the cascade.

The tendency for the stall cell to split into two as its width increases, as predicted by the analytical flow model, appears to be supported by the measured axial velocity profiles just upstream of the rotor given in Figs. 50 and 55. Furthermore, this tendency might explain why smaller stall cells (greater numbers of cells) existed in the circular cascade than in the rotor. Since the two-dimensional flow field of the circular cascade extended only a few blade chords downstream of the cascade, the discussion of page 28 indicates that the cells should be thinner (n less in Fig. 9) than for the rotor. This fact, together with the assumption that there must be enough total blockage from the cells to cause $(W_2)_0$ to be nearly the same as for $C_{P_{max}}$ (as observed for the rotor), implies that there should be a greater number of cells in the circular cascade than the rotor.

Equation (12) shows that for the vortex flow model assumed in the analysis, stall cells can exist only for

$$C_p > \cos^2\beta_1.$$

In Fig. 67 this minimum value of C_p is plotted versus β_1. Measured values of C_p are plotted for increasing β_1 until the onset of stall propagation.

Propagation started after $C_p > \cos^2\beta_1$ in the three rotors tested. (This was not always true for the circular cascade.)

Equation (11) shows that for the assumed type of propagation to exist, $W_{\theta_1} > W_2$. If it is assumed that $C_{x_1} = C_{x_2}$ and $\beta_2 = \lambda$, this condition becomes cotan $\beta_1 < \cos \lambda$ giving a minimum value of β_1 for which stall propagation can exist in a cascade of stagger λ. This minimum value of β_1 and the corresponding measured values of β_1 where stall propagation

started in the test rigs are plotted in Fig. 68. Also plotted is cotan β_1 = .866 cos λ (which gives $V_p = \frac{W_{\theta_1}}{2}$ from Equation (11) if $C_{x_1} = C_{x_2}$ and $\beta_2 = \lambda$). It appears that this latter curv? correlates rather well with the values of β_1 where stall propagation actually began in the test rigs.

Predicted values of propagation velocity for the vortex flow model of Section 3 are given by Equations (11) and (12). Correlation of the rotor data with Equation (12) is shown in Figs. 46 and 54 where $C_{p_{CG}}$ from Figs. 45 and 53 was used. Correlation of the data from Ref. 2 with Equation (12) is shown in Table III where $C_{p_{3-7}}$ from that reference was used. It appears that the predicted values of V_p from Equation (12) are considerably greater than the measured values. It is felt that the reason for this trend lies in the fact that $p_2 - p_1$ was assumed to be given by isentropic flow outside stall cells in developing Equation (12). The presence of blade wakes in the actual flow outside the stall cells causes $(\beta_2)_o$ to be less for a given measured Δp than in the assumed ideal flow. Therefore, for a measured Δp, V_p should be less than predicted by Equation (12).

Using the average measured values for $(\beta_G)_o$ and $(C_{x_G})_o$ indicated in Figs. 51, 52, and 56, one calculates V_Q/U from Equation (11) to be .57 for Configuration A and .60 for Configuration B. The correlation with the measured values of V_Q/U as shown in Fig. 66 appears to be good considering the accuracy of measurement, the departure of the flow from two-dimensionality, and the simplifying assumptions in the analysis. Equation (11) appears to predict propagation velocities more closely than Equation (12), probably because it is less sensitive to the effect of blade wakes outside stall cells.

In Table III is shown the correlation of data from Ref. 2 with Equation (11) using $C_{p_{3-7}}$ from Ref. 2 and assuming:

$$(\beta_G)_o = \text{const} = 28.5° = \lambda \quad , \quad C_{x_1} = (C_{x_2})_o$$

for the two and three cell patterns, and $C_{x_1} = .8(C_{x_2})_o$ for the one cell pattern; which are estimates based upon the data presented in Ref. 2.

TABLE III

β_1	$c_{p_{3-7}}$	Number of Cells	$(\frac{Vp}{C_{x_1}})_{meas.}$	$(\frac{Vp}{C_{x_1}})_{eqn.\ 12}$	$(\frac{Vp}{C_{x_1}})_{eqn.\ 11}$
55°	.46	2	.53	.80	.58
56	.43	3	.48	.87	.54
58	.33	1	.89	1.19	.87

In Table IV is shown the correlation of data from the circular cascade with Equation (12)

TABLE IV

Ref. 19, = 1

β_1	c_p	Number of Cells	$(\frac{Vp}{C_{r_1}})_{meas.}$	$(\frac{Vp}{C_{x_1}})_{eqn.\ 12}$
63°	.48	9	.60	.80
64	.46	9	.64	.86
66	.41[x]	10-12	.70	1.03
68	.36[x]	12	.70	1.22

x (extrapolated from data)

Configuration A, = 1

β_1°	c_p	Number of Cells	$(\frac{Vp}{C_{r_1}})_{meas.}$	$(\frac{Vp}{C_{x_1}})$ eqn. 12
55°	.33	15-20	.24	1.4
60	.29	13-14	.54	1.3
68	.25	16	.75	1.6
81	.12	5	1.6	4.3

Configuration B, = 1

β_1	c_p	Number of Cells	$(\frac{Vp}{C_{r_1}})_{meas.}$	$(\frac{Vp}{C_{x_1}})_{eqn.\ 12}$
58°	.45	9-10	.55	.82
64	.36	11	.83	1.6

It is observed that Equation (12) overestimates the measured values of $\frac{Vp}{C_{x_1}}$ considerably for the circular cascade. However, good correlation cannot be expected since the assumption in the analysis that the flow field extends infinitely far downstream of the cascade is not a valid approximation for the circular cascade. Furthermore, the analysis is not valid for a radial flow field.

In Table V is shown the correlation with Equation (12) of data from Ref. 14 for a guide vane-rotor stage relative to the rotor.

TABLE V

β_1°	C_p	No. of Cells	$(\frac{Vp}{C_{x_1}})_{meas}$	$(\frac{Vp}{C_{x_1}})_{eqn.\ 12}$
67.5	.30	8	.9	1.4
72.5	.25	9	1.1	1.8
75.0	.23^x	1	2.3	2.2
77.5	.20^x	1	3.0	2.8
80.0	.16^x	3	3.0	3.6

6   Summary and Suggestions for Future Research

Using approximations suggested by visual observation of the flow through a circular cascade, a vortex flow model of stall propagation in an isolated blade row has been developed. Equation (11) derived from analysis of the vortex flow model, appears to predict the propagation velocities measured in an isolated rotor within 15%. Stall cell configurations observed in an isolated rotor were found to be nearly two-dimensional and to propagate at approximately half wheel speed. The stall cells consisted of regions where the axial velocity was small and extended downstream from the rotor in a direction parallel to the rotor axis within $\pm 20°$.

The number of cells increased as the flow through the rotor was throttled. A qualitative prediction of the analysis is that a stall cell of the type assumed should have a tendency to split into two cells as it grows in peripheral extent. This tendency may be the reason for the observed trend in the number of cells.

It appears that the most fruitful areas for future analytical work will be further investigation of the mechanism which determines the number of cells and extension of the analysis to include flows which are not two-dimensional, such as caused by "tip cells" or"hub cells." The interference effect of one blade row on another during stall propagation may be attacked by the method used in the present analysis by assuming the blades to shed potential vortices and determining the effect on the blade rows of the vortices as they are convected downstream.

It is suggested that future experimental work should include an investigation of the effect of airfoil profile on stall propagation in the circular cascade and rotor. It appears that alteration of the single stage research compressor so that two widely separated rotors could be installed would be useful because it would permit a wider range of flow geometry relative to one of the rotors(or rotor-stator combinations). It is also suggested that further investigation of the effect on cascade stall characteristics of the time rate of change of incidence should lead to a better understanding of the dynamic stall characteristics of the cascade during stall propagation.

LIST OF SYMBOLS

$\overset{\circ}{A}$ angstroms

A $\cos \beta_1 / \cos \beta_2 \sqrt{1 - C_p}$ = discharge coefficient

a vortex spacing along stall cell downstream of blade row

C absolute velocity

C_p static pressure coefficient of cascade $= \dfrac{p_2 - p_1}{1/2 \, \rho \, W_1^2}$

C_L blade lift coefficient $= \dfrac{\text{Lift/Area}}{1/2 \, p \, W_1^2}$

C_N blade normal force coefficient $= \dfrac{\text{aerodynamic force normal to chord}}{1/2 \, \rho \, W_1^2}$

d length of cascade or circumference of rotor

$f(\quad)$ function of; frequency

i incidence $= \beta - \lambda$

K defined by Equation (7)

L blade chord

M Γ / Γ_0 ; Mach number

m length of stall cell in vortex spaces a

N $\dfrac{V_1 \cos \phi}{W_{x_2}}$

n width of stall cell downstream of blade row in vortex spaces a

p static pressure

r radius; polar coordinate

s cascade blade spacing

R radius; radius of cylinder in picture plane $= \dfrac{L}{4}$

Re Reynolds number based on blade chord, $\dfrac{\rho \, W \, L}{\mu}$

$\mathfrak{R}$ real part of

S $\dfrac{\text{time mean } p_0 - p}{1/2 \, \rho \, W_1^2}$

t time

u, v velocity components

U rotor velocity at mean radius $= W_{\theta_1}$ for isolated rotor

V velocity; transport velocity of vortex downstream of blade row

V_a velocity of vortex Γ along lines b) and c) in Fig. 10

V_p velocity of stall propagation relative to blade row

V_Q absolute   velocity of stall propagation $= U - V_p$

V_i velocity induced by stall cell $= \dfrac{\Gamma}{a}$

W complex velocity potential in picture plane; velocity relative to cascade or rotor

X $\dfrac{W_{x_1}}{W_{x_2}}$

Y fraction of downstream periphery covered by stall cells $= \dfrac{na}{d \cos \phi}$

z $= x + i\,y$, complex coordinate in physical plane

α angle of flow from axial direction in absolute coordinate system

β angle of flow from axial direction in coordinate system fixed to blade row

σ cascade solidity $= L/s$

λ cascade stagger angle from blade chord to axial direction

τ period with which stall cells pass a fixed point

Γ strength of shed vortex

Γ_o strength of bound vortex

θ polar coordinate; blade camber angle

ϕ angle of stall cell from axial direction

ζ $= \xi + i\,\eta$ complex coordinate in picture plane

$(\ )_o$ stagnation point; outside stall cell

$(\ )_i$ inside stall cell

$(\ )_1$ far upstream; upstream measuring station in circular cascade

$(\ )_2$ far downstream; downstream measuring station in circular cascade

$(\overline{\ \ })$ complex conjugate of $(\quad)$

$f'(x)$ $\dfrac{df}{dx}$

$(\overset{o}{\ })$ $\partial(\ )/\partial t$

$(\ )_x$ axial component of $(\quad)$ (Note, $C_x = W_x$)

$(\ )_r$ radial component of $(\quad)$

$(\ )_\theta$ tangential component of $(\quad)$

$(\ )_{C,\ E,\ F,\ FG,\ G,\ K}$ measuring stations along axis of rotor shown in Fig. 41

BIBLIOGRAPHY

1. Anton, L., "Formation of a Vortex at the Edge of a Plate", NACA TM 1398, March 1956.

2. Costilow, E.L. and Huppert, M.C., "Rotating Stall Characteristics of a Rotor with High Hub-Tip Radius Ratio", NACA TN 3518.

3. DeFrate, L.A., Barry, F.W. and Bailey, D.Z., "A Portable Mach-Zehnder Interferometer", Meteor Report No. 51, M.I.T. Guided Missiles Program, February 1950.

4. Draper, C.S., McKay, W. and Lees, S., "Instrument Engineering", New York, McGraw Hill Book Company, 1953.

5. Emmons, H.W., Pearson, C.E. and Grant, H.P., "Compressor Surge and Stall Propagation", Transactions of the ASME, May 1955, pp. 455-467.

6. Fage, A., and Johansen, F.C., "On the Flow of Air Behind an Inclined Flat Plate of Infinite Span", Proceedings of the Royal Society, London, Vol. 116, p. 170, September 1927.

7. Goldstein, S., "Modern Developments in Fluid Dynamics", Vol. 1, Oxford Press, London, 1952.

8. Herrig, L.J., Emery, J.C. and Erwin, J.R., "Systematic Two Dimensional Cascade Tests of NACA 65-Series Compressor Blades at Low Speeds", NACA RM L51G31, September 1951.

9. Kriebel, A.R. and Stenning, A.H., "A Test Apparatus for Stall Propagation Study", Report No. 26, Gas Turbine Laboratory, Massachusetts Institute of Technology, August 1954.

10. Lin, C.C., "On the Motion of Vortices in Two Dimensions", Applied Mathematics Series No. 5, University of Toronto Studies, The University of Toronto Press, 1943.

11. Livengood, J.C., "Improvement of Accuracy of Balanced Pressure Indicators and Development of an Indicator Calibrating Machine", NACA TN 1896, June 1949.

12. Marble, F.E., "Propagation of Stall in a Compressor Blade Row", California Institute of Technology, Technical Report No. 4.

13. Milne-Thomson, L.M., "Theoretical Aerodynamics", D. Van Nostrand Company, Inc., New York, 1948.

14. Montgomery, S.R. and Braun, J.J., "An Investigation of Rotating Stall in a Single Stage Axial Compressor", Report No. 29, Gas Turbine Laboratory, Massachusetts Institute of Technology, May 1955.

BIBLIOGRAPHY (Continued)

15. Patterson, J.L., "A Miniature Electrical Pressure Gauge Utilizing a Stretched Flat Diaphragm", NACA TN 2659, April 1952.

16. Prandtl and Tietjens, "Fundamentals of Hydro and Aerodynamics", McGraw Hill Book Company, Inc., New York, 1934.

17. Schlichting, H., "Berechnung der reibungslosen inkompressiblen Stroemung fuer ein vorgegebenes ebenes Schaufelgitter", VDI Forschungsheft 447, 1955.

18. Sears, W.R., "A Theory of Rotating Stall in Axial-Flow Compressors", Cornell University, Graduate School of Aeronautical Engineering, January 1953.

19. Stenning, A.H., Kriebel, A.R. and Montgomery, S.R., "Stall Propagation in Axial Compressors", NACA TN 3580, June 1956.
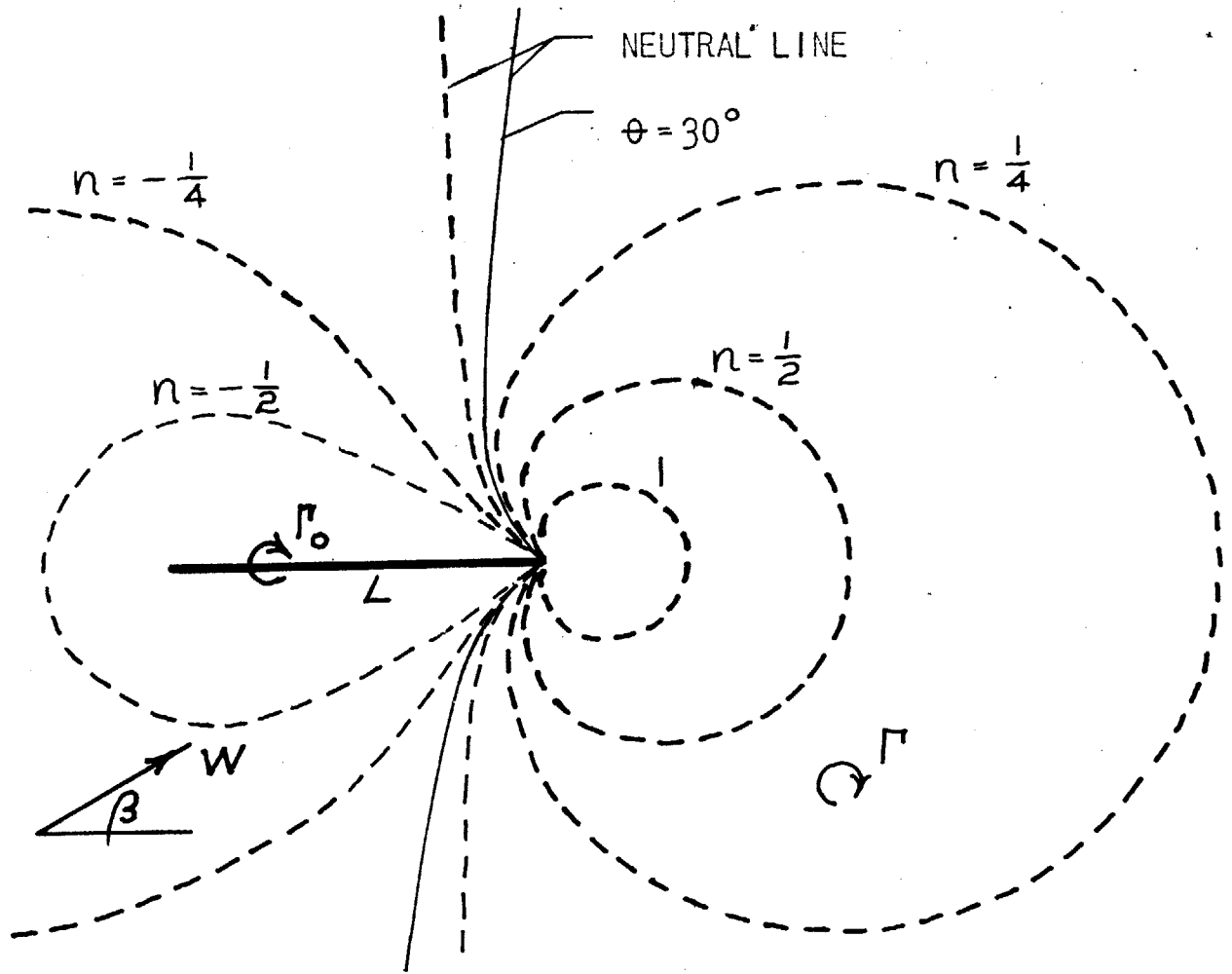
FIG. 1   LOCI OF VORTEX Γ FOR CONSTANT PLATE CIRCULATION
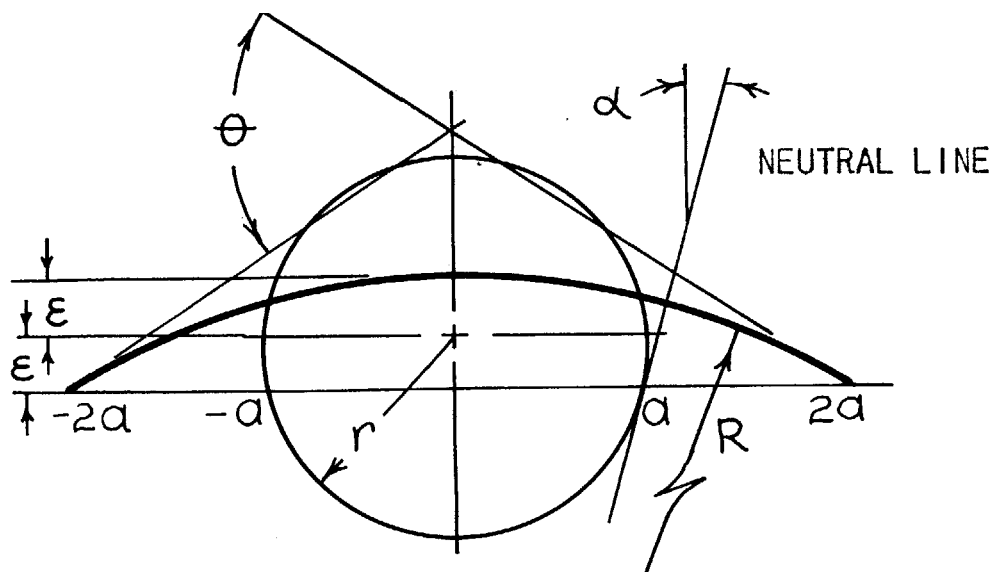
FIG. 2   JOUKOWSKI TRANSFORMATION OF CIRCULAR ARC
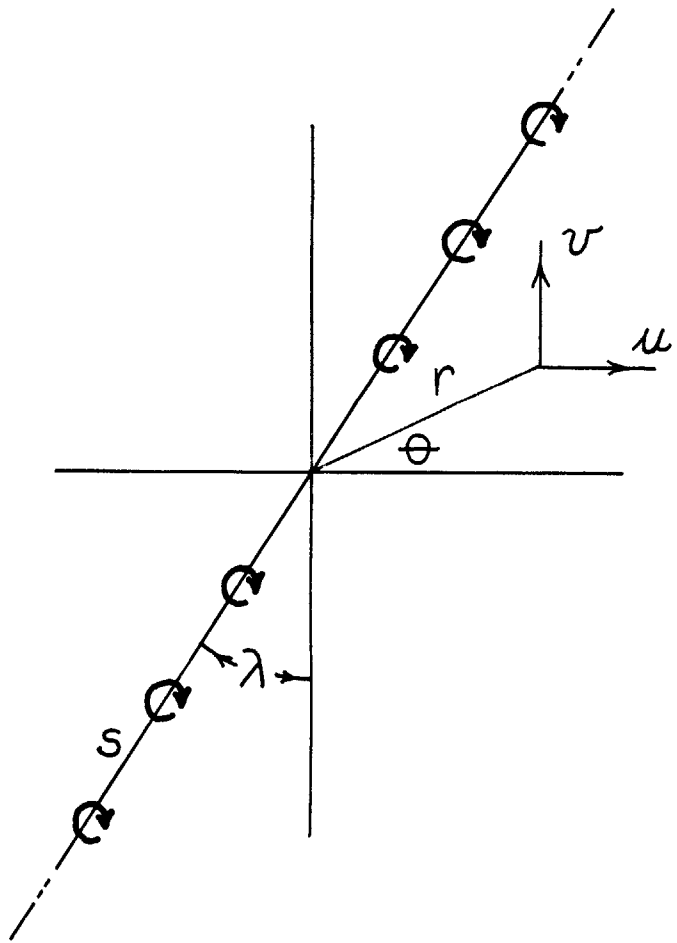
FIG. 3   VORTEX REPRESENTATION OF CASCADE

$\beta_1 = 60.0°$

$\beta_2 = 49.8°$

$\beta_m = 55.5°$

$\lambda = 30°$

$\sigma = \dfrac{1}{2}$
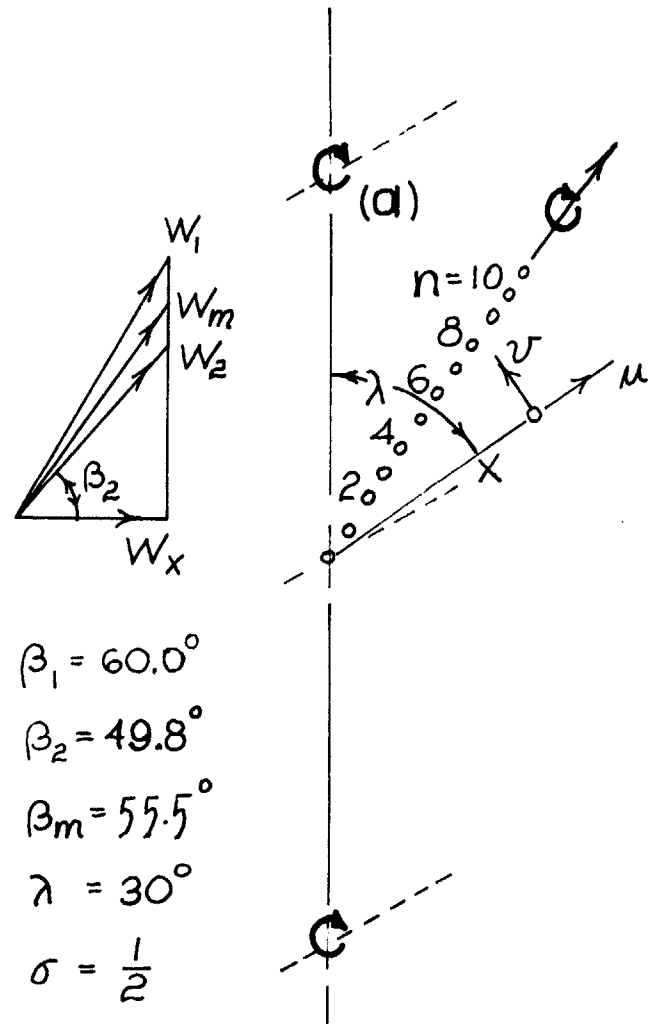
FIG. 4   LOCATION OF SHED VORTEX
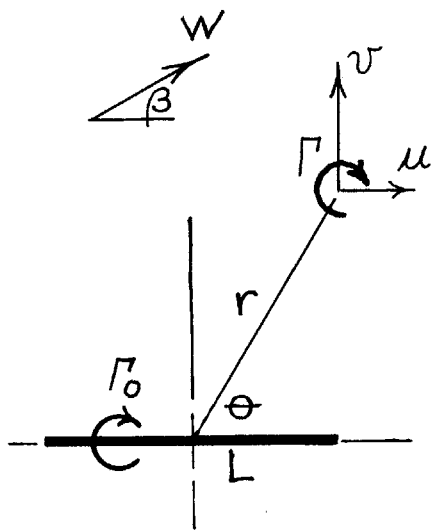
FIG. 5   VORTEX NEAR FLAT PLATE
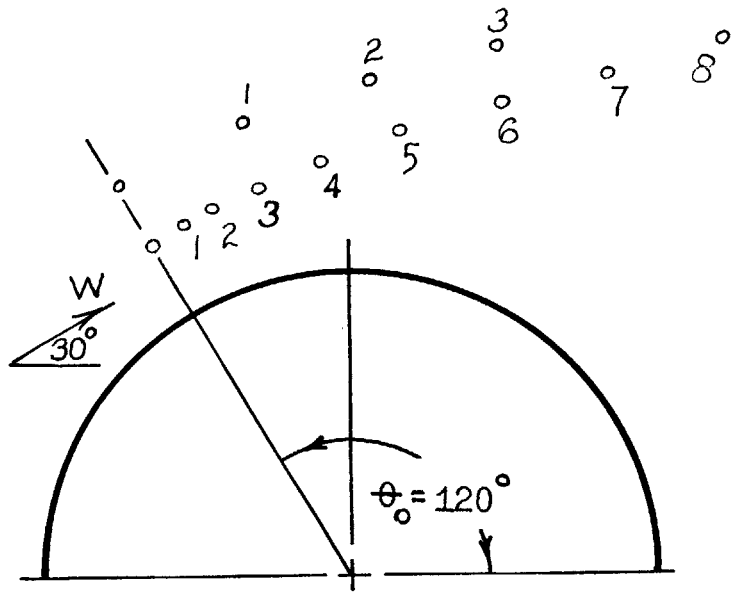
FIG. 6   LOCATIONS OF VORTEX
FOR TWO INITIAL POINTS
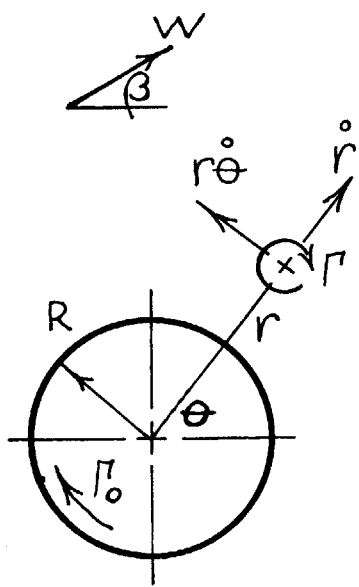
FIG. 7   VORTEX NEAR CYLINDER
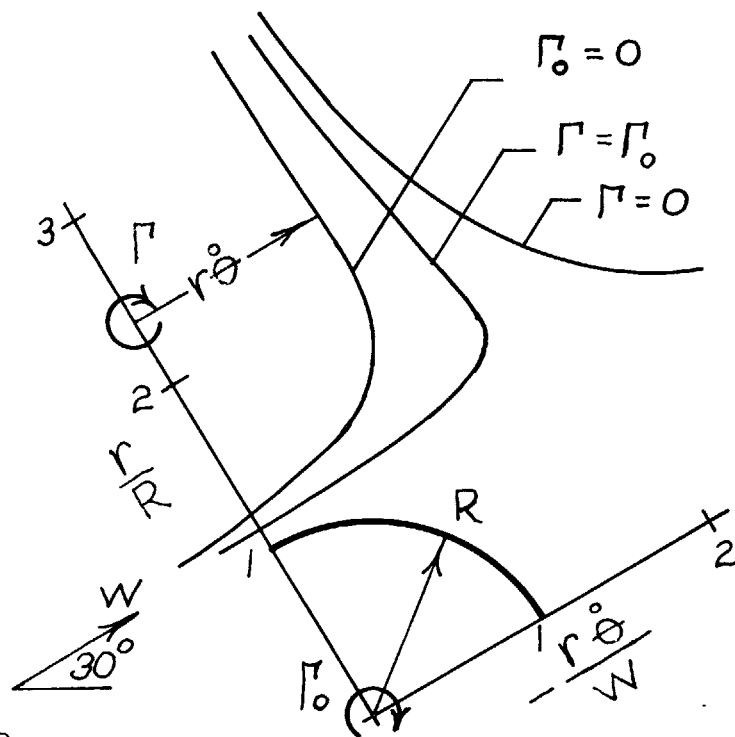
FIG. 8   VELOCITY OF VORTEX NEAR CYLINDER
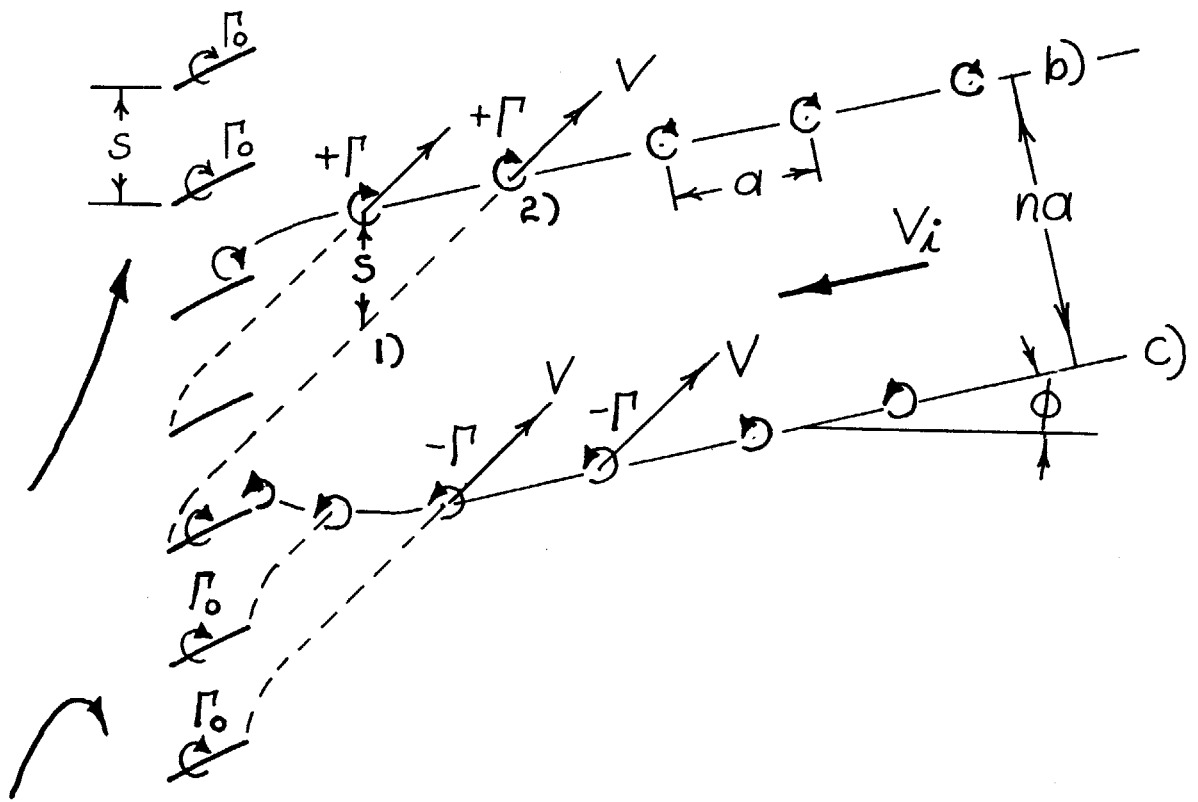
FIG. 9 PATTERN OF VORTICES IN STALL CELL
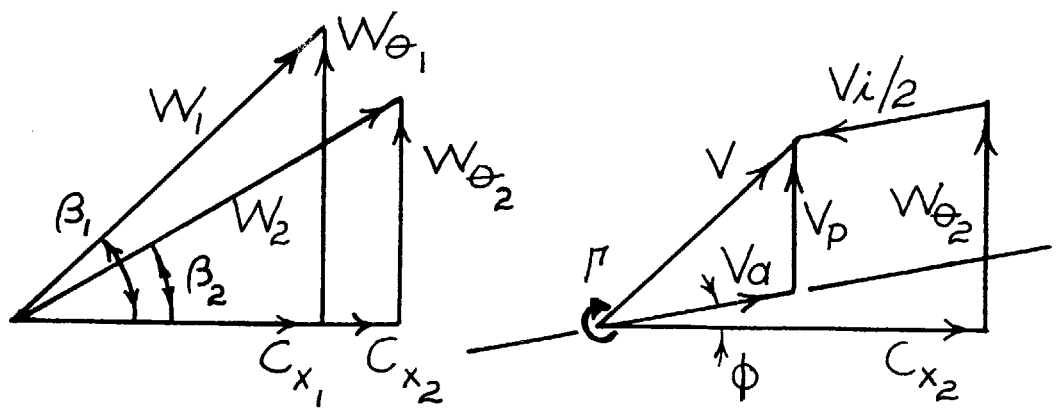
FIG. 10 VELOCITY TRIANGLES FOR STALL CELL
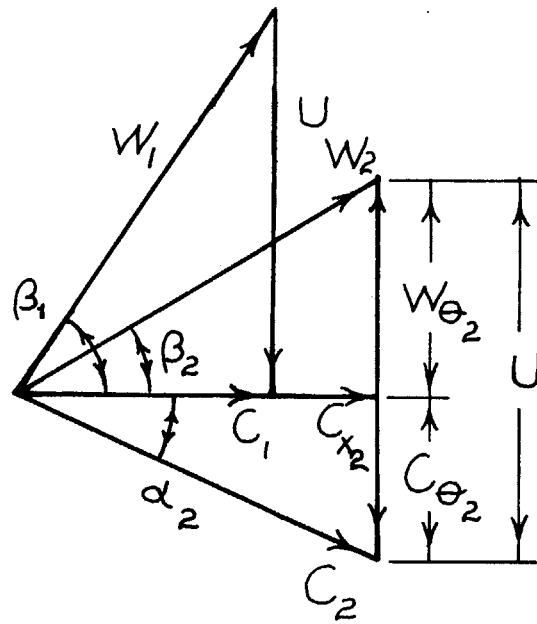
FIG. 11 VELOCITY TRIANGLES FOR ISOLATED ROTOR
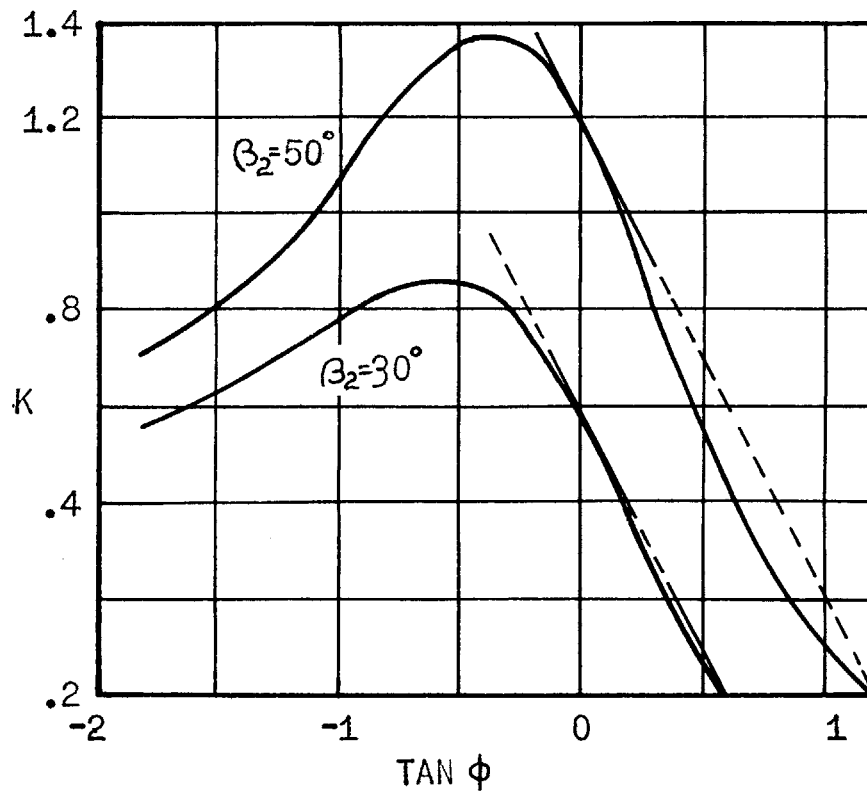
FIG. 12   K VS TAN ϕ FOR TWO VALUES OF β_2
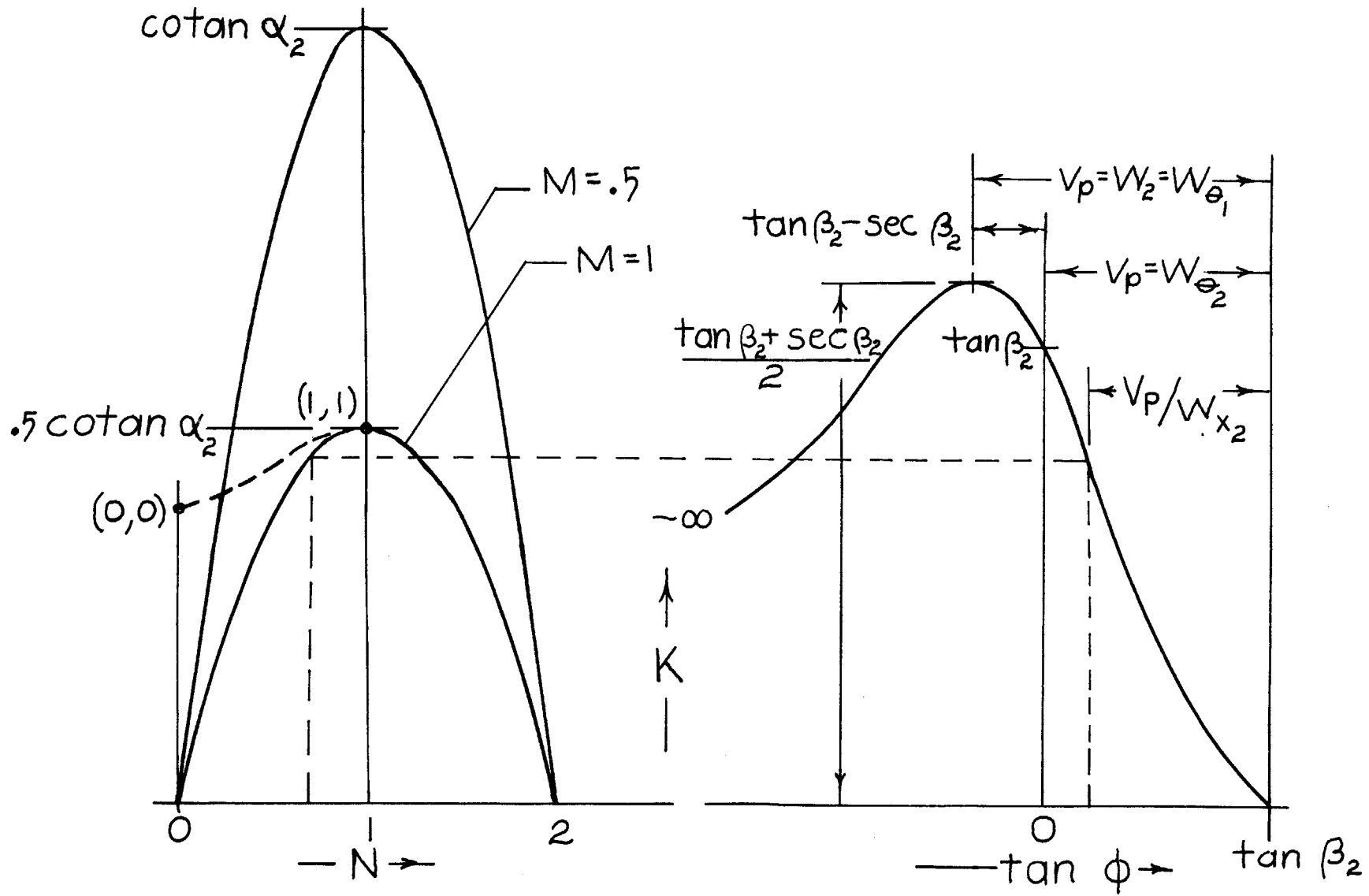
FIG. 13   K VS M AND N   K VS TAN φ
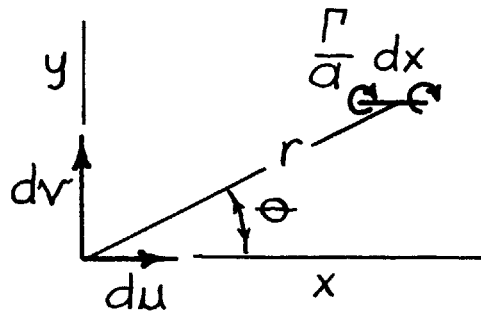
FIG. 14   VELOCITY INDUCED FROM ELEMENT
OF VORTEX SHEET
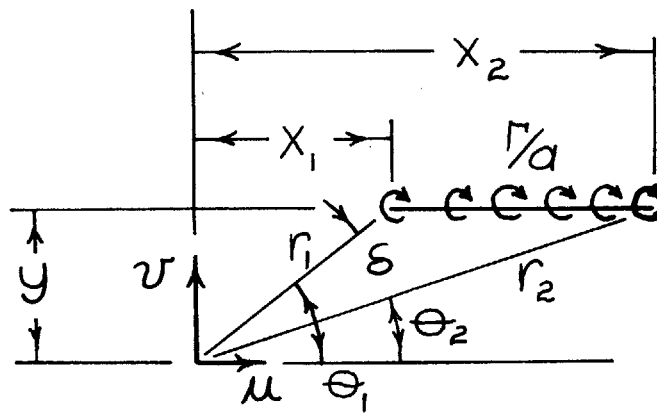
FIG. 15   VELOCITY INDUCED FROM FINITE
LENGTH VORTEX SHEET
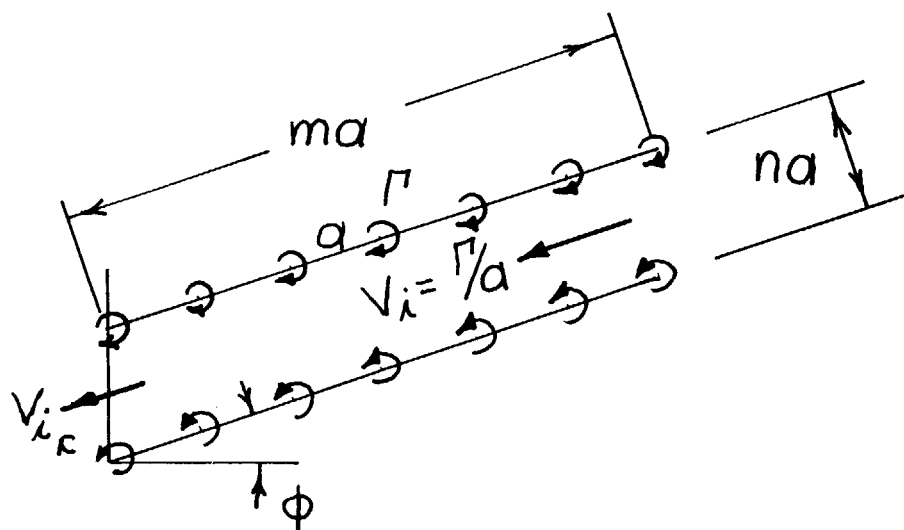
FIG. 16   VELOCITY INDUCED FROM TWO FINITE VORTEX
SHEETS AT ANGLE ϕ
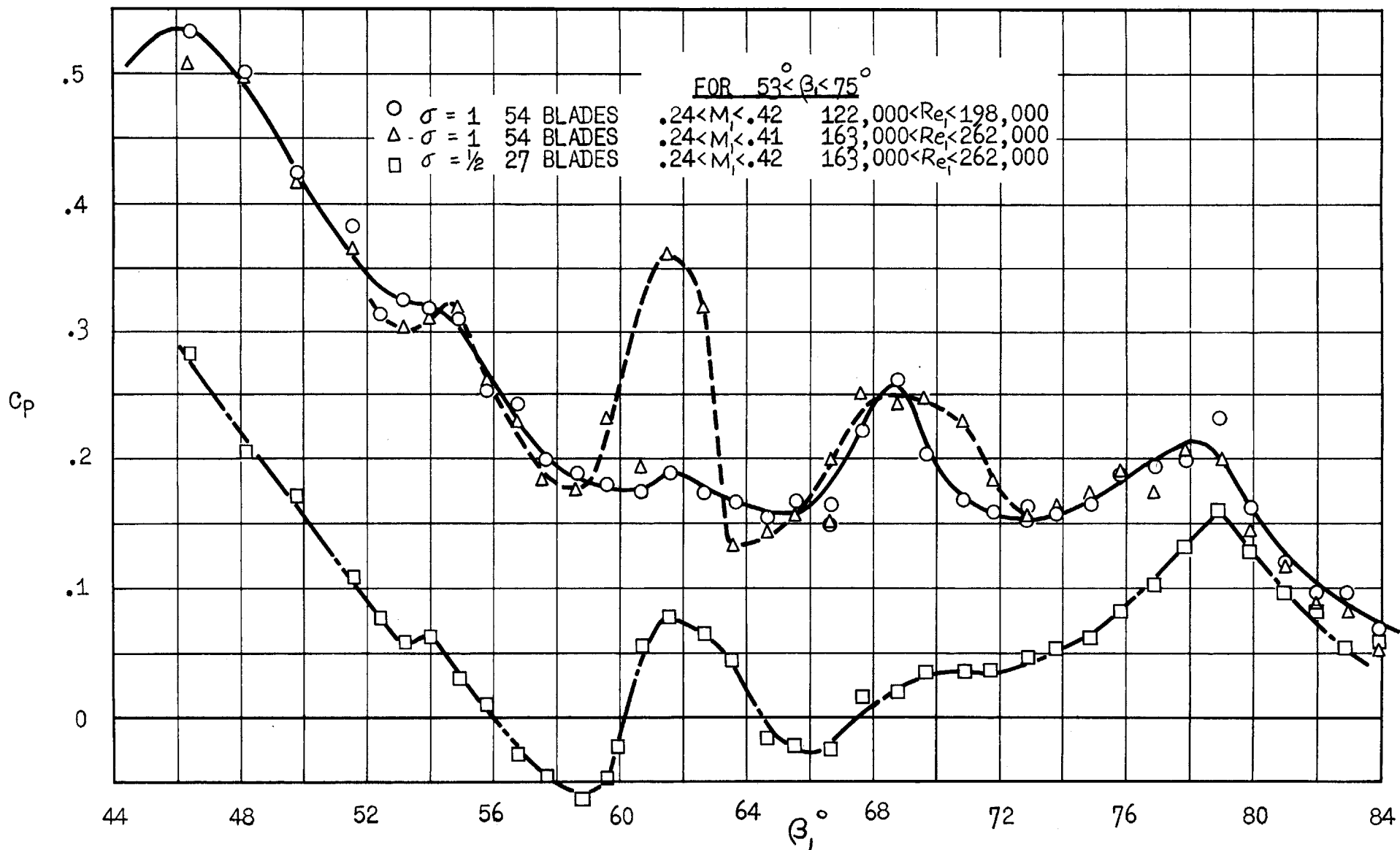
FIG. 18 PRESSURE COEFFICIENT VS UPSTREAM AIR ANGLE-CONFIGURATION A
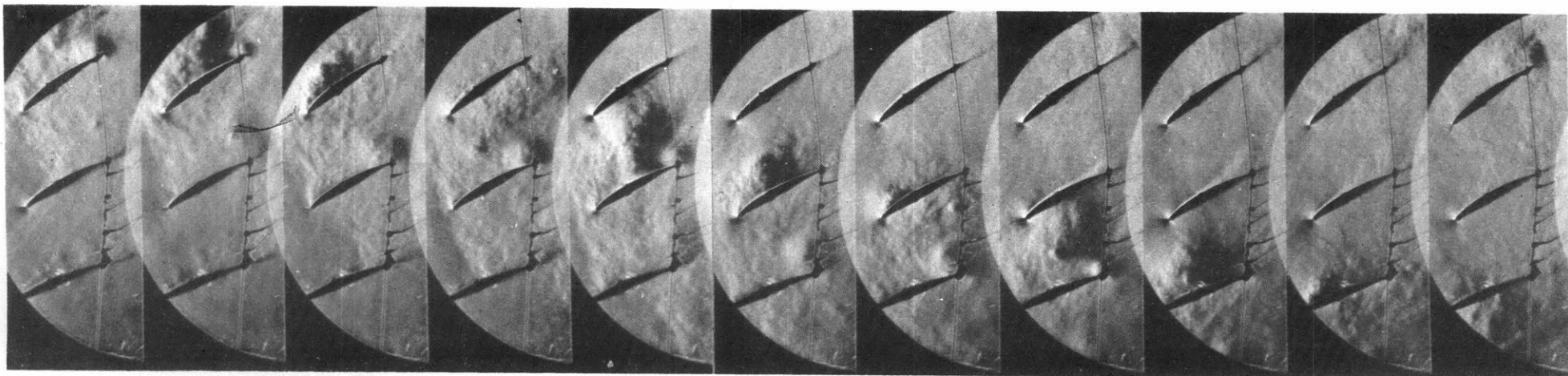
C) $\beta_1 = 68°$
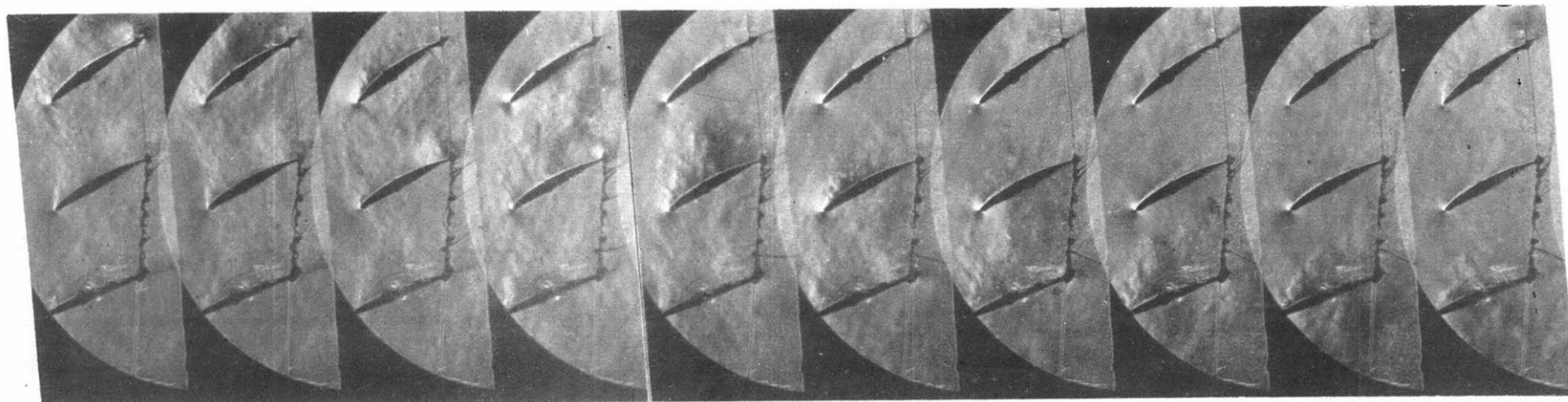
D) $\beta_1 = 81°$

FIG. 19   SCHLIEREN FILMS-CONFIGURATION A, $\sigma = 1$
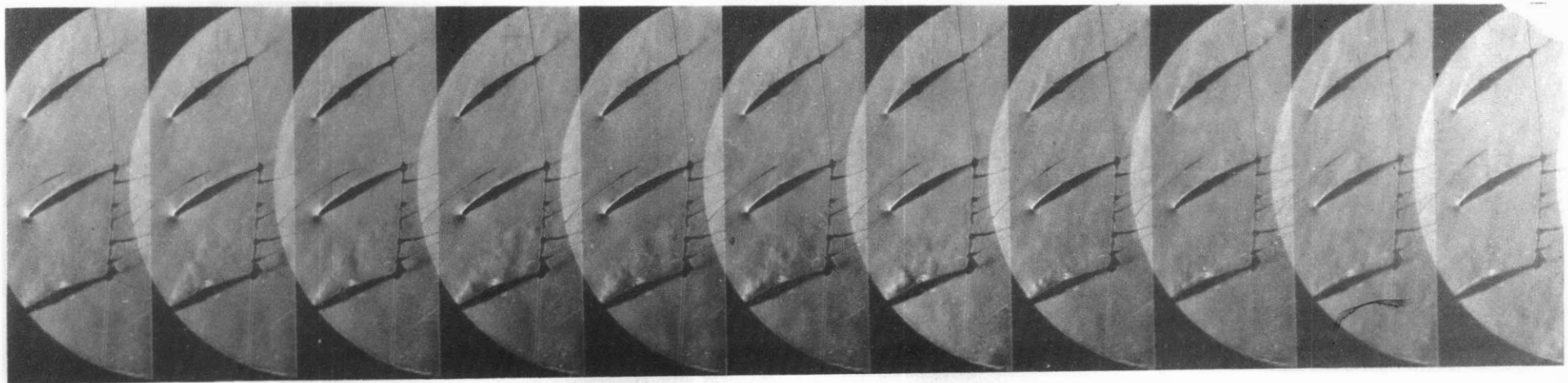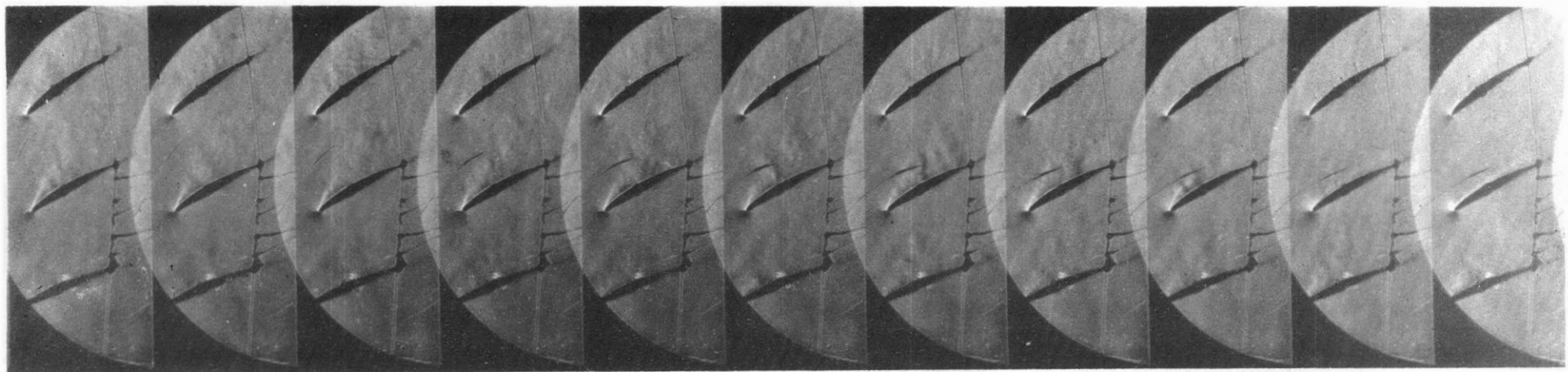
FIG. 19 A)   SCHLIEREN FILMS-CONFIGURATION A, $\sigma = 1$, $\beta_i = 55°$, TIME $\nearrow$

FIG. 19 B) SCHLIEREN FILMS-CONFIGURATION A, $\sigma = 1$, $\beta_1 = 60°$, TIME ⇄
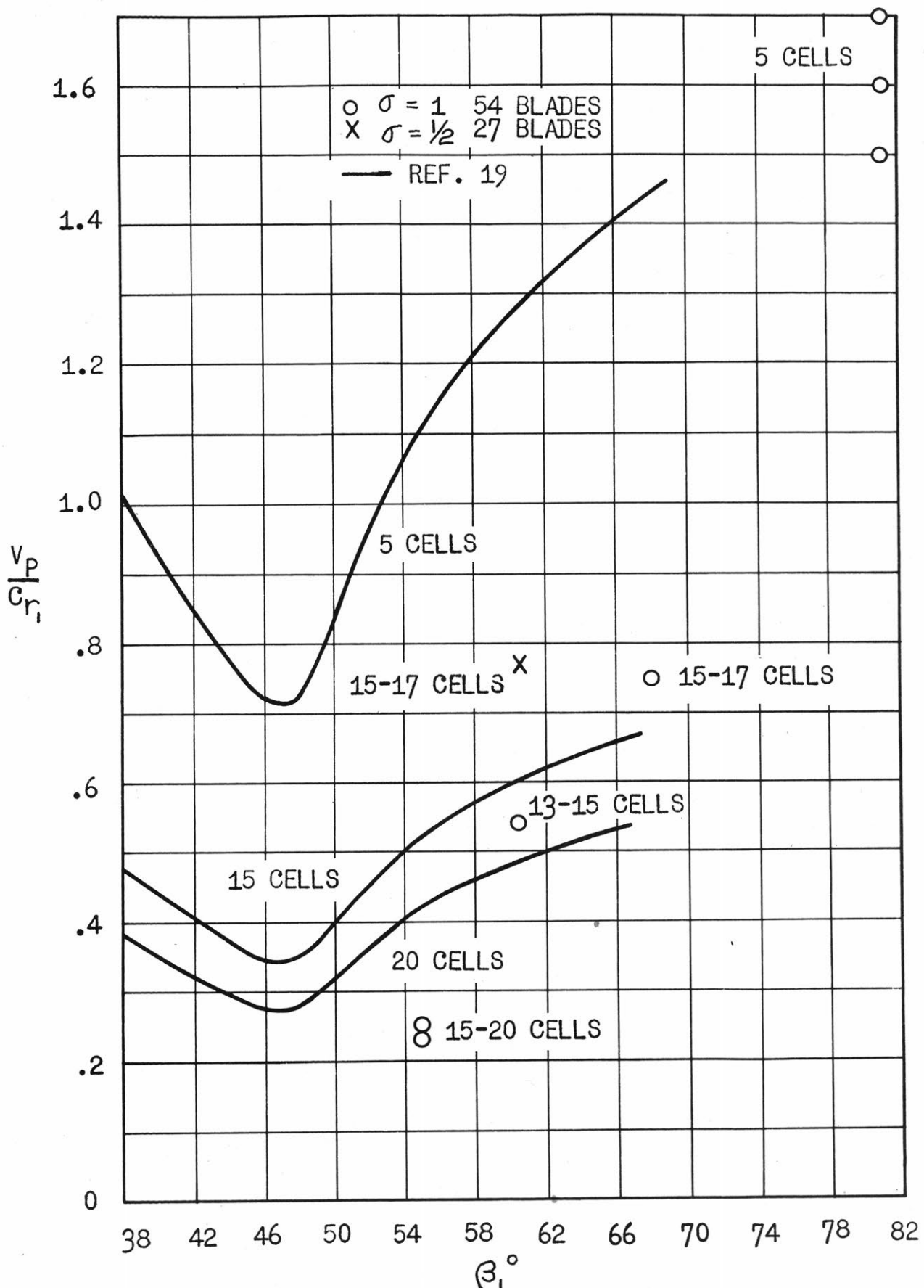
FIG. 20 VELOCITY OF STALL PROPAGATION VS UPSTREAM AIR ANGLE
CONFIGURATION A

	β_1°	σ	CONFIGURATION	TIMING FREQUENCY CPS
A	55	1	A	200
B	63	1	A	200
C	69	1	A	1000
D	81	1	A	400
E	61	1/2	A	500
F	57	1/3	B	500
G	70	1/3	B	500
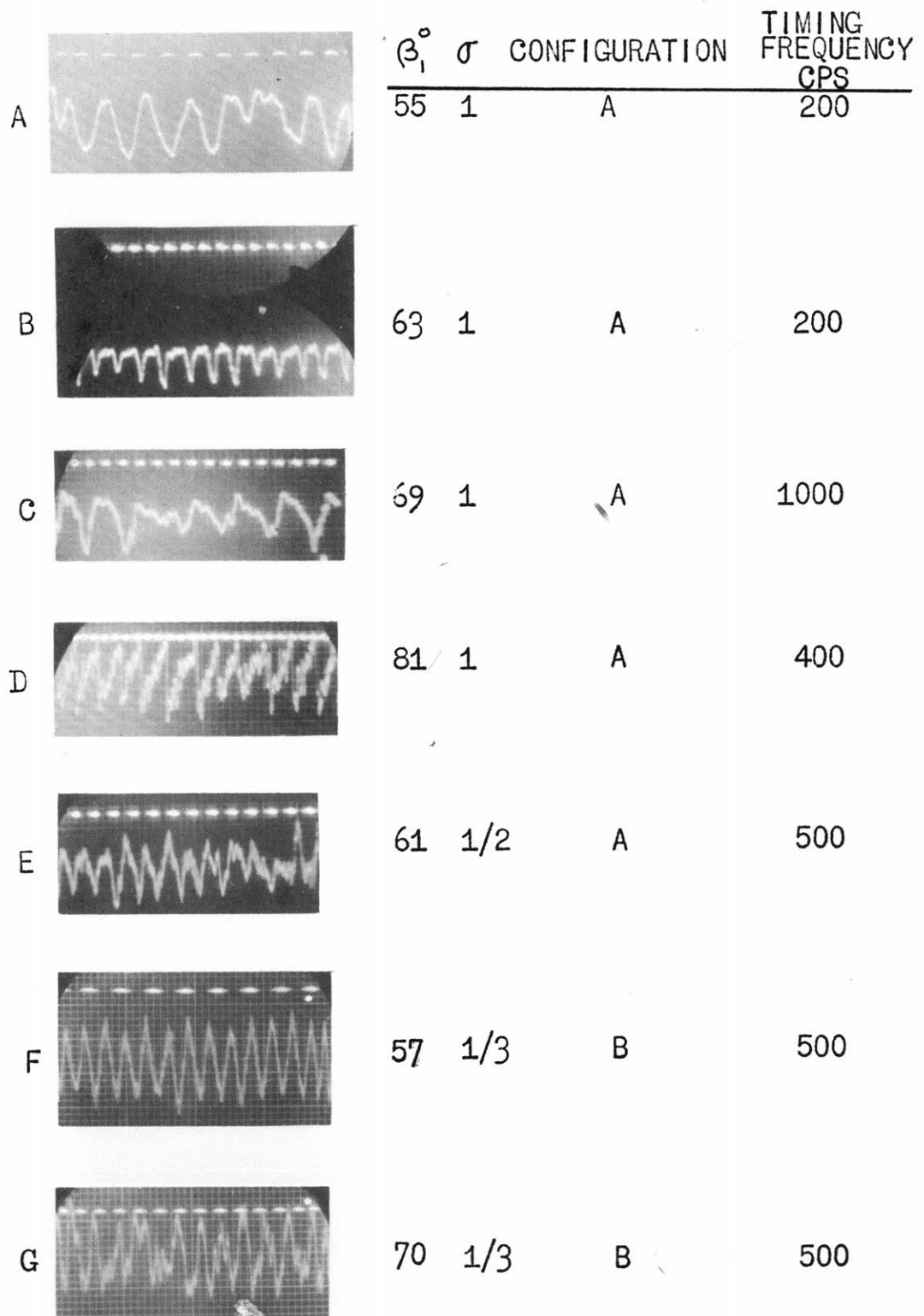
FIG. 21   HOT WIRE TRACES UPSTREAM OF CIRCULAR CASCADE
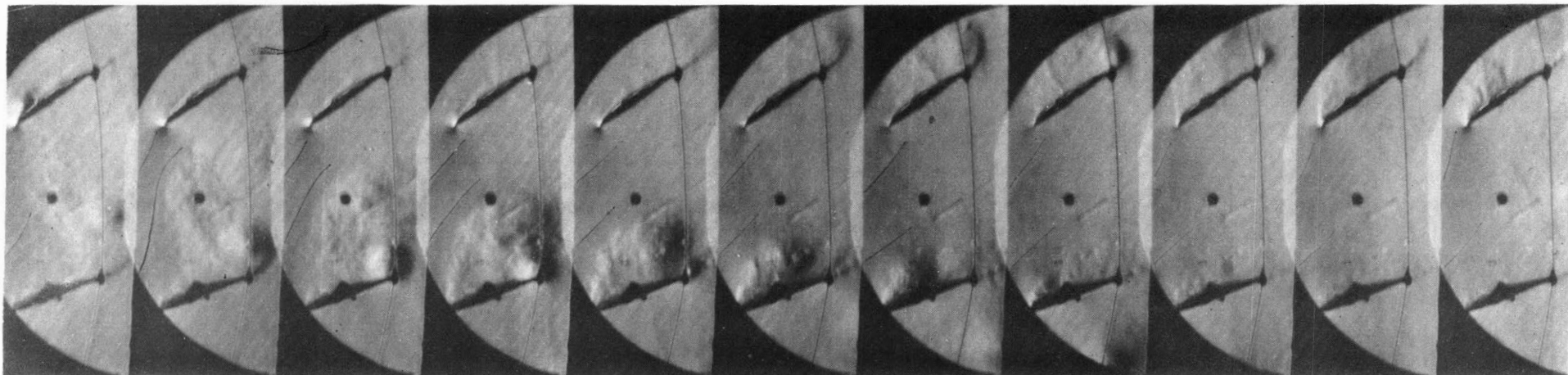
A)

B)
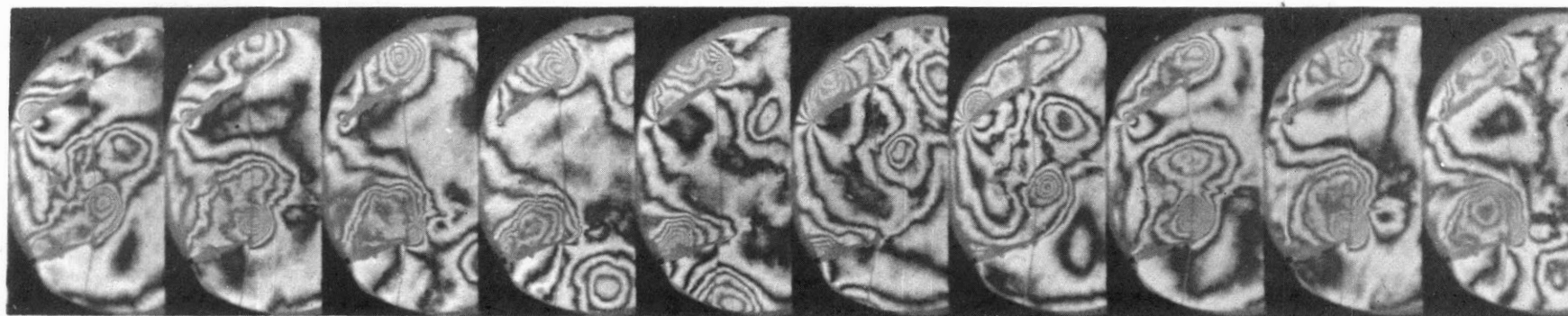
FIG. 22   SCHLIEREN AND INTERFEROMETER FILMS-CONFIGURATION A, $\sigma = 1/2$, $\beta_1 = 60°$
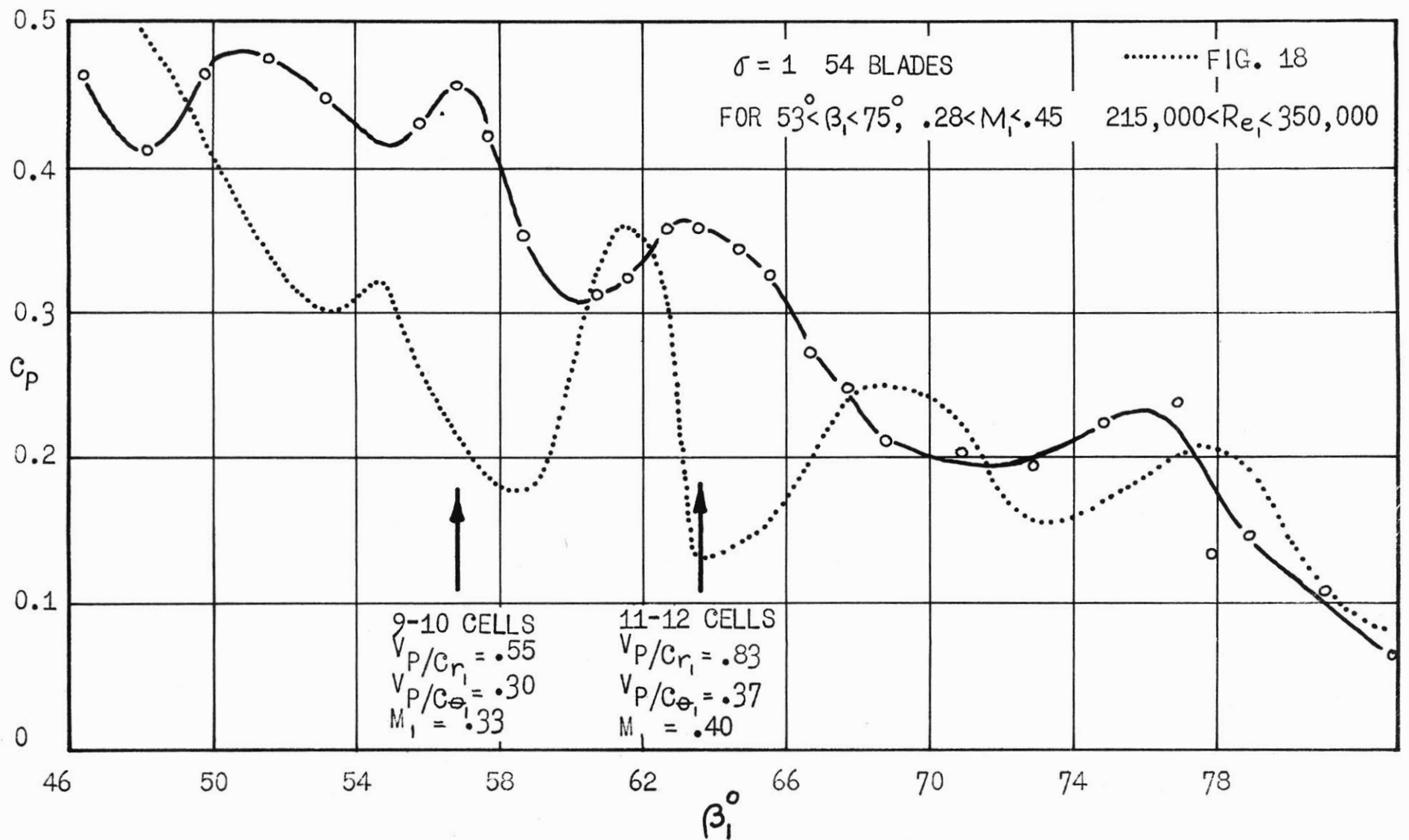
FIG. 23 PRESSURE COEFFICIENT VS UPSTREAM AIR ANGLE-CONFIGURATION B
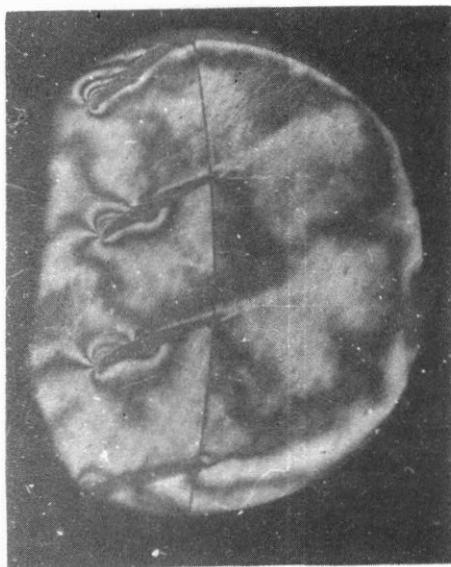
$\beta_1 = 46.4$
$M_1 = 0.45$

$\beta_1 = 51.6$
$M_1 = 0.50$
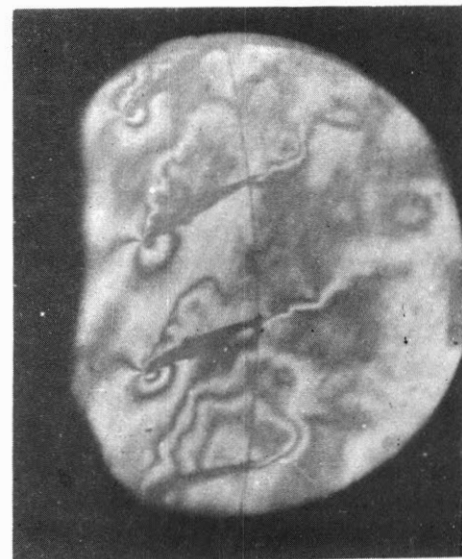
$\beta_1 = 60.7$
$M_1 = 0.38$

FIG. 24   INTERFEROGRAMS OF STEADY FLOW-CONFIGURATION B, $\sigma = 1$
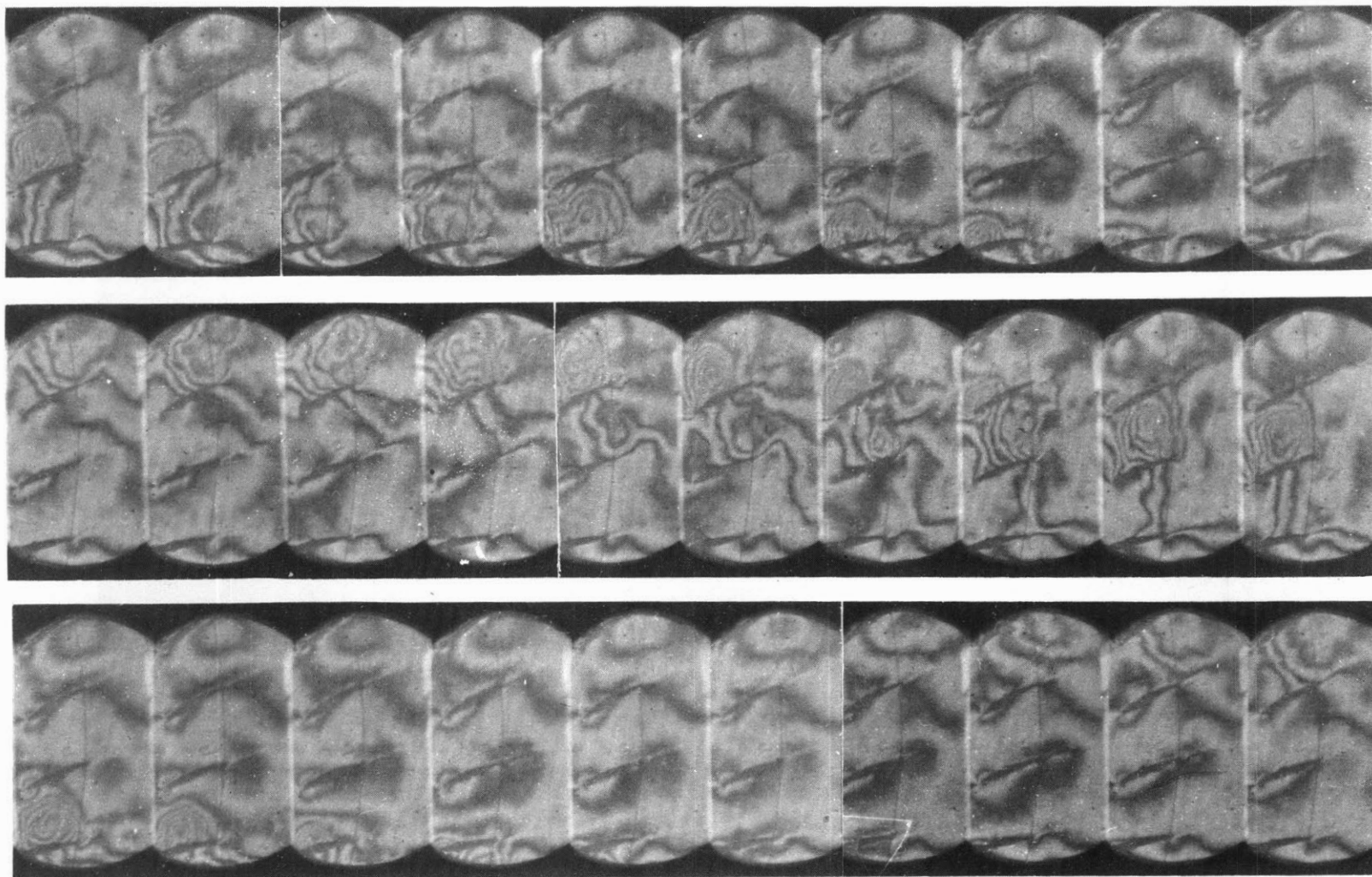
FIG. 25 A) INTERFEROMETER FILMS-CONFIGURATION B, $\sigma = 1$, $\beta_i = 57°$, TIME ⋛
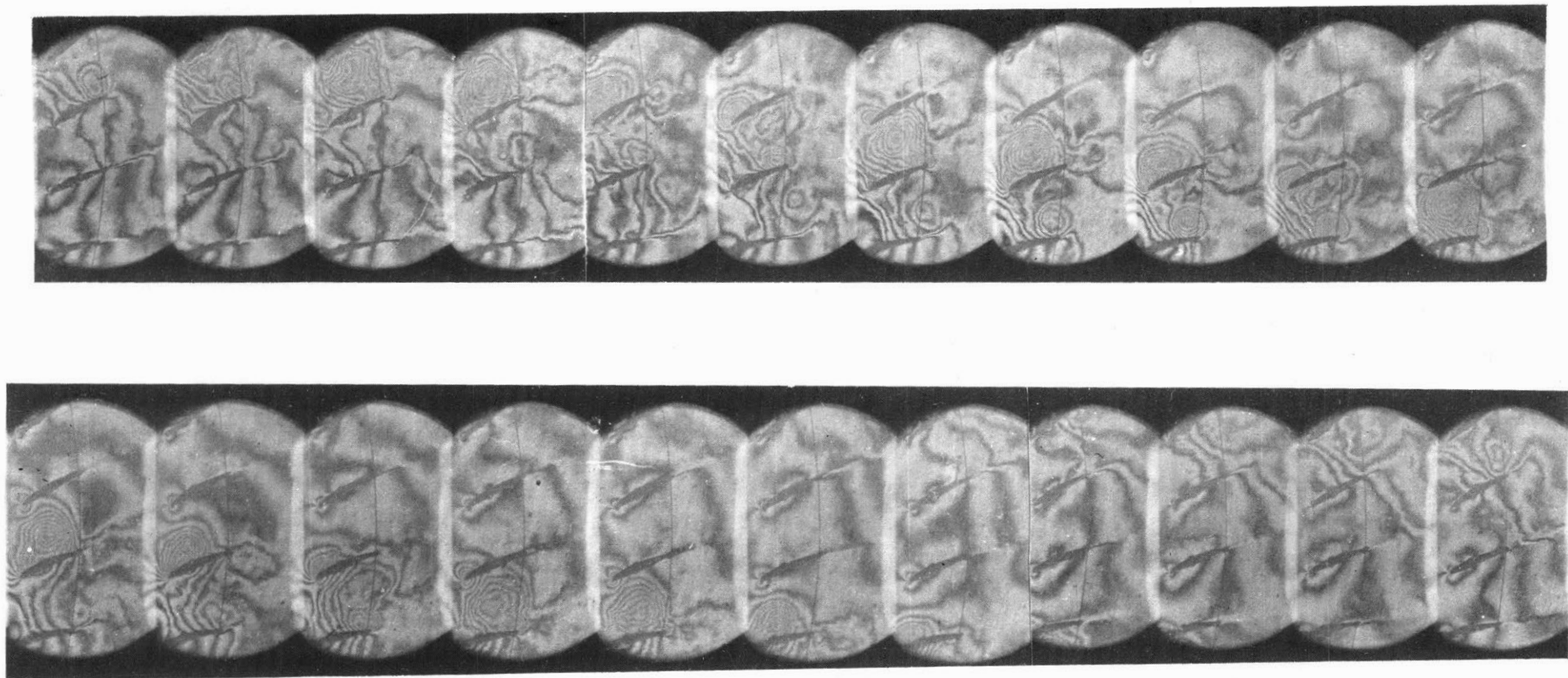
FIG. 25 B) INTERFEROMETER FILMS-CONFIGURATION B, $\sigma = 1, \beta_1 = 64°,$ TIME
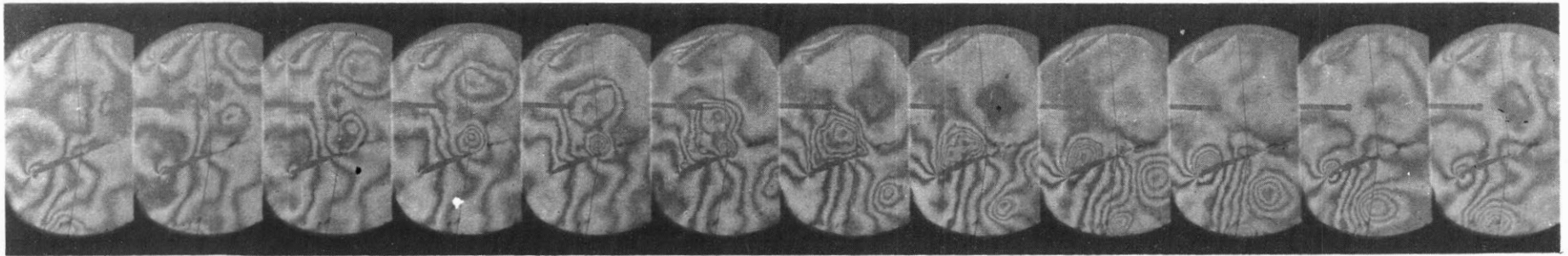
A) $\beta_1 = 58°$
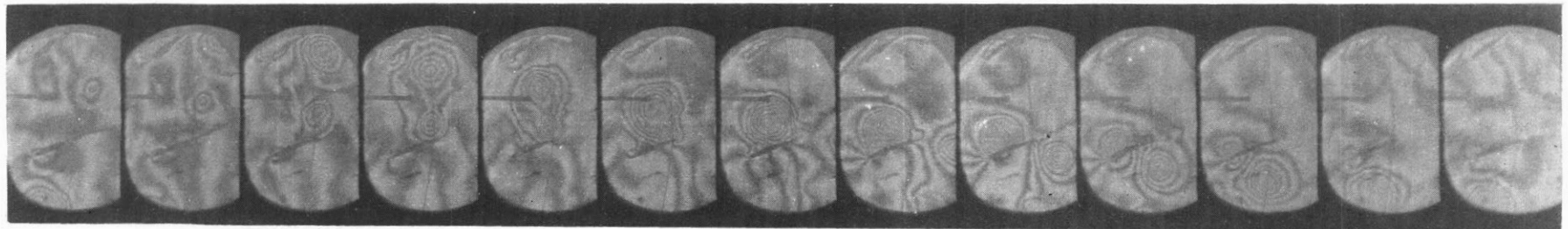
C) $\beta_1 = 64°$

FIG. 26   INTERFEROMETER FILMS-CONFIGURATION B, $\sigma = 1/2$
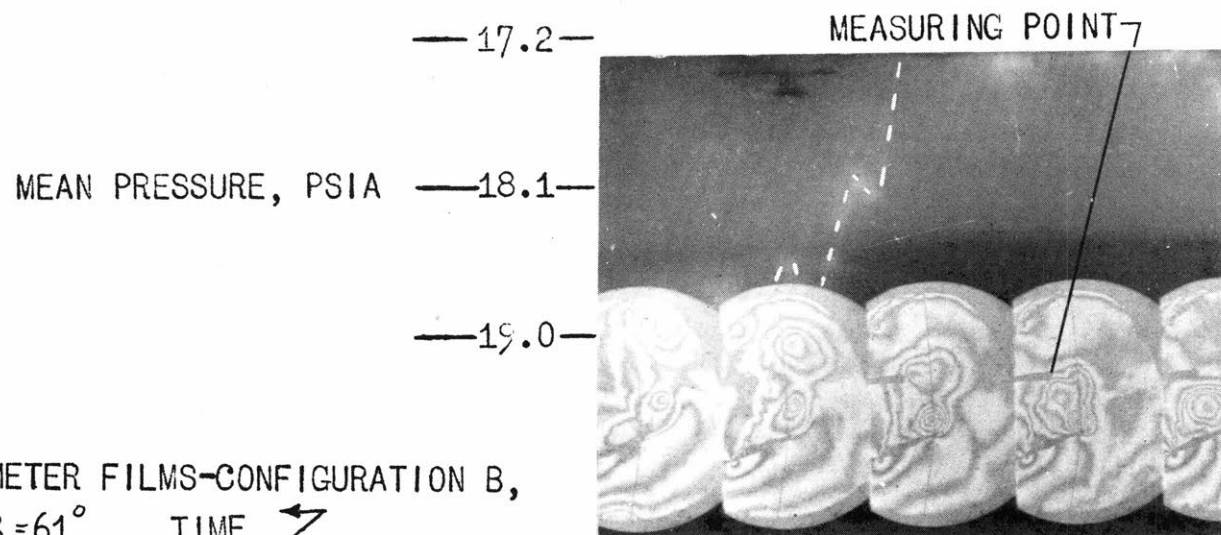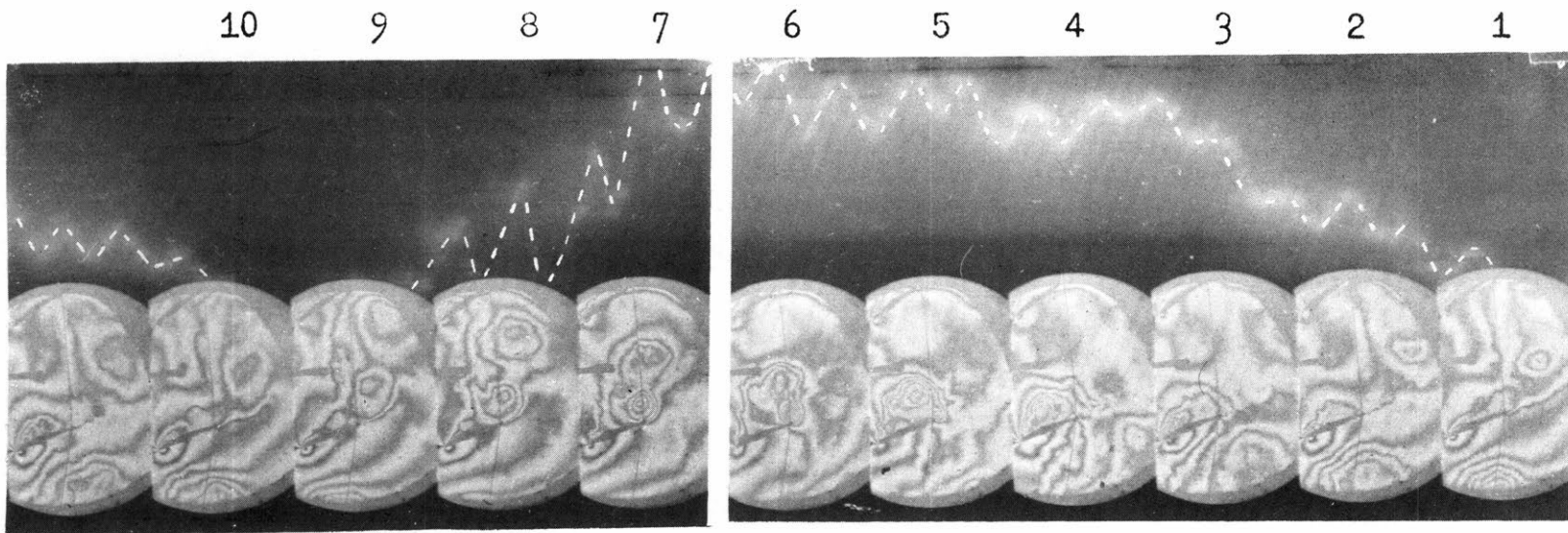
FIG. 26 B) INTERFEROMETER FILMS—CONFIGURATION B, $\sigma = 1/2$, $\beta_1 = 61°$ TIME Z

A) $\beta_1 = 57°$
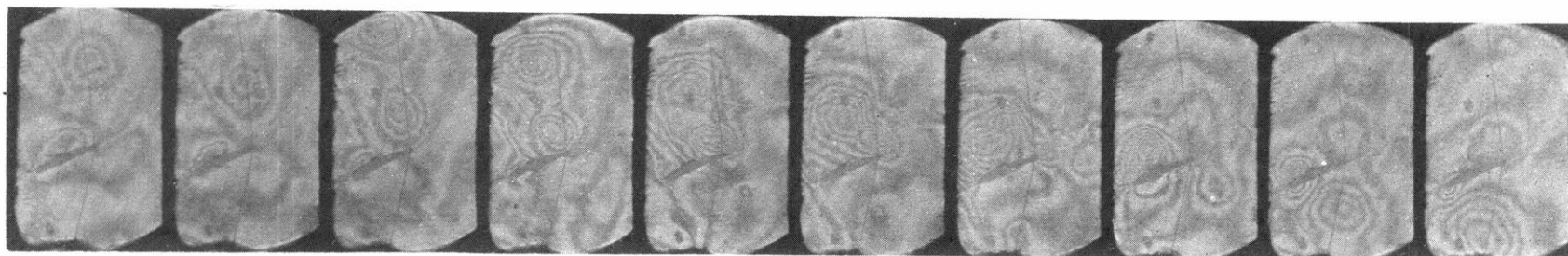
B) $\beta_1 = 70°$

FIG. 27   INTERFEROMETER FILMS-CONFIGURATION B, $\sigma = 1/3$
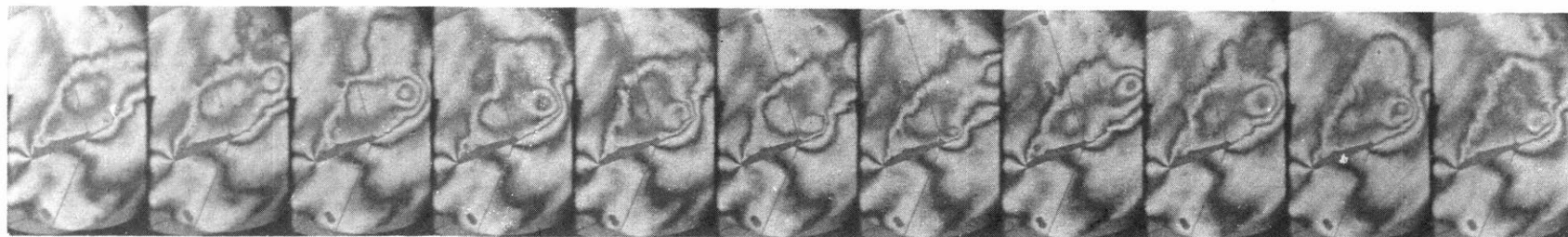
FIG. 28   INTERFEROMETER FILMS-CONFIGURATION B, $\sigma = 1/6$, $\beta_1 = 57°$

$$\frac{f \cdot L \cdot SIN\, i}{W_1}$$

$i = 20°$
28°
60°
38°
26°
30°
33°
27°
33°
26°
27°

.15

.10

.05

0

0   1/6 1/3 1/2 $\sigma \rightarrow$ 1
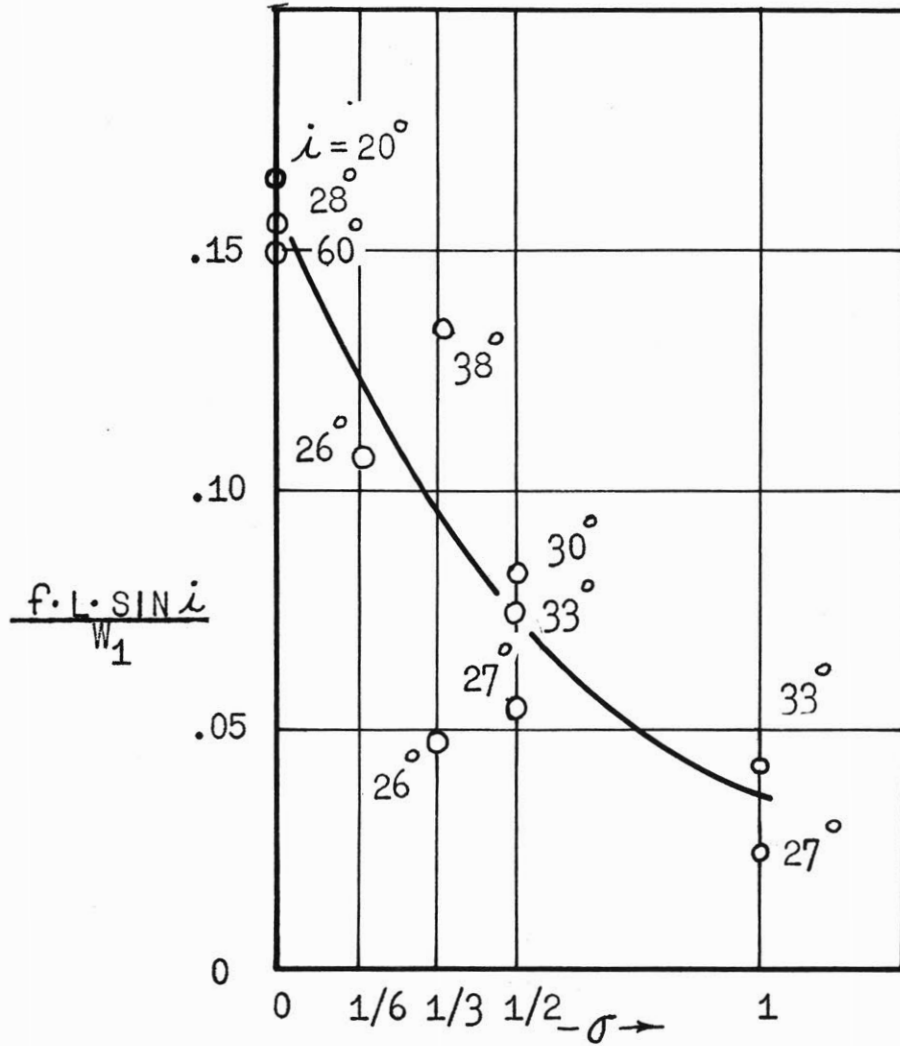
FIG. 29
VORTEX SHEDDING FREQUENCY VS SOLIDITY
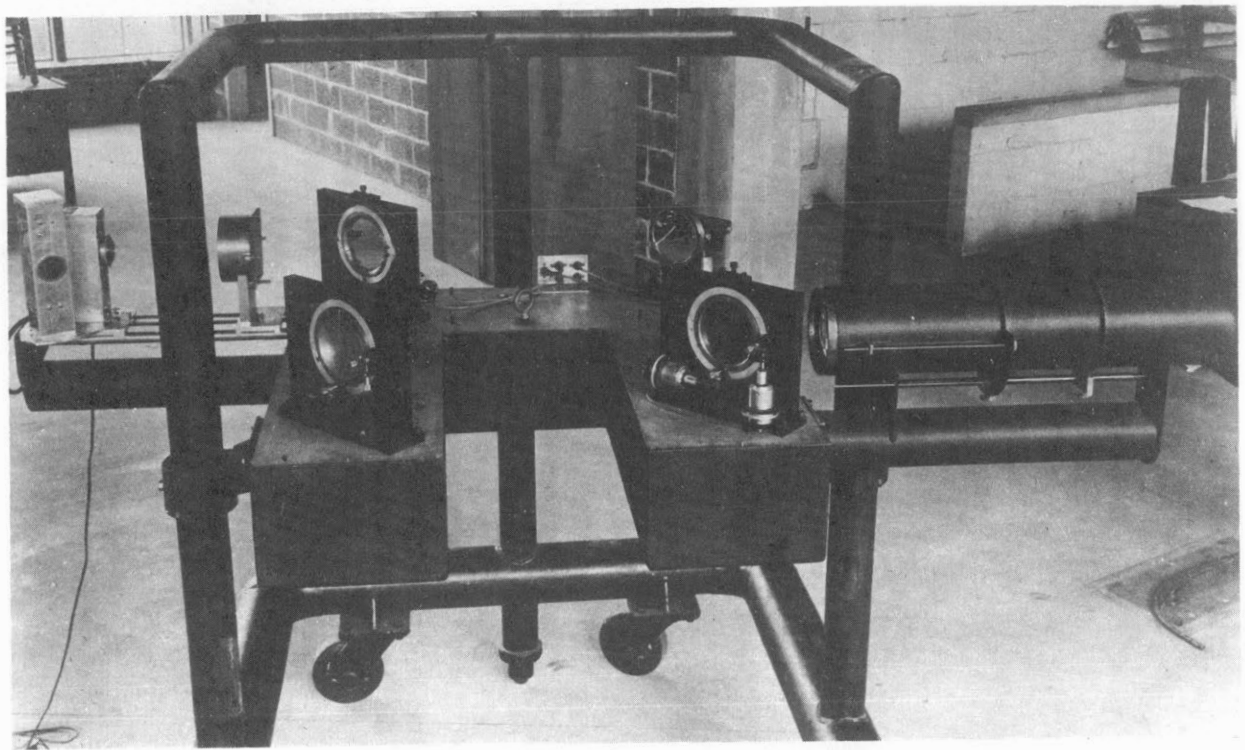
FIG. 30   PHOTOGRAPH OF GAS TURBINE LABORATORY INTERFEROMETER
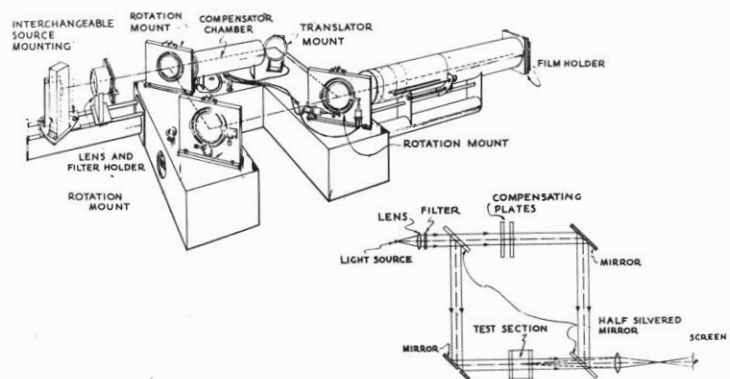
FIG. 31   SCHEMATIC DIAGRAM OF INTERFEROMETER
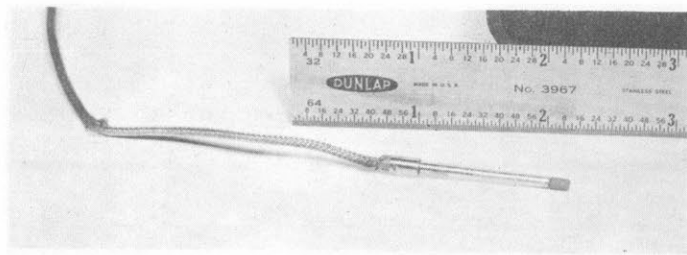
FIG. 32   PHOTOGRAPH OF PIEZOELECTRIC CRYSTAL PRESSURE PICK-UP
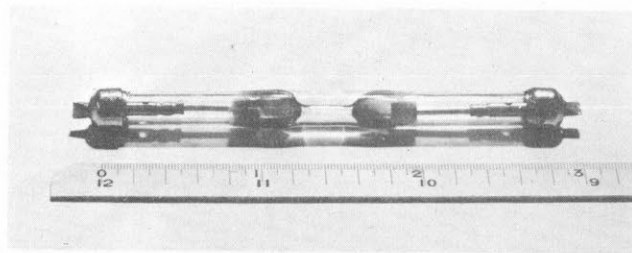
FIG. 33   PHOTOGRAPH OF LIGHT SOURCE
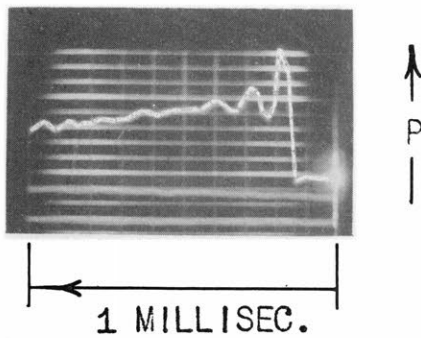
FIG. 34   RESPONSE OF
CRYSTAL PICKUP TO SHOCK WAVE
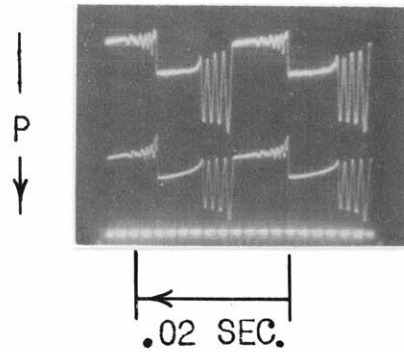
FIG. 35   RESPONSE OF
PICKUPS IN PRESSURE CHAMBER

FIG. 36   PRESSURE DISTRIBUTIONS CALCULATED FROM FIG. 26 B

FRAME 5

PER CENT CHORD

FRAME 6

PER CENT CHORD

FRAME 7

PER CENT CHORD

FRAME 8

PER CENT CHORD
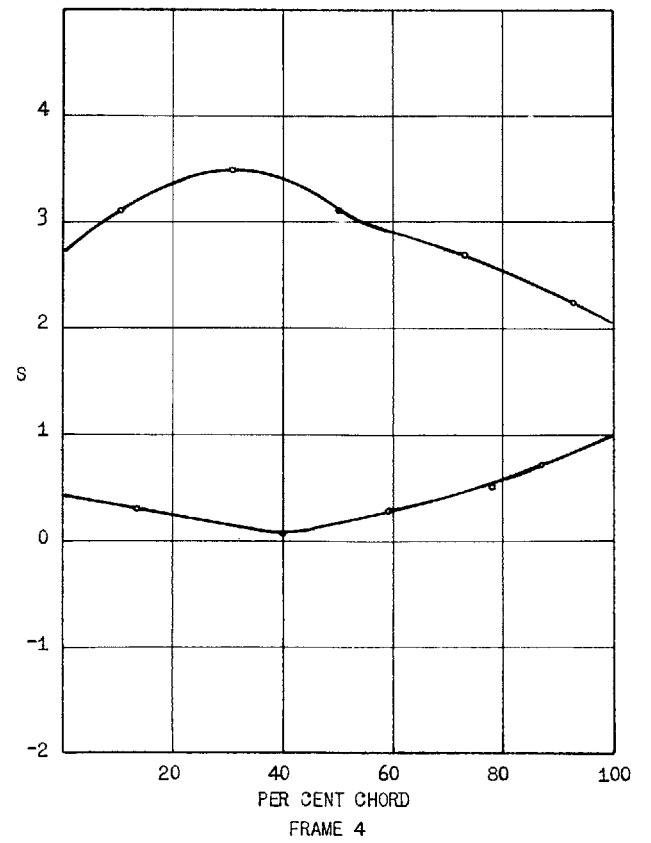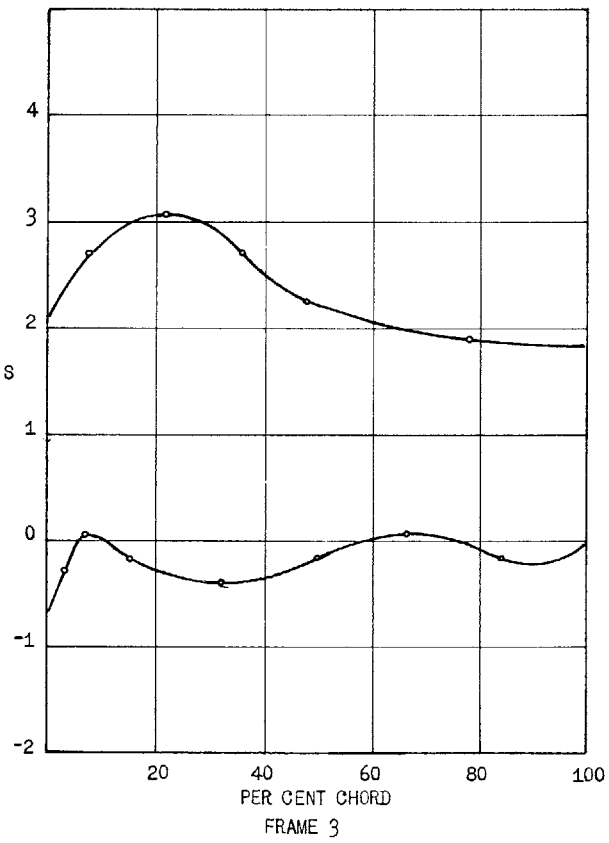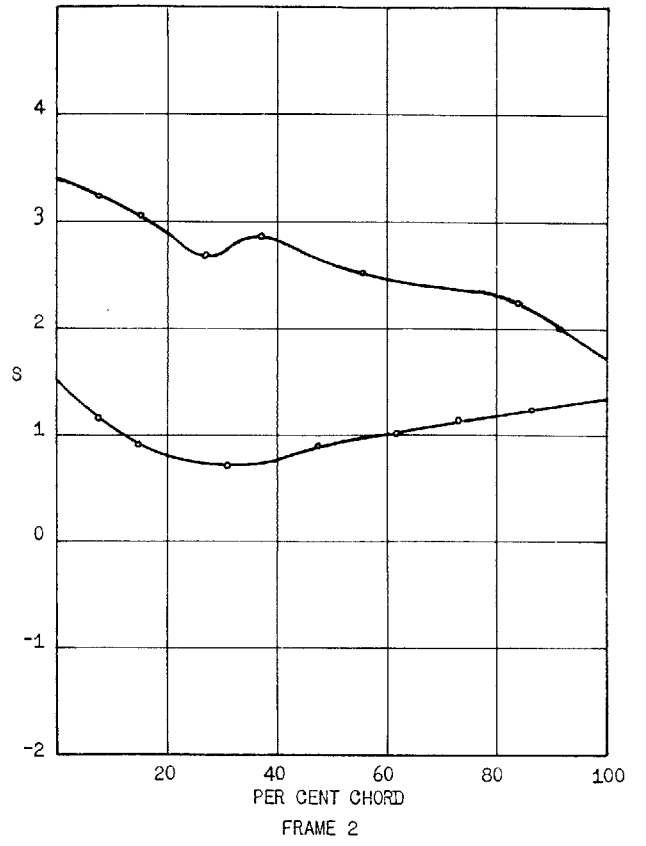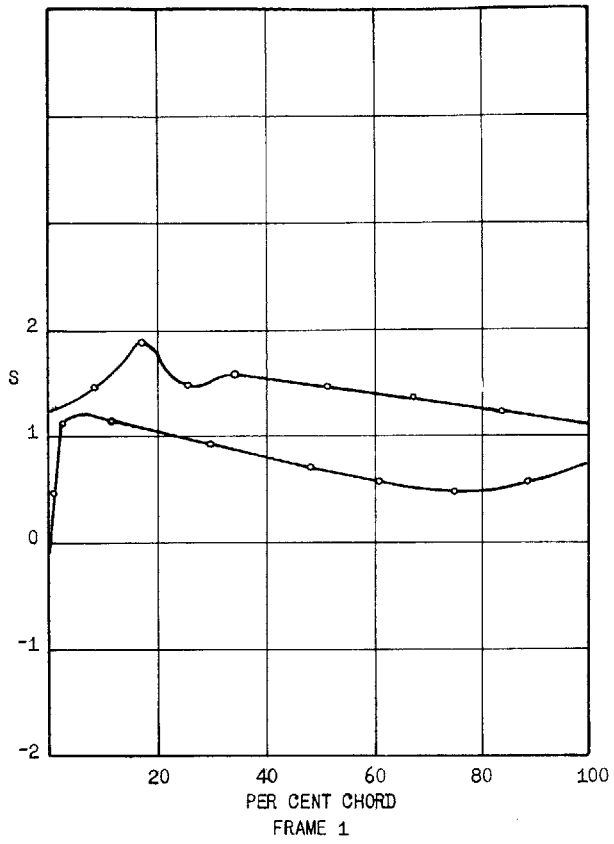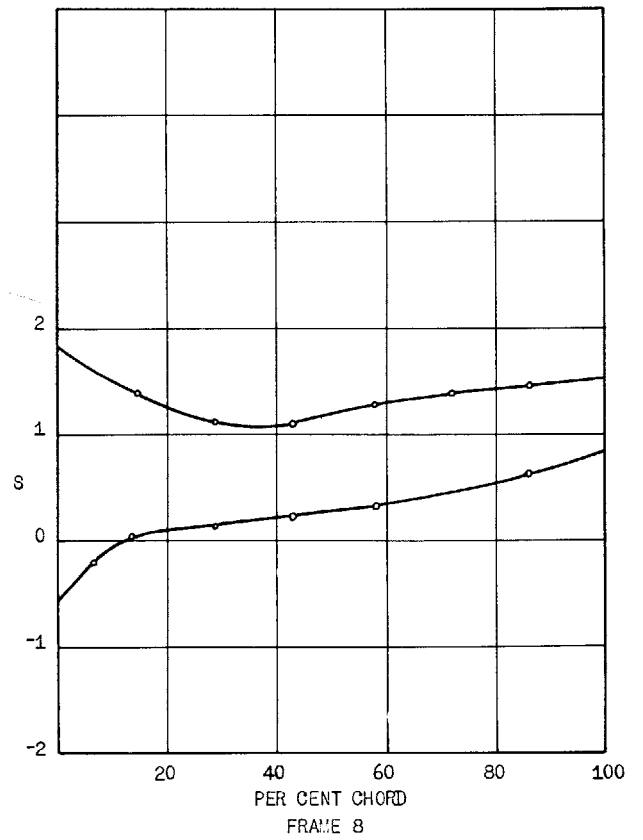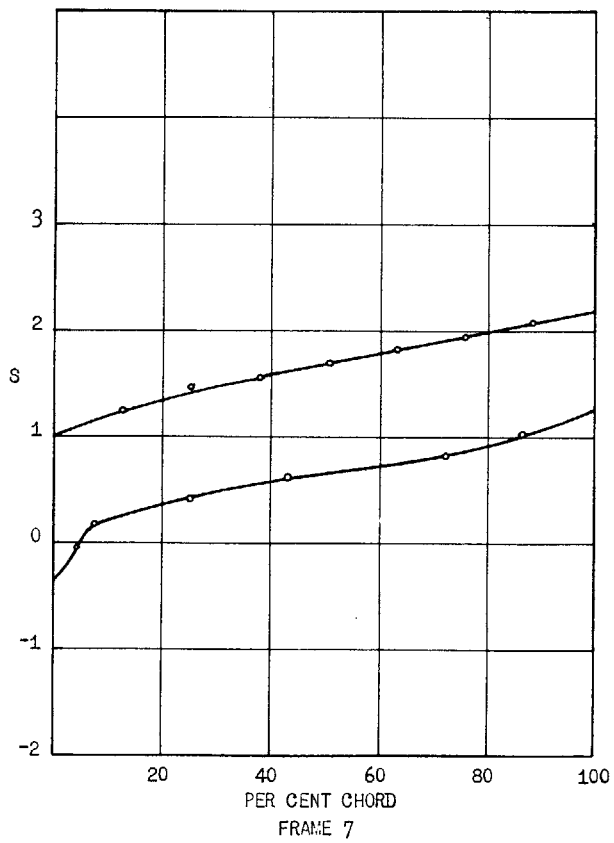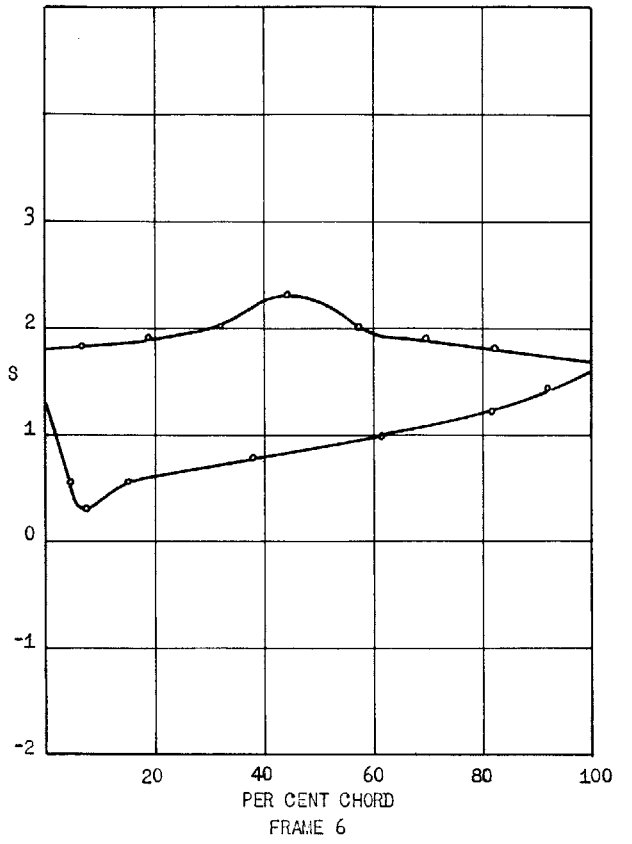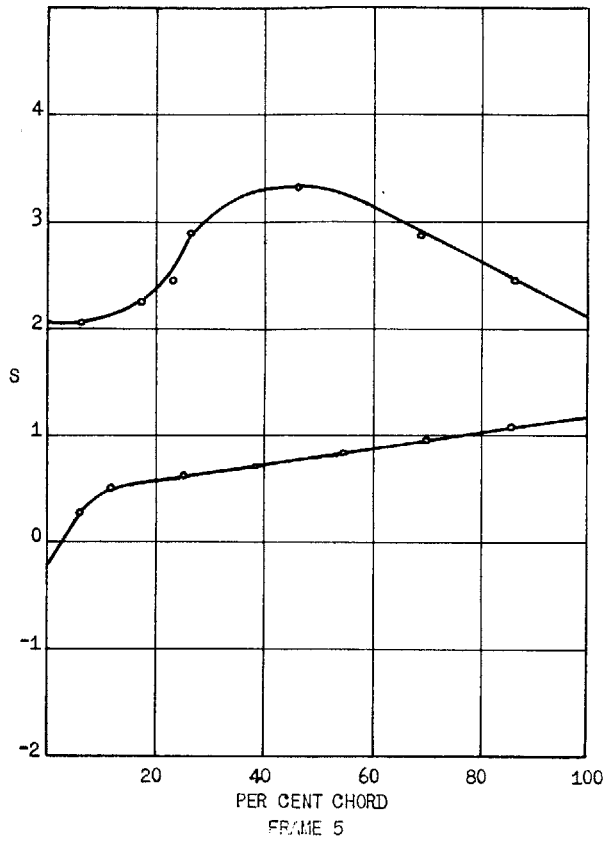
FIG. 36   PRESSURE DISTRIBUTIONS CALCULATED FROM FIG. 26B
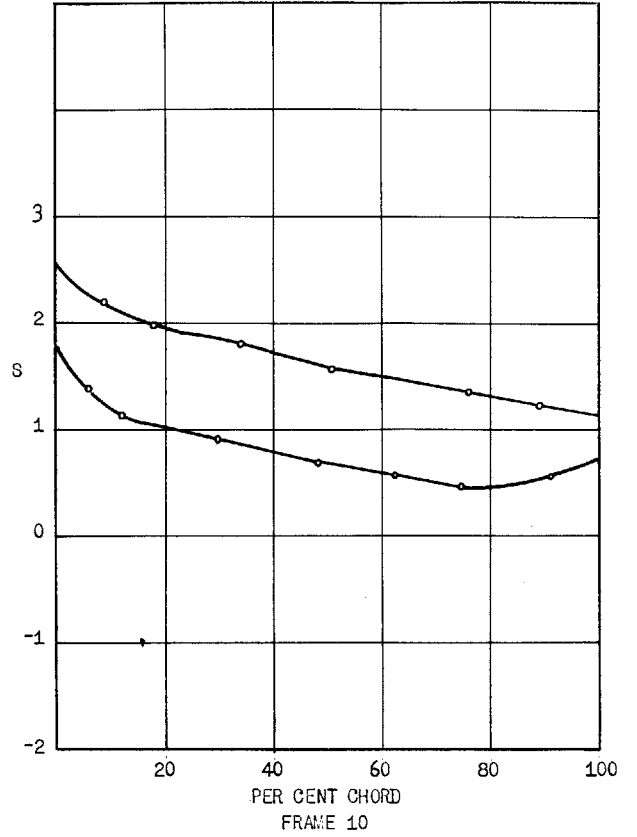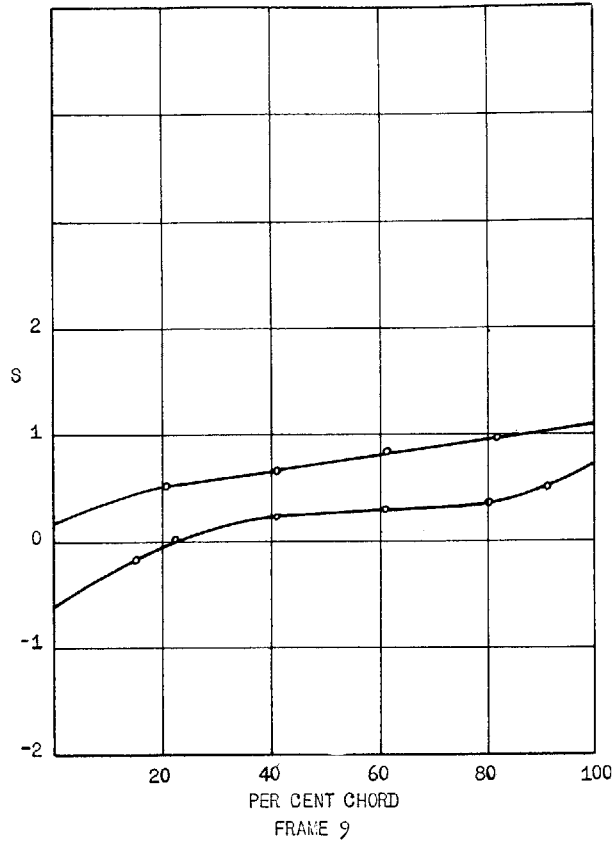
FIG. 36   PRESSURE DISTRIBUTIONS CALCULATED FROM FIG. 26 B
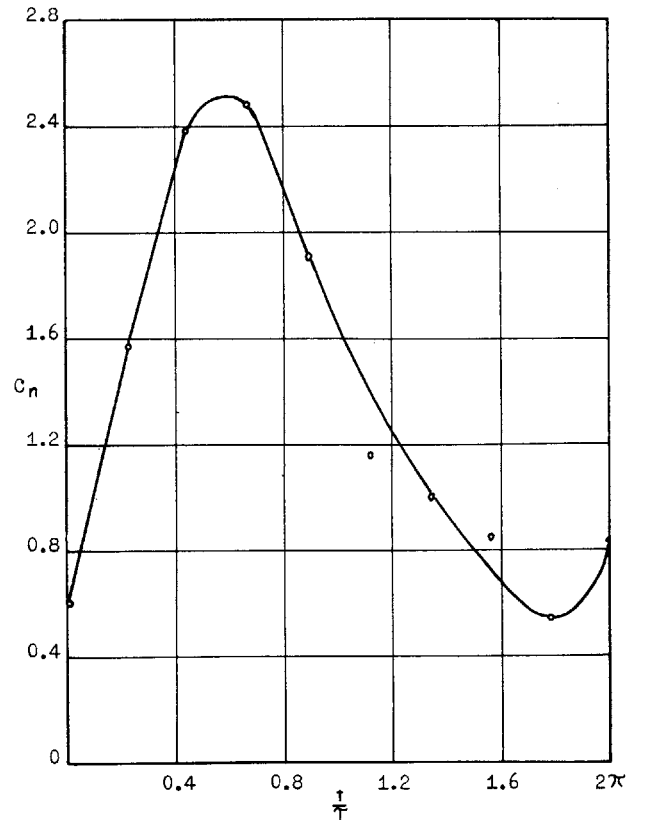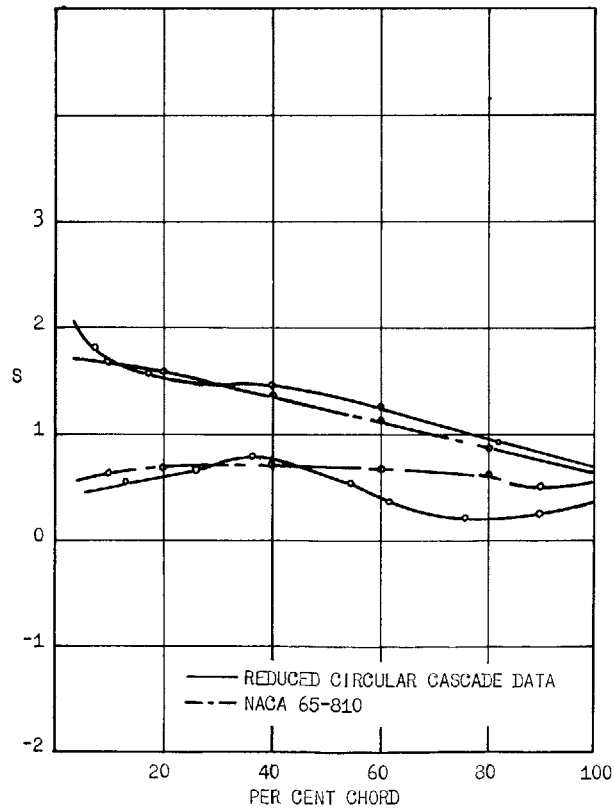
FIG. 37   COMPARISON OF PRESSURE DISTRIBUTIONS   46.4

FIG. 38   NORMAL FORCE COEFFICIENT VS TIME
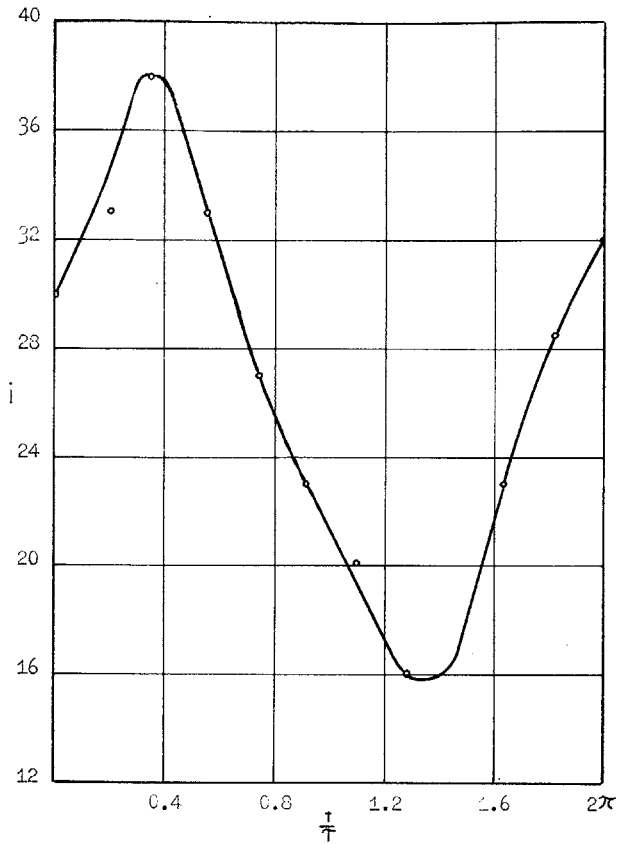
FIG. 39   LOCAL INCIDENCE VS TIME
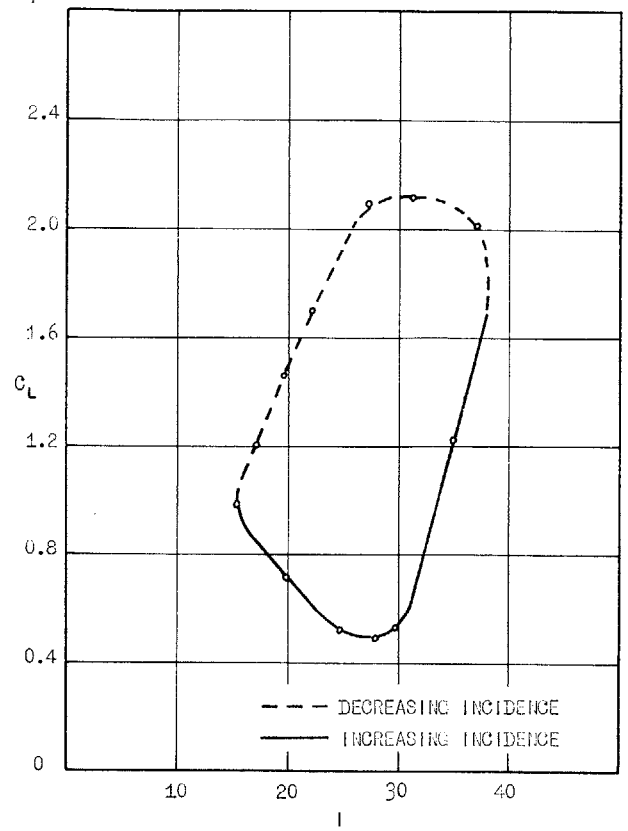
FIG. 40   LIFT COEFFICIENT VS LOCAL INCIDENCE
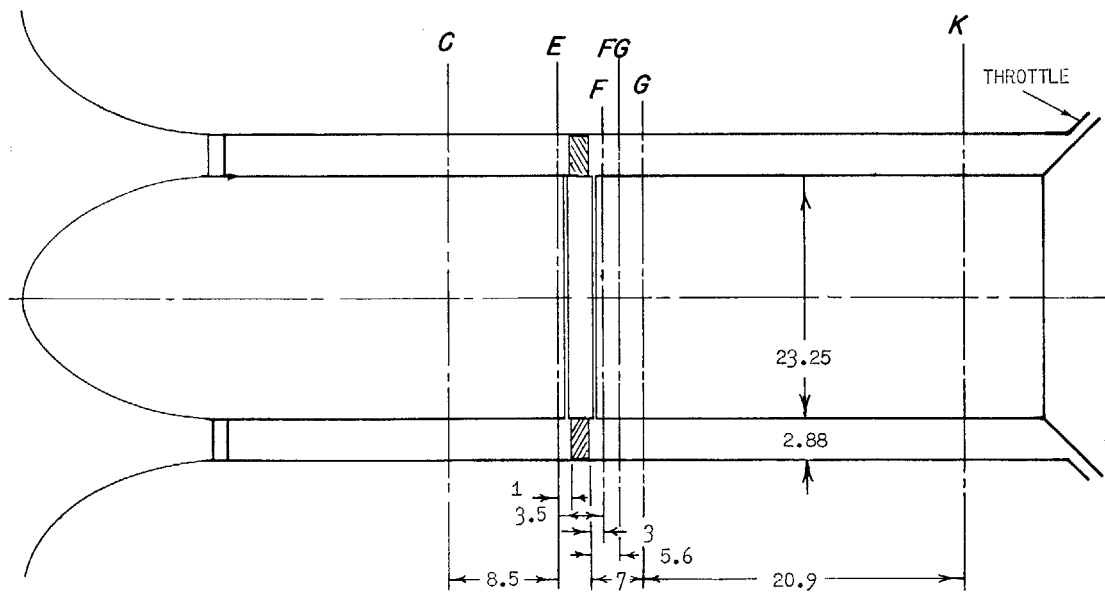
FIG. 41   SCHEMATIC DRAWING OF RESEARCH COMPRESSOR
SHOWING MEASURING STATIONS
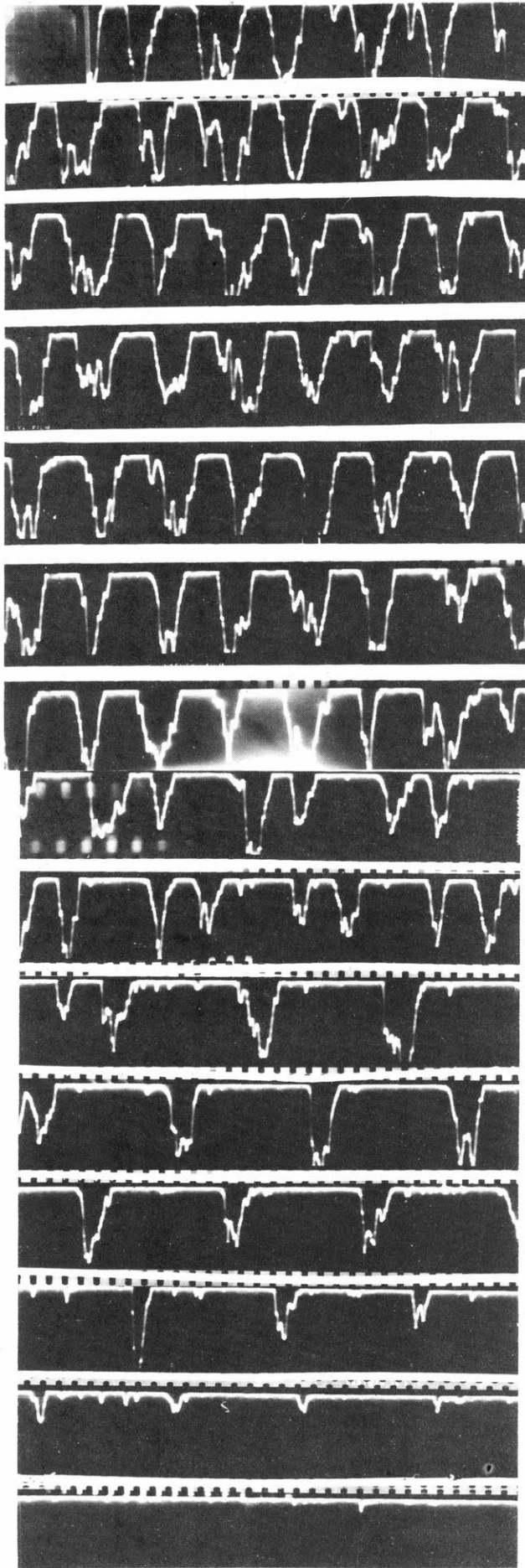
FIG. 42 STRIP FILM RECORD OF HOT WIRE TRACE
SHOWING C_{X_G} AS THROTTLE IS OPENED
CONFIGURATION C   TIME $\searrow$ $+ C \uparrow$

CONFIGURATION A

$30° 15'$

CONFIGURATION B

$30° 15'$

CONFIGURATION C

$52° 45'$
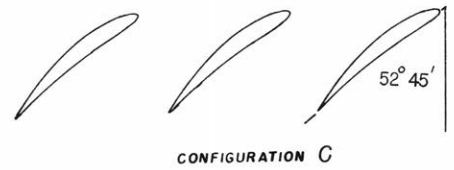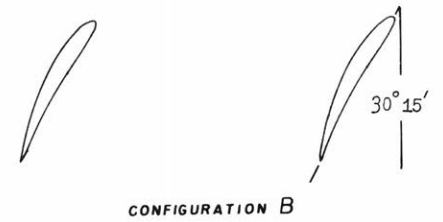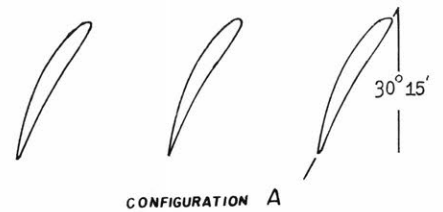
FIG. 43   ROTOR CONFIGURATIONS

HOT WIRE PROBE

A—A

$60°$

B—B
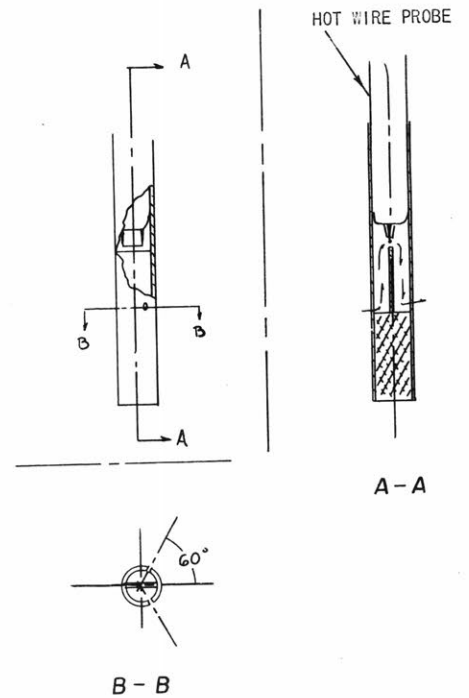
FIG. 44   HOT WIRE ANGLE MEASURING PROBE
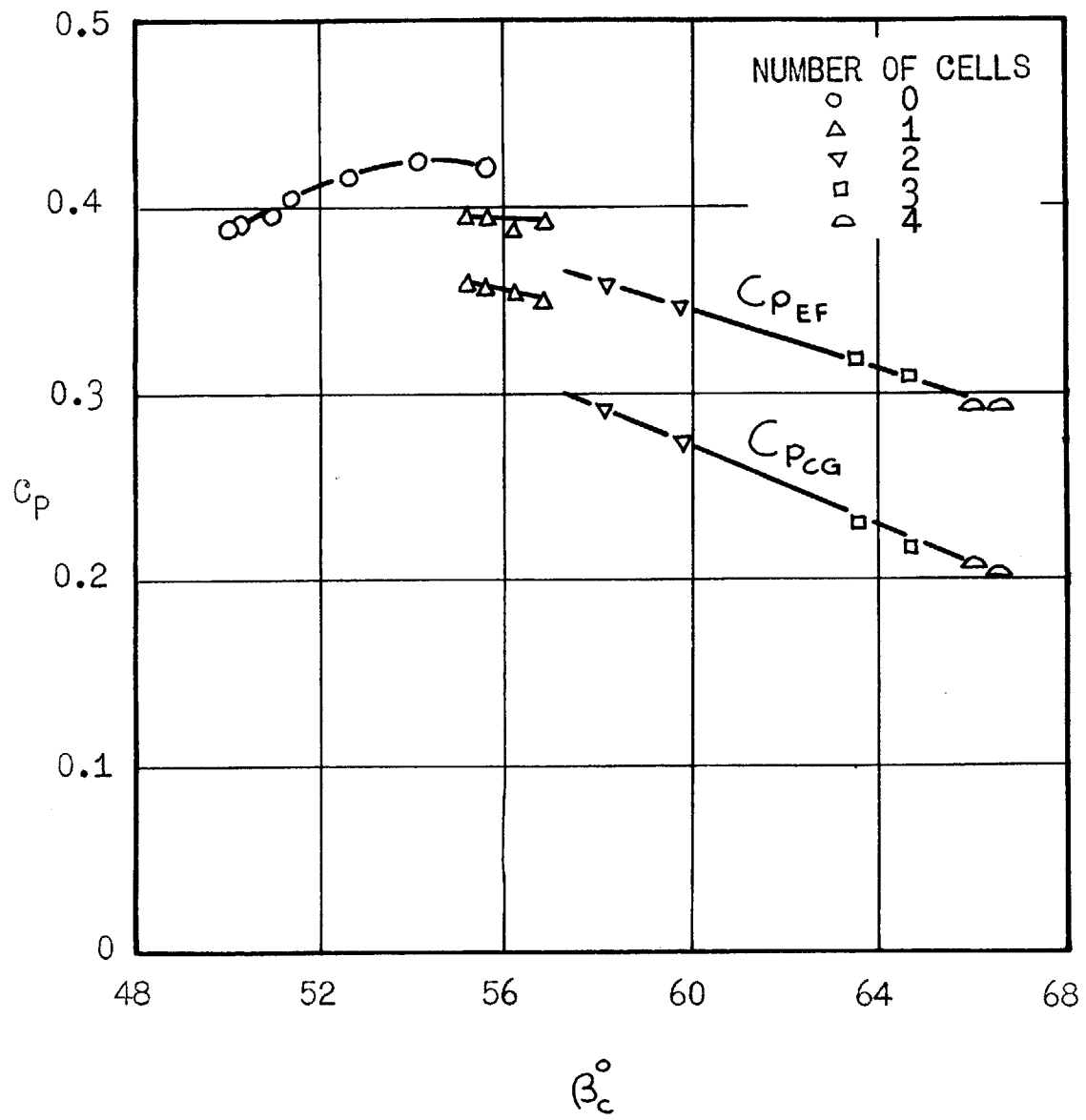
FIG. 45   PRESSURE COEFFICIENT VS β_c -CONFIGURATION A

FIG. 46   PROPAGATION VELOCITY VS β_c -CONFIGURATION A

NUMBER OF CELLS 1   2   3   4   4

β_c° 55.8   59.8   63.1   66.6   70.3
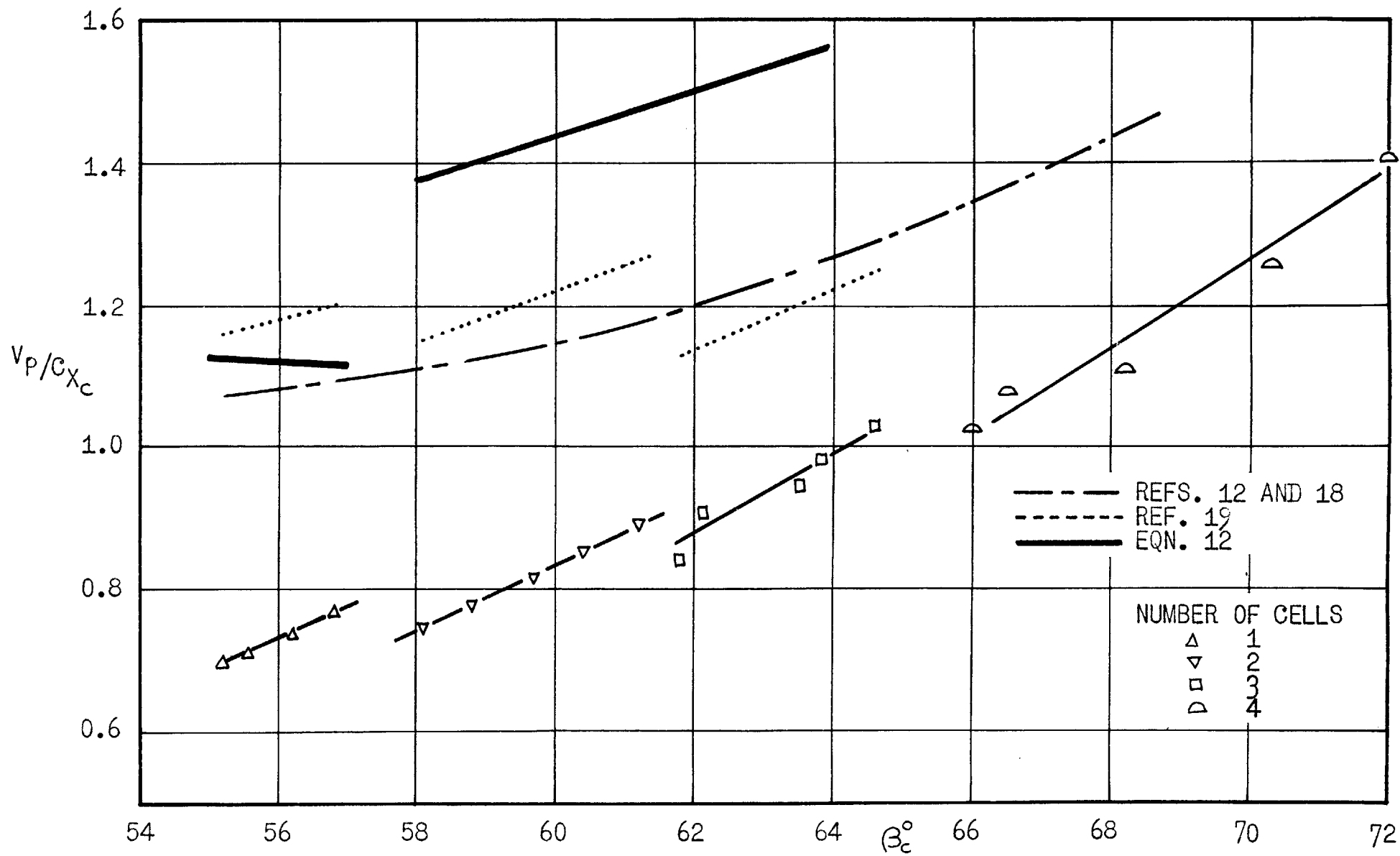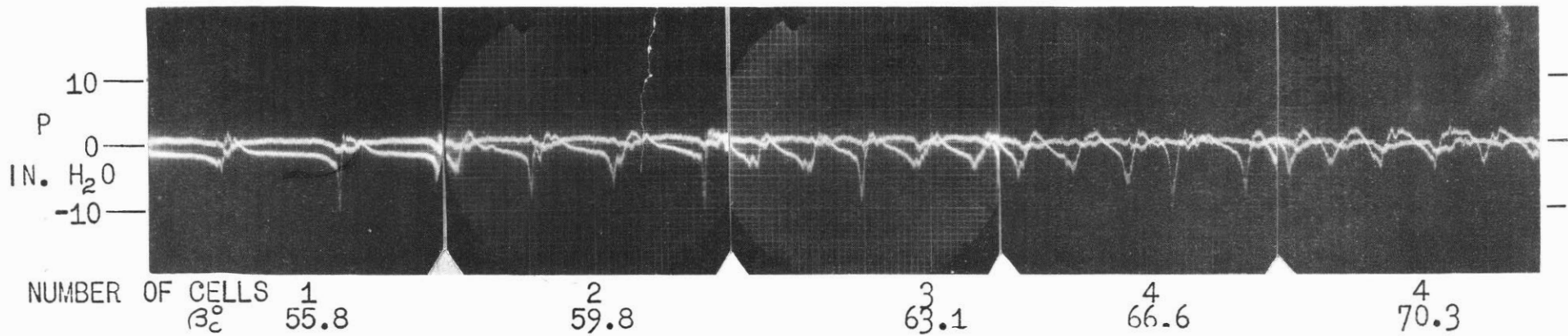
FIG. 47   STATIC PRESSURE AT OUTER WALL-CONFIGURATION A
UPPER TRACE AT STATION FG, LOWER AT E   TIME →

NUMBER OF CELLS 1   2   3   4   4

β_c° 56.7   60.1   63.4   67.3   71.0
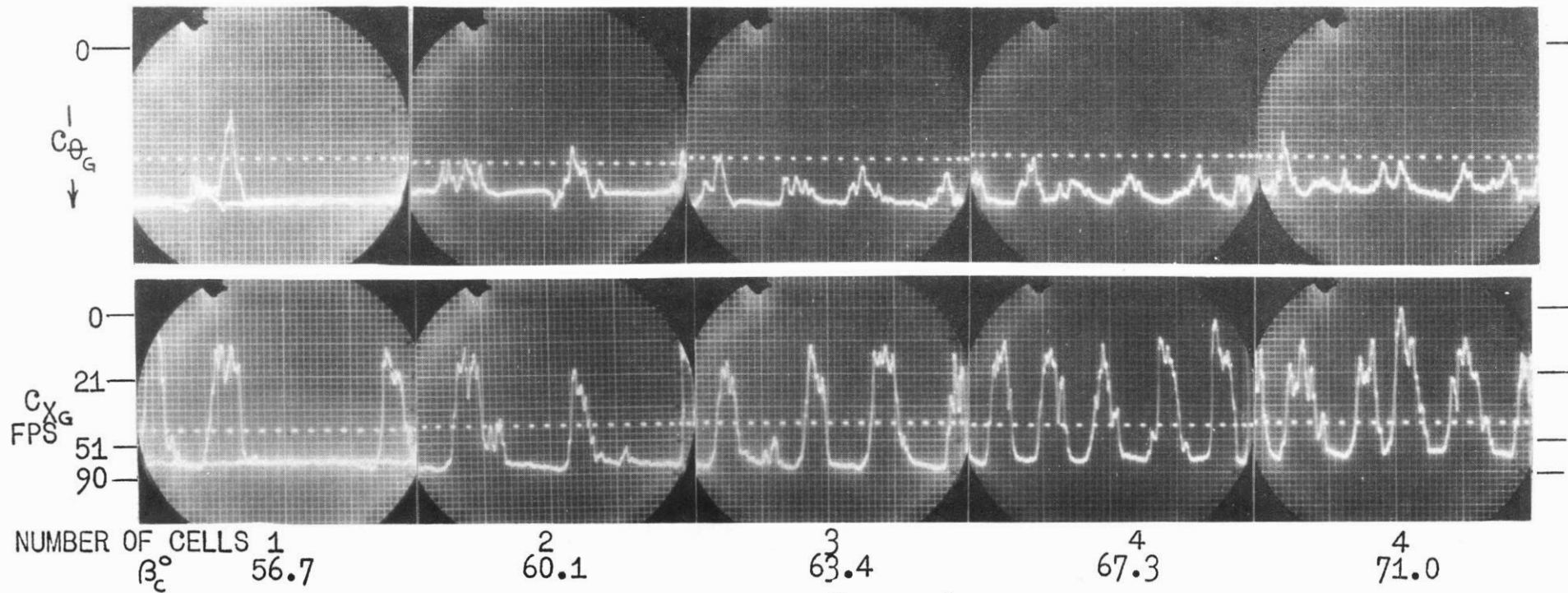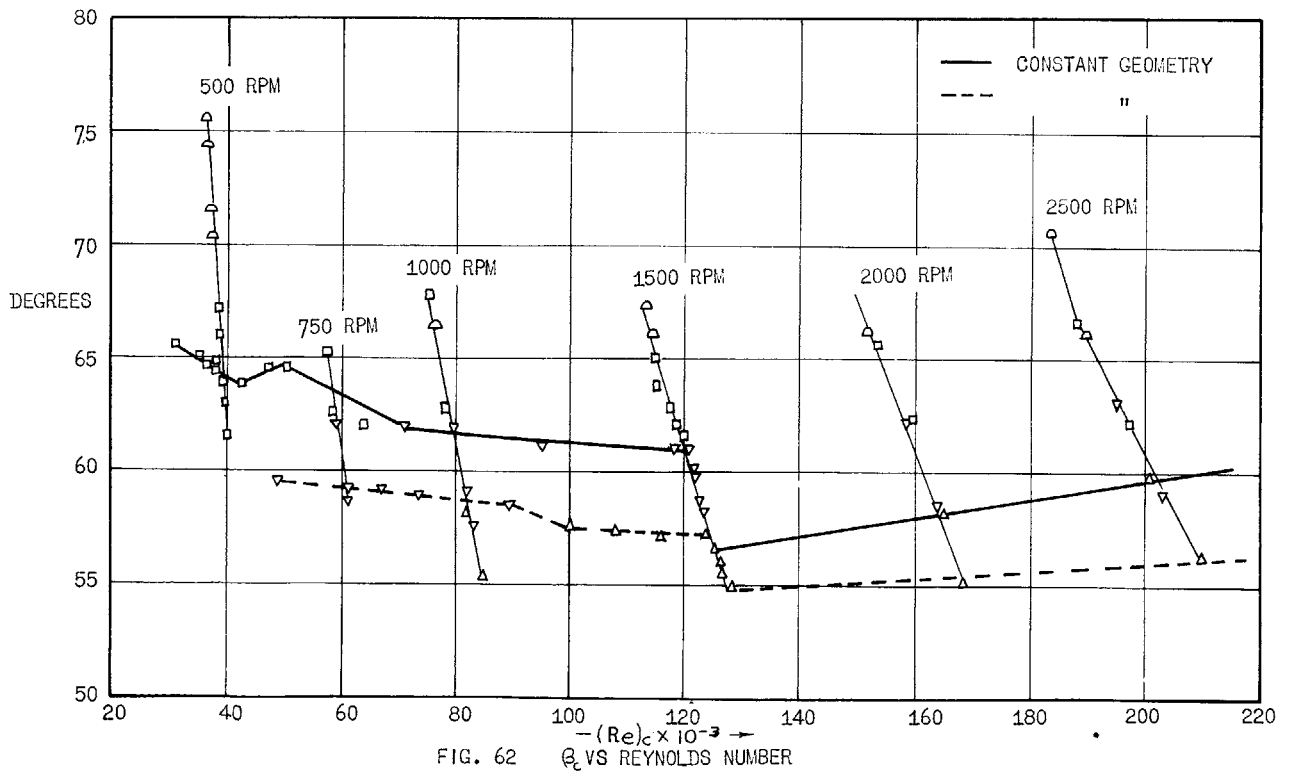
FIG. 48   HOT WIRE TRACES OF C_{X_G} AND C_{θ_G} -CONFIGURATION A
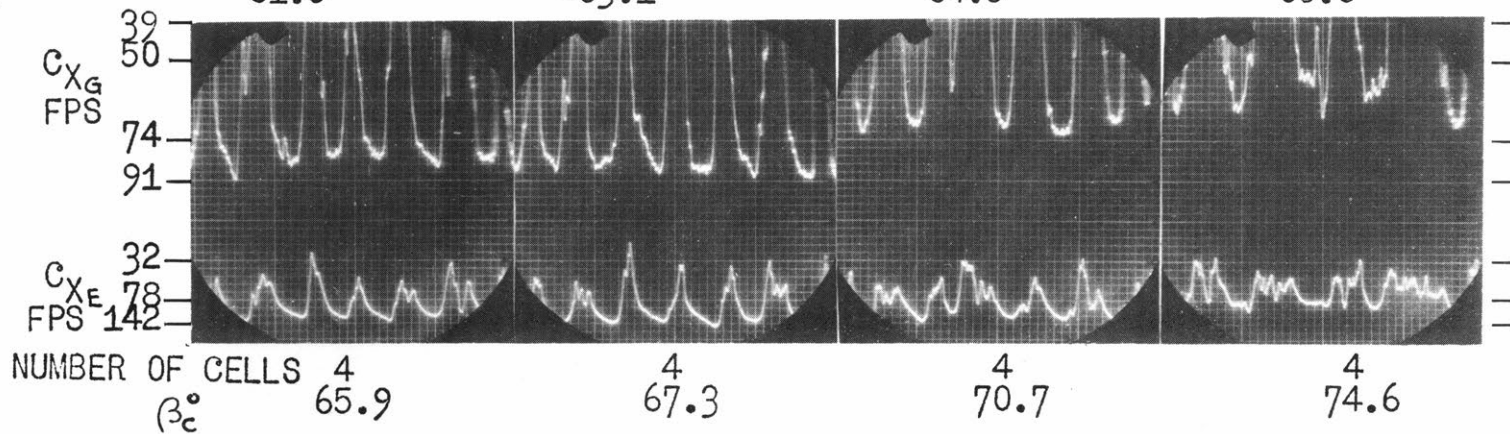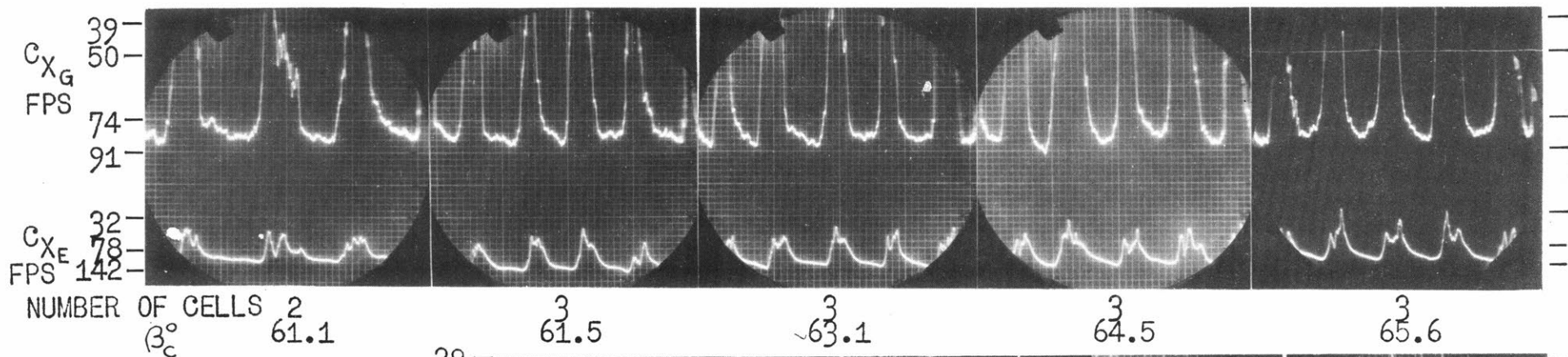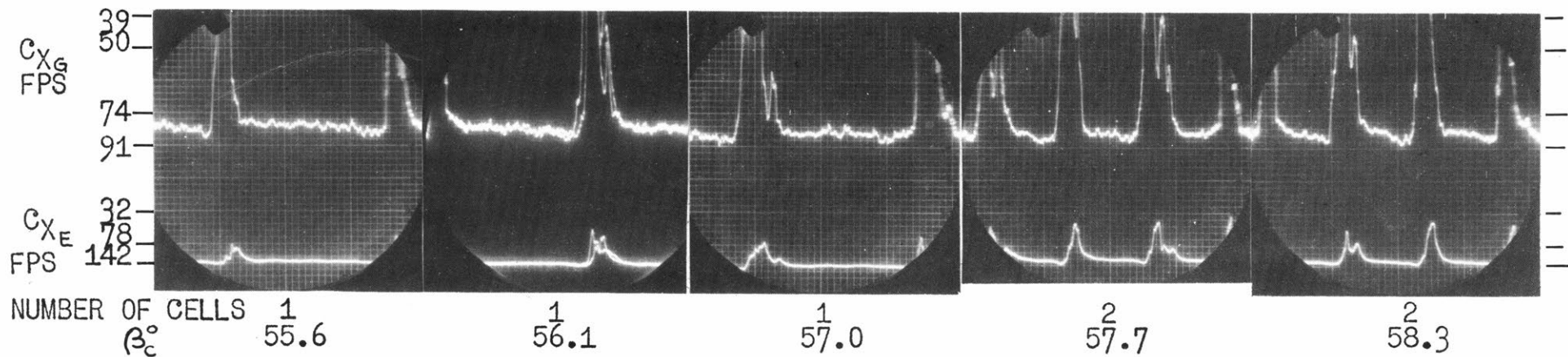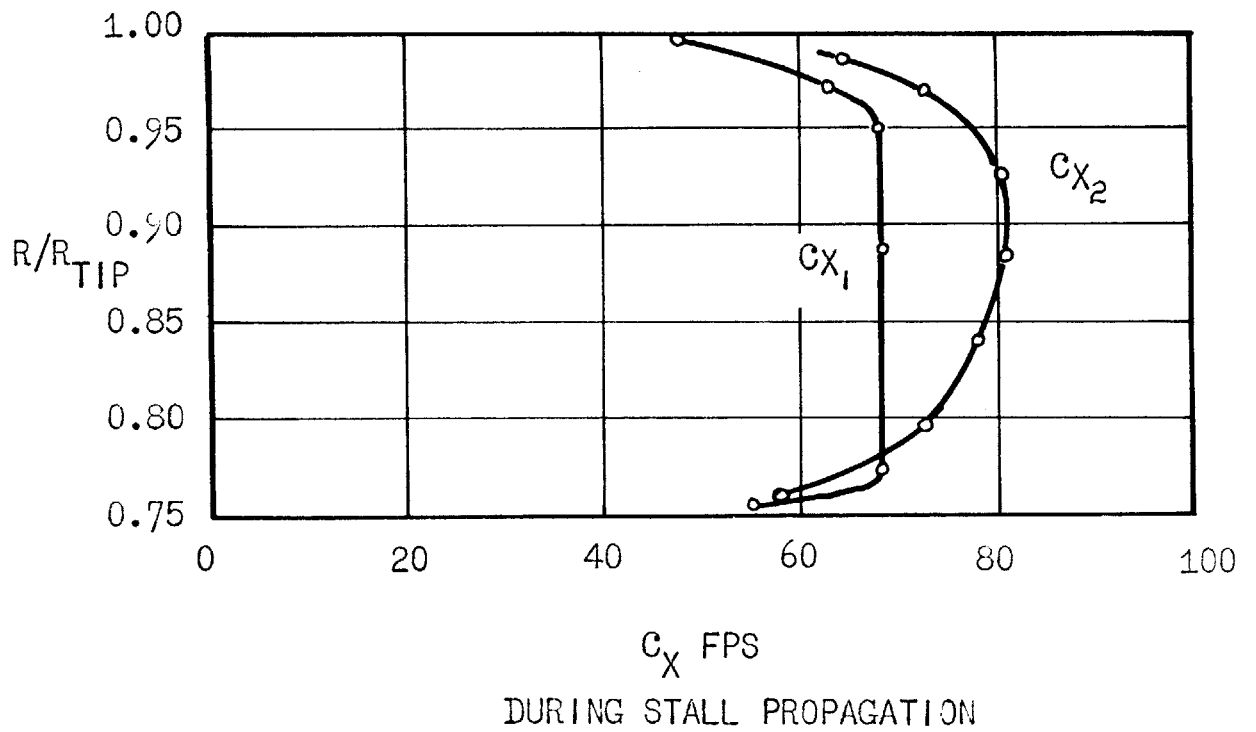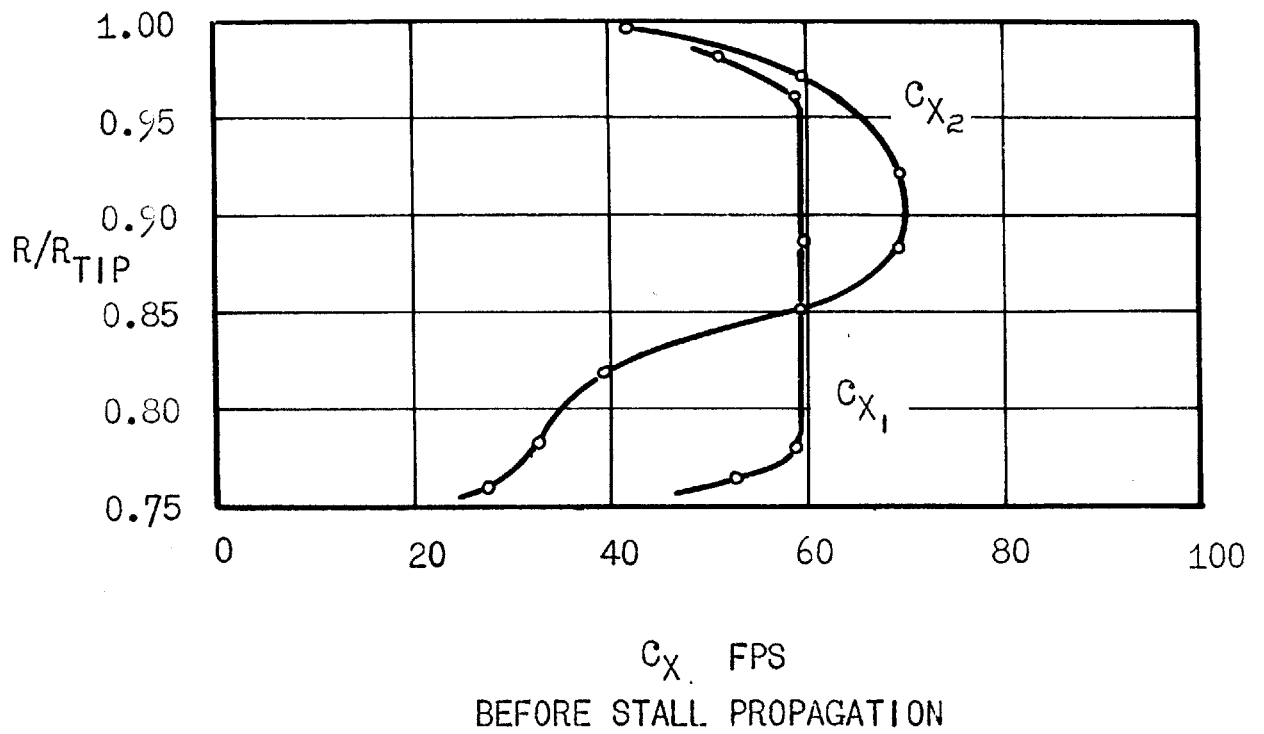
FIG. 49

HOT WIRE TRACES OF C_X
CONFIGURATION A
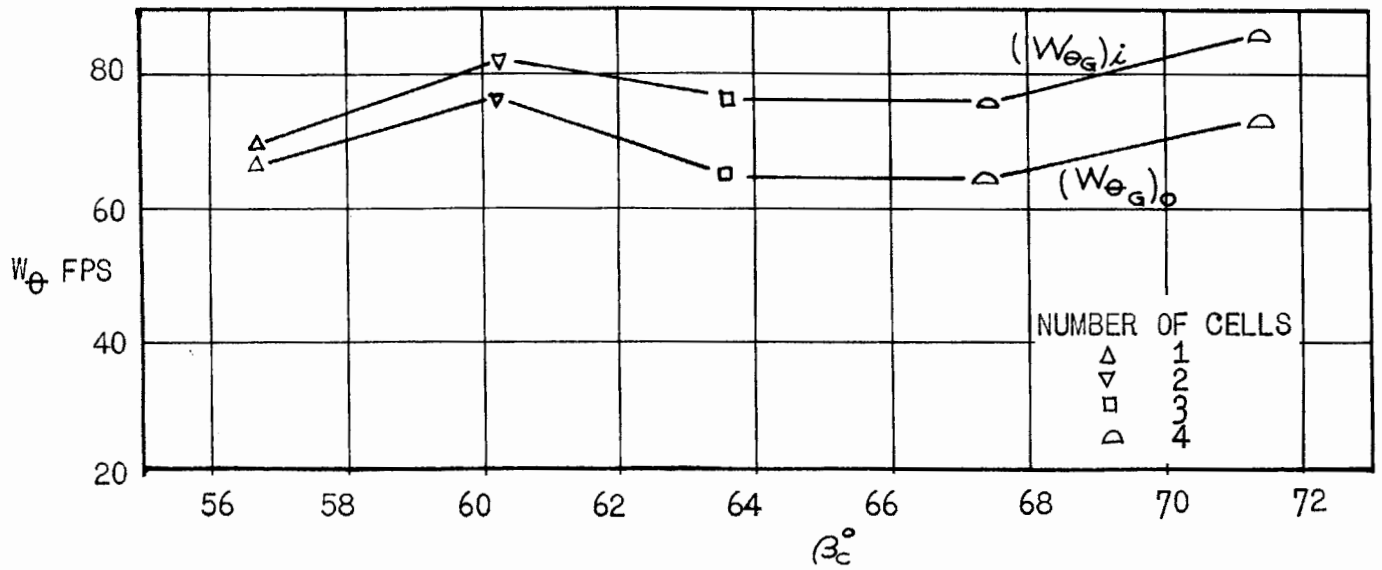
FIG. 50   VELOCITY COMPONENTS VS β_c —CONFIGURATION A
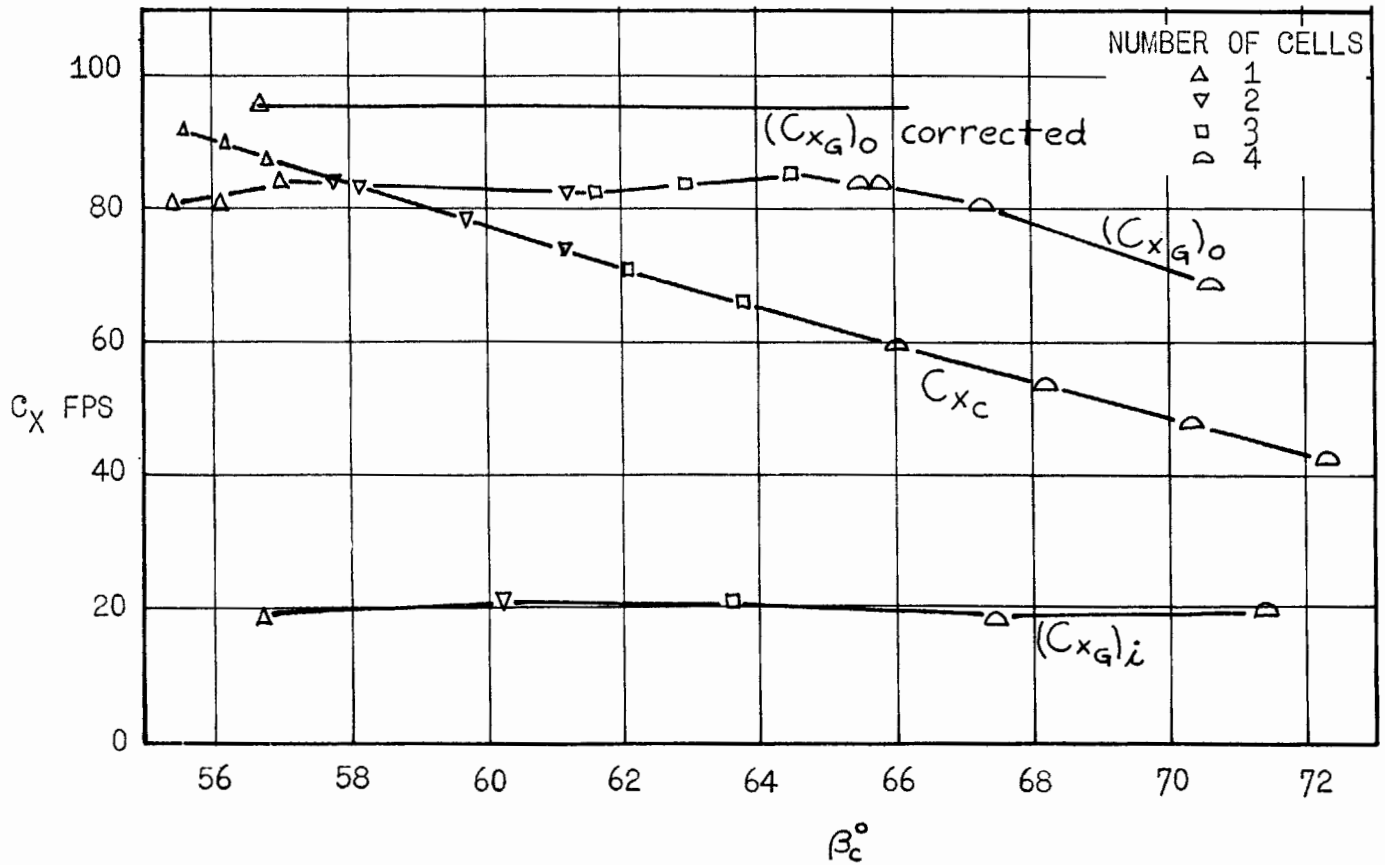
FIG. 51   VELOCITY COMPONENTS VS β_c —CONFIGURATION A
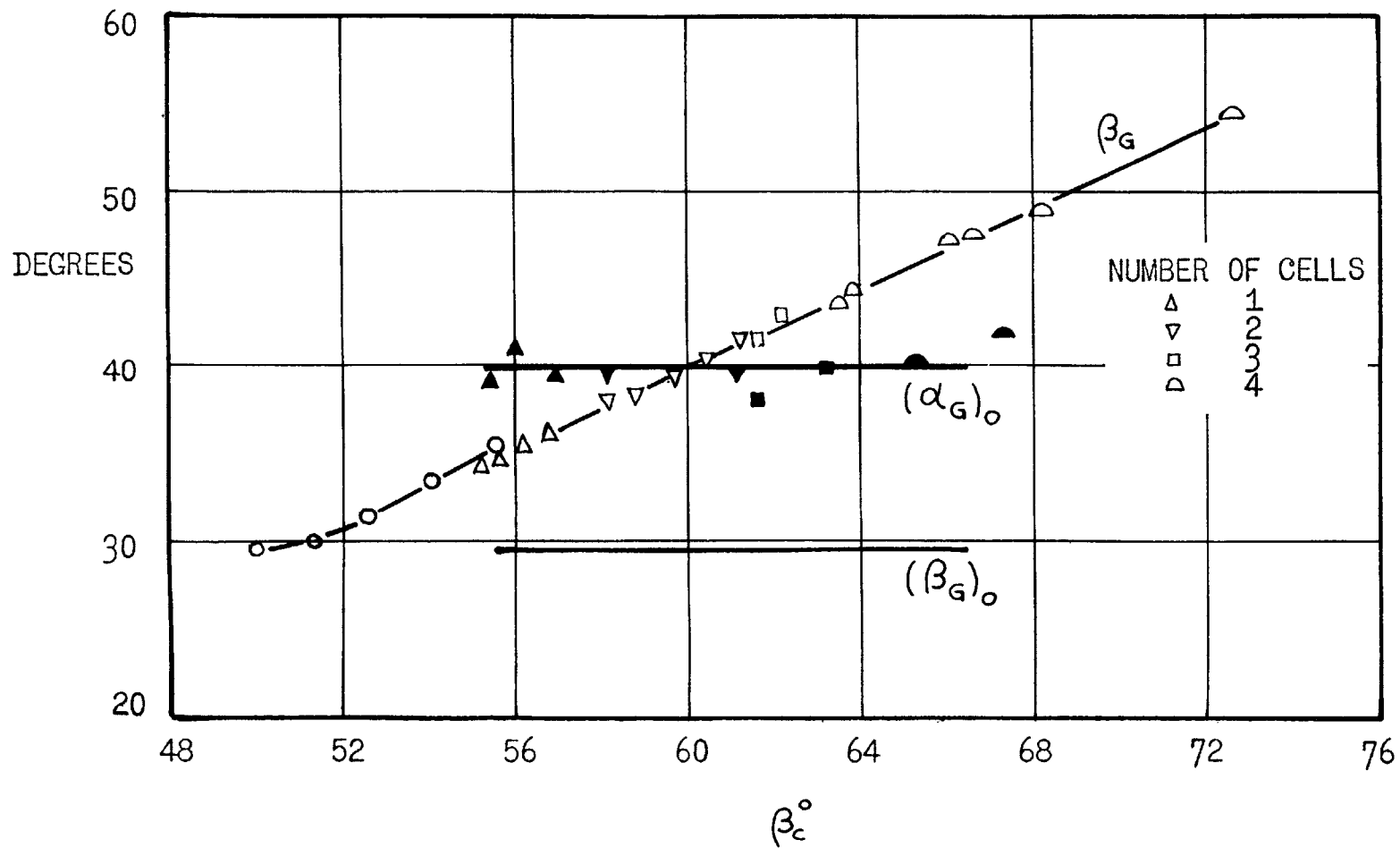
FIG. 52 FLOW ANGLES VS β_c —CONFIGURATION A
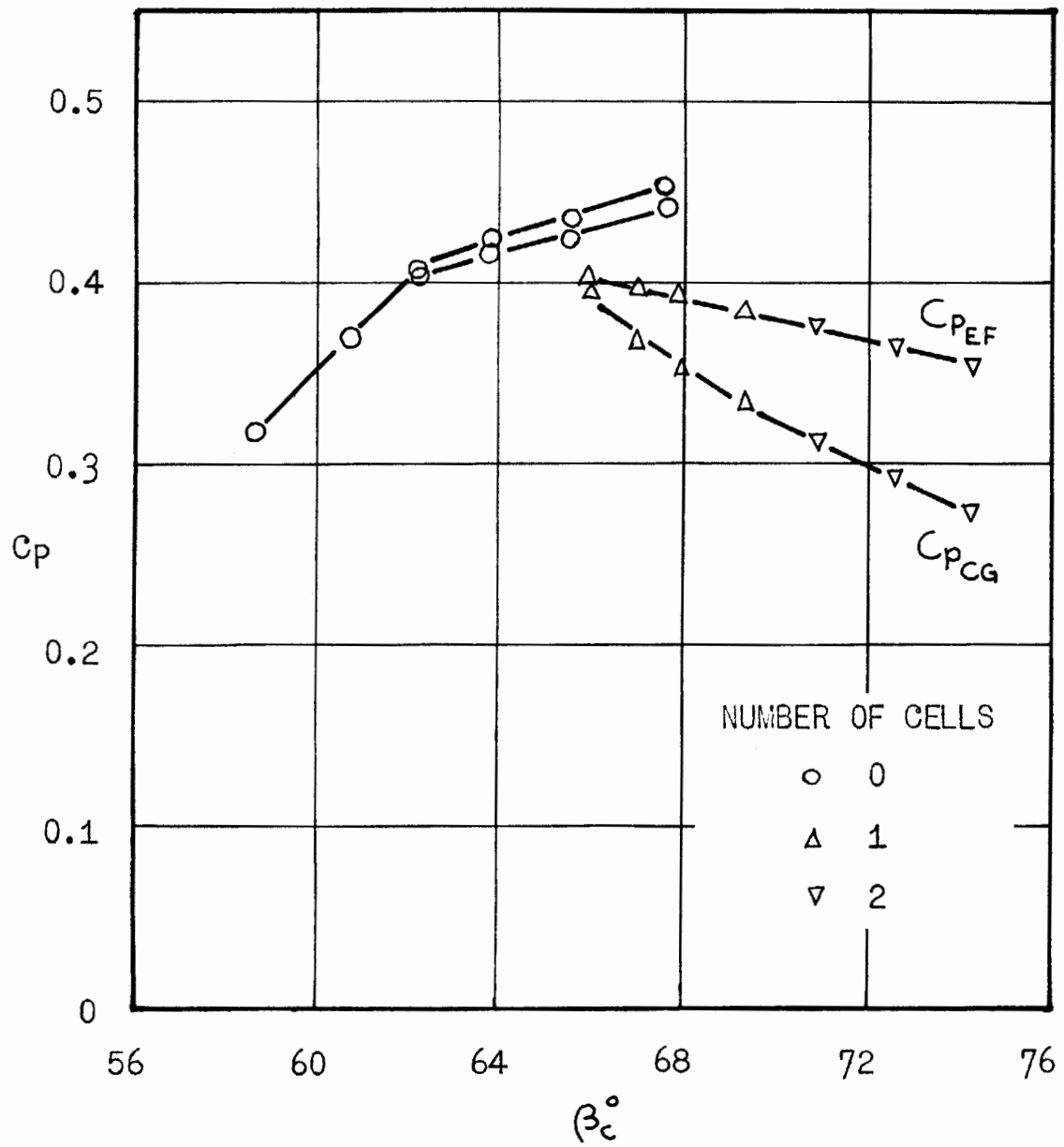
FIG. 53   PRESSURE COEFFICIENT VS β_c -CONFIGURATION C
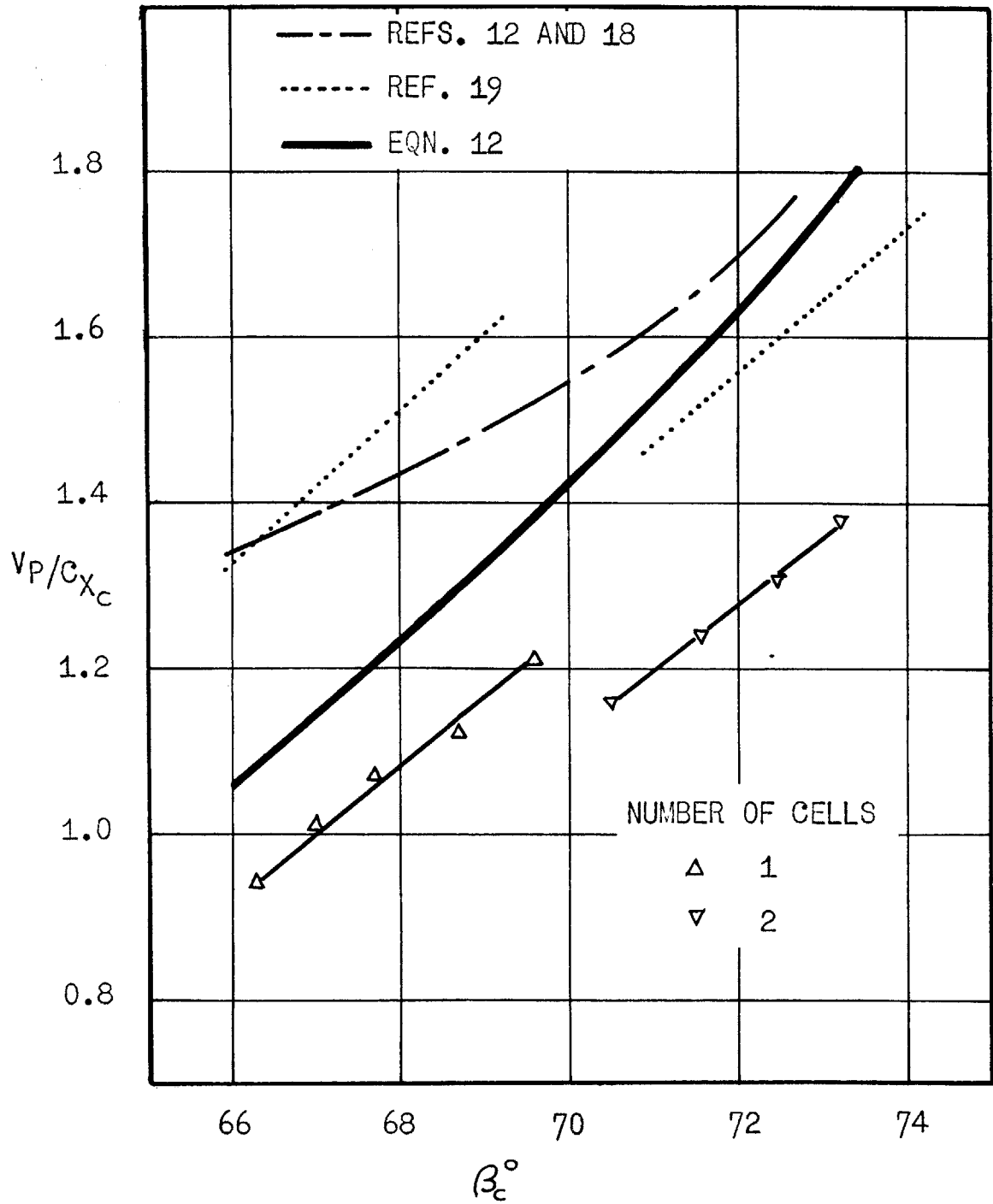
FIG. 54   PROPAGATION VELOCITY VS β_c -CONFIGURATION C
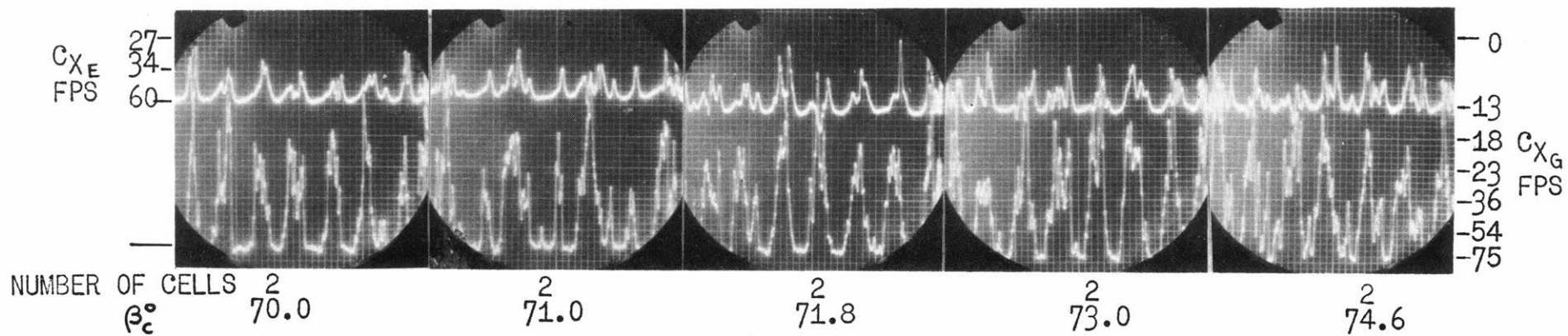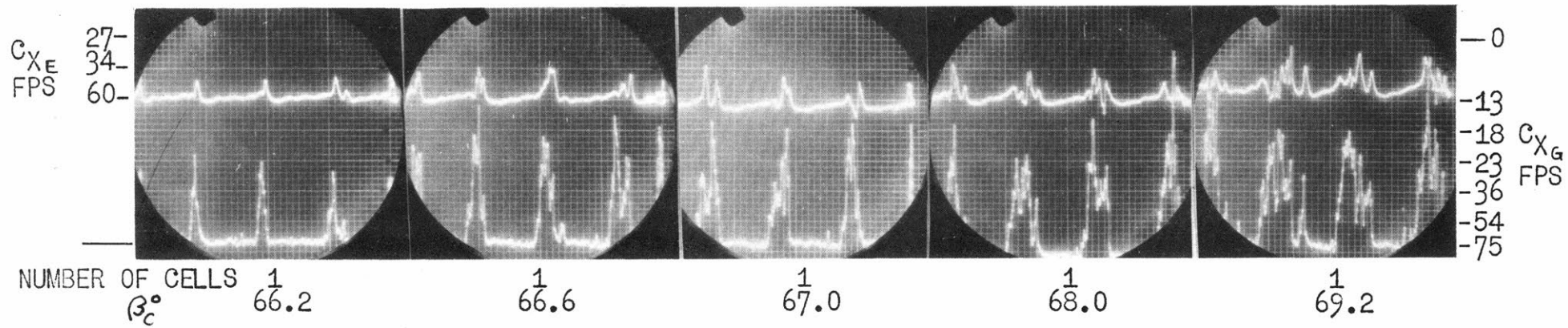
FIG. 55   HOT WIRE TRACES OF C_X-CONFIGURATION C
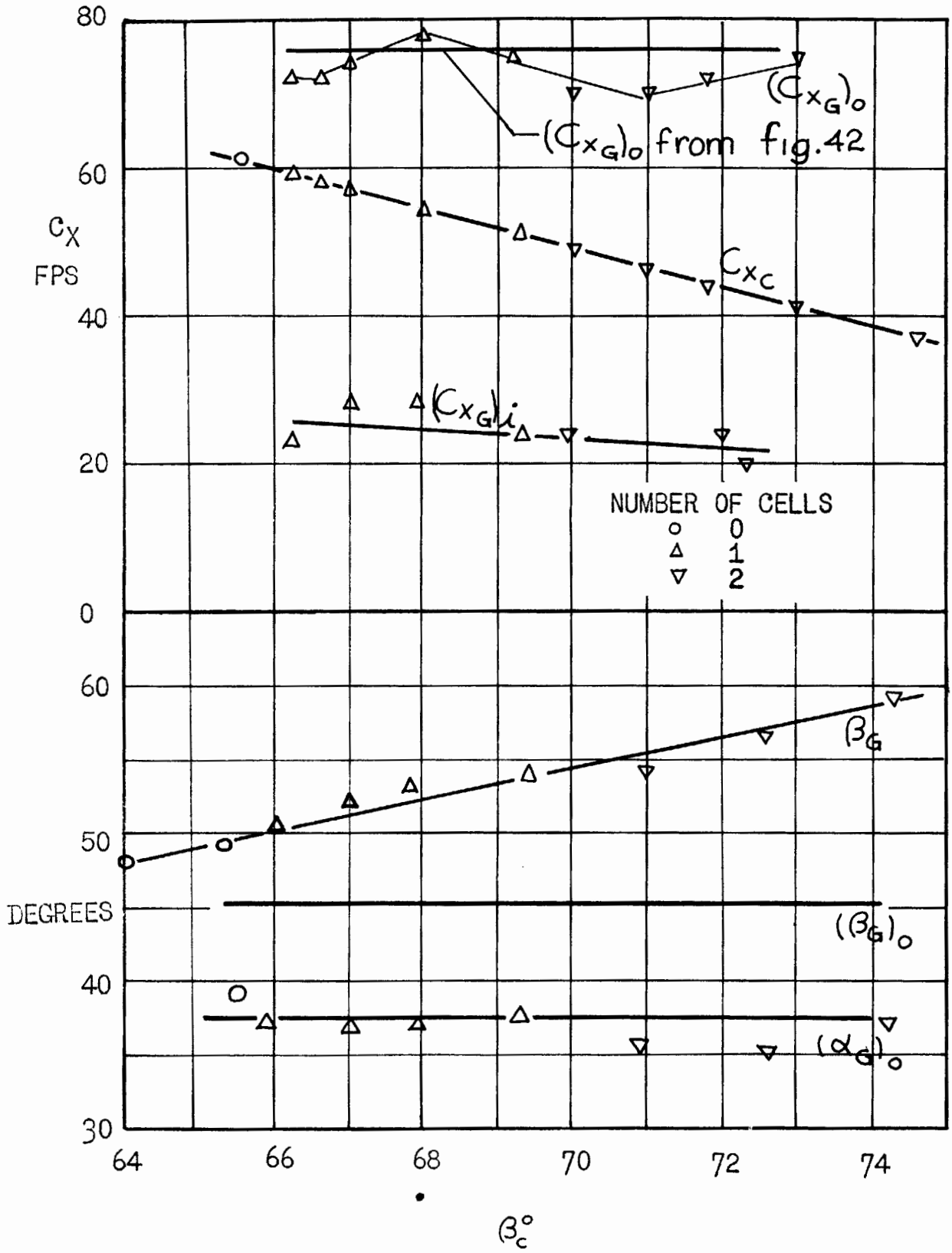
FIG. 56

VELOCITY COMPONENTS AND FLOW ANGLES VS β_c —CONFIGURATION C

HUB   MEAN RADIUS   TIP
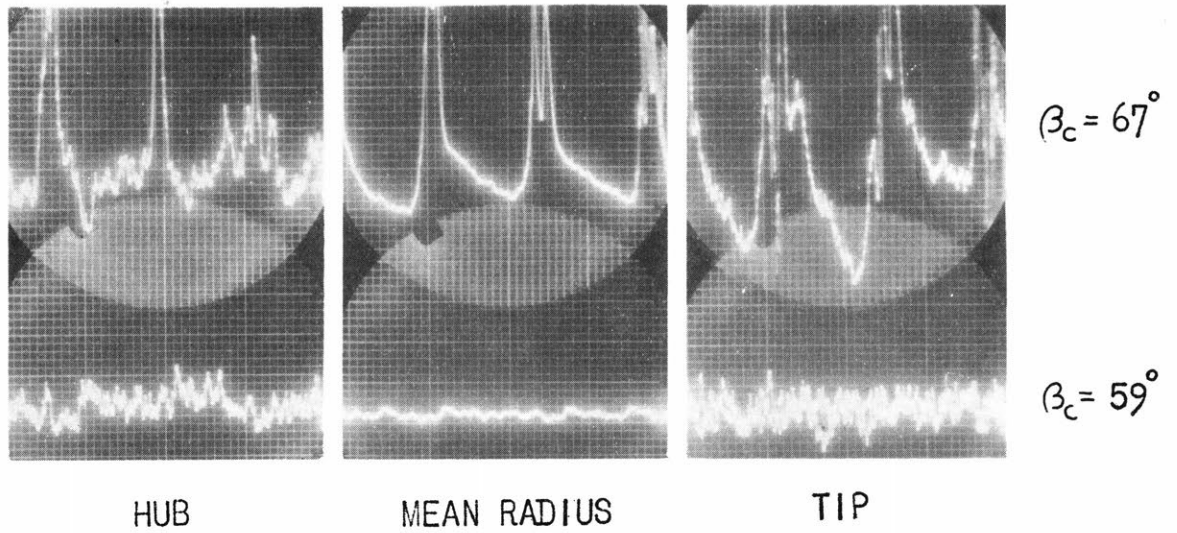
FIG. 57   HOT WIRE TRACES AT STATION E-CONFIGURATION C
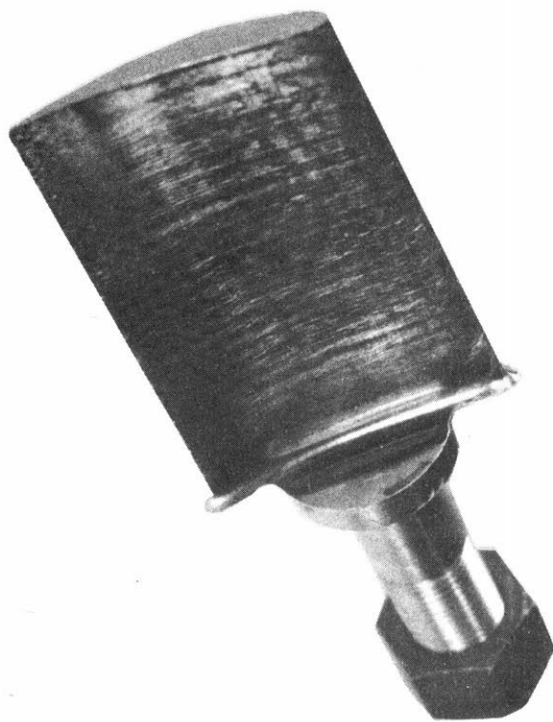
FIG. 58
PHOTOGRAPH OF ROTOR BLADE

FIG. 59   HOT WIRE TRACES OF C_X
CONFIGURATION A

NUMBER OF CELLS

○ 500 RPM	△ 1
● 1500 RPM	▽ 2
♀ 2500 RPM	▢ 3
	◠ 4

FIG. 60 V_P/C_{X_c} VS β_c FIG. 61 V_Q/U VS β_c

CONSTANT GEOMETRY
                    "

FIG. 62 β_c VS REYNOLDS NUMBER

c_X FPS

BEFORE STALL PROPAGATION

c_X FPS

DURING STALL PROPAGATION
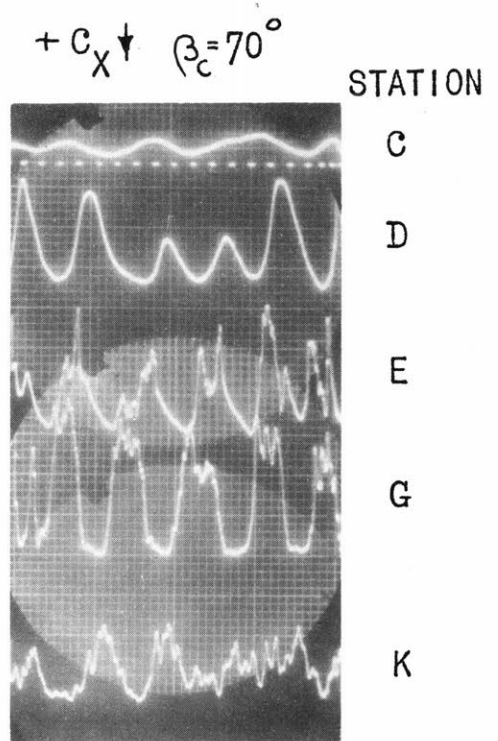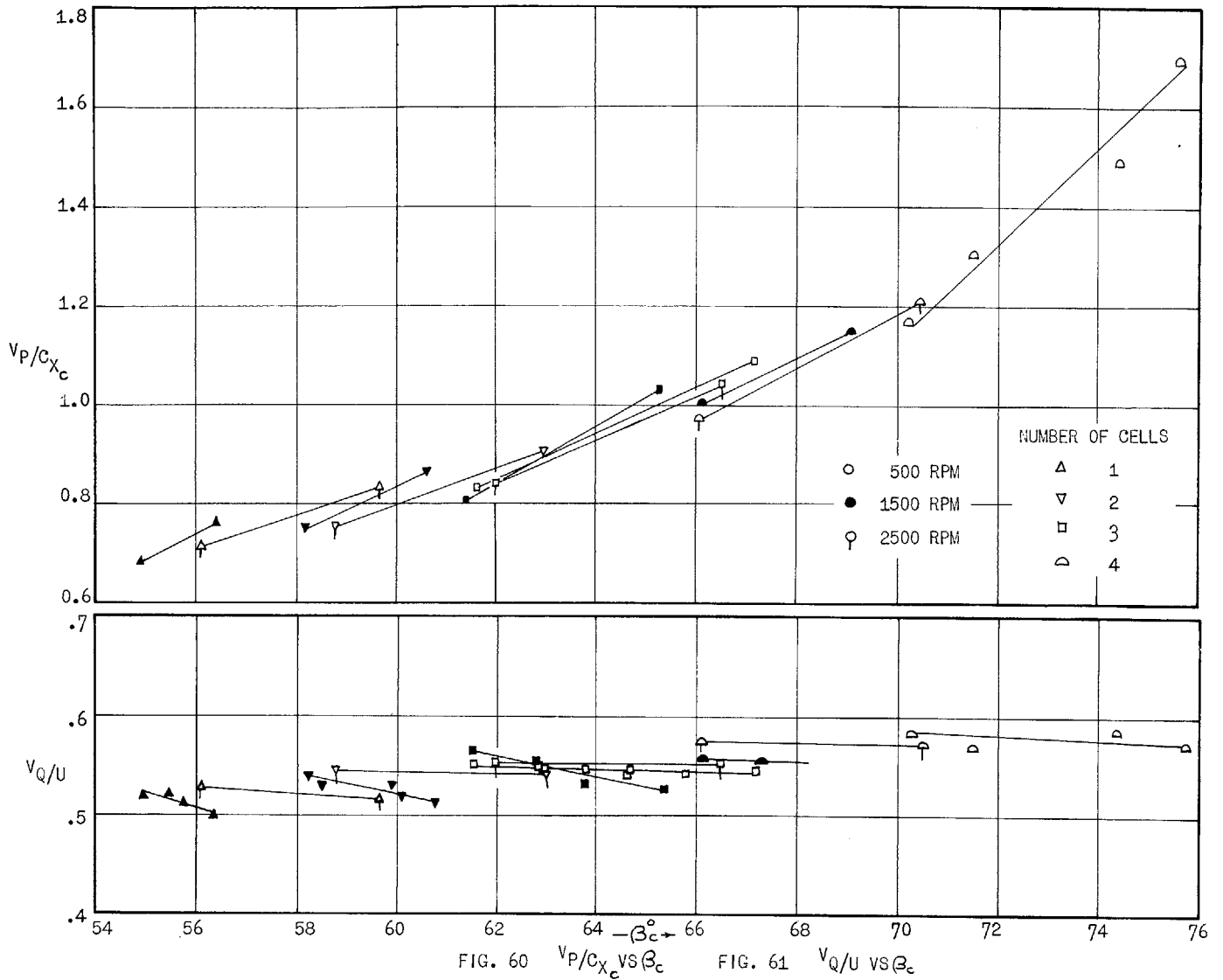
FIG. 63

VELOCITY PROFILES BEFORE AND AFTER ROTOR-CONFIGURATION C
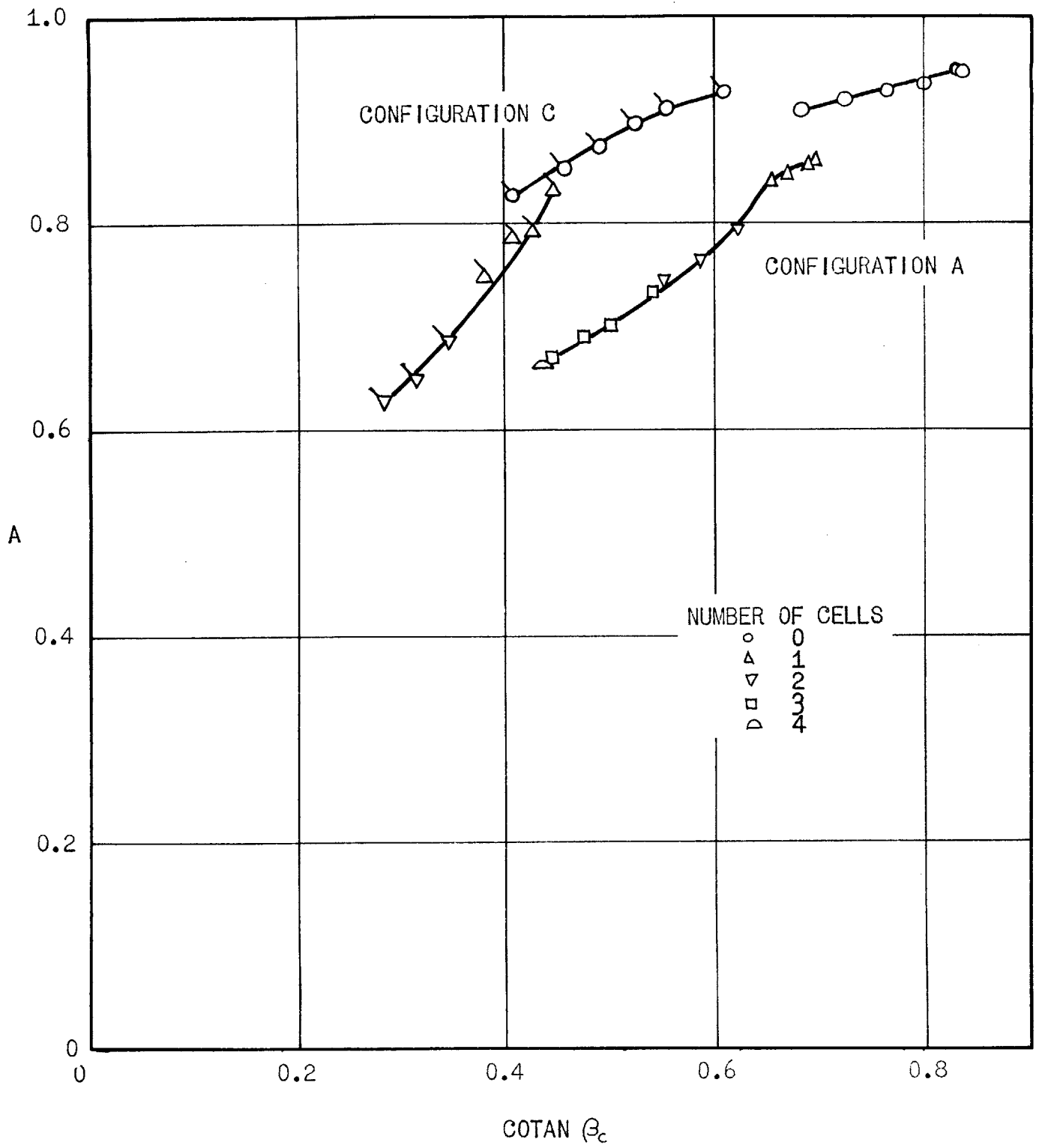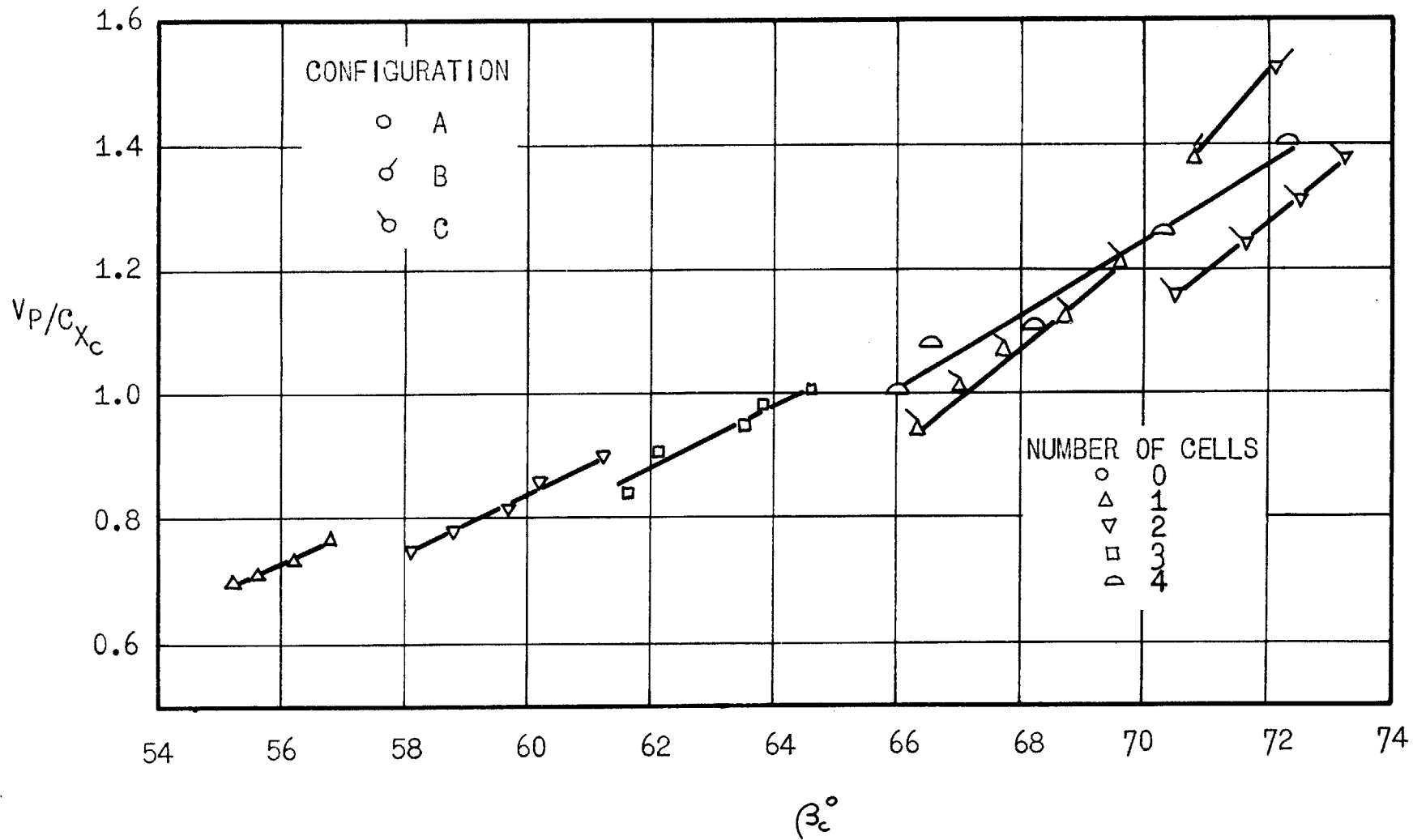
FIG. 64   DISCHARGE COEFFICIENT A VS COTAN β_c

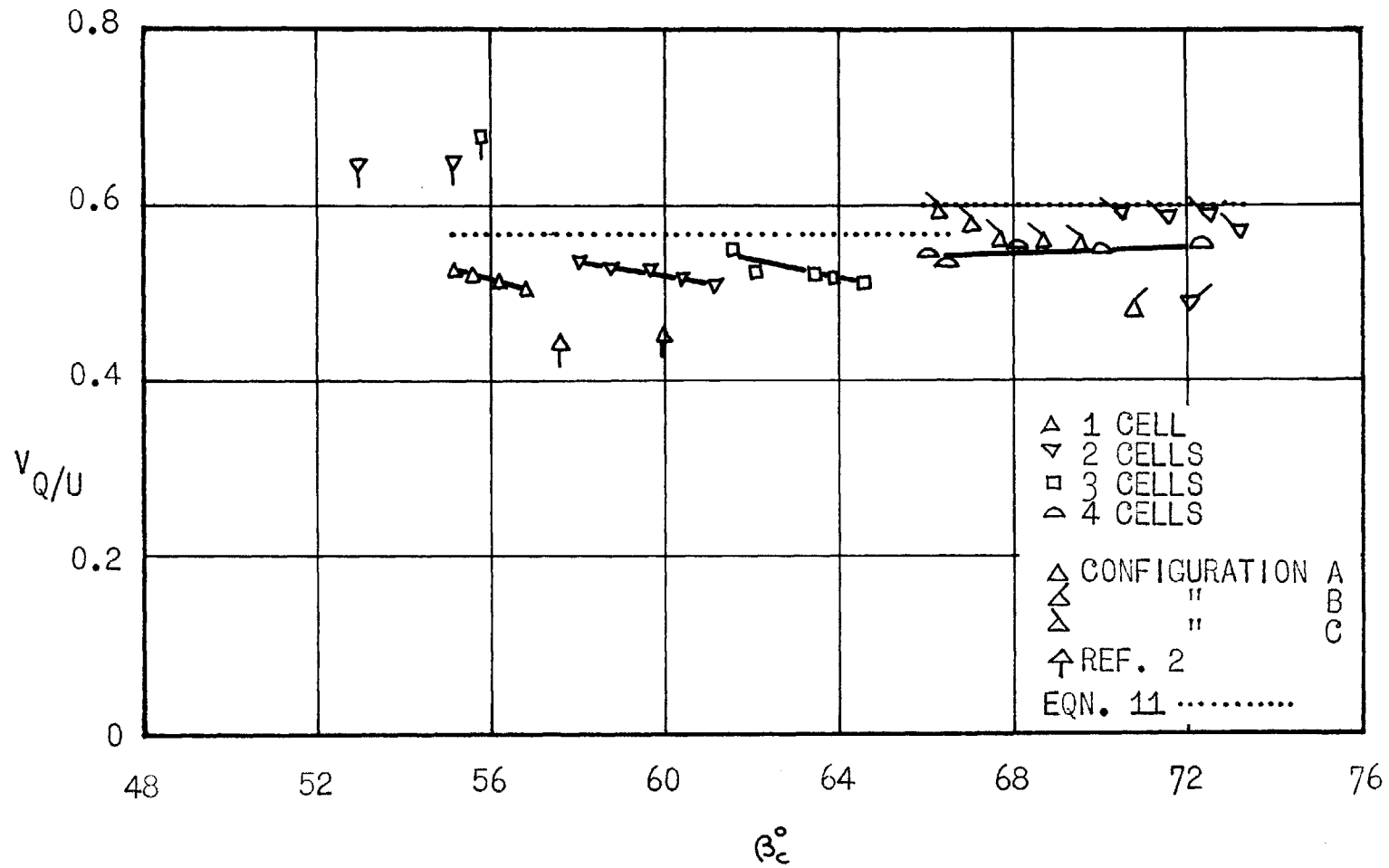FIG. 65   PROPAGATION VELOCITY VS β_c

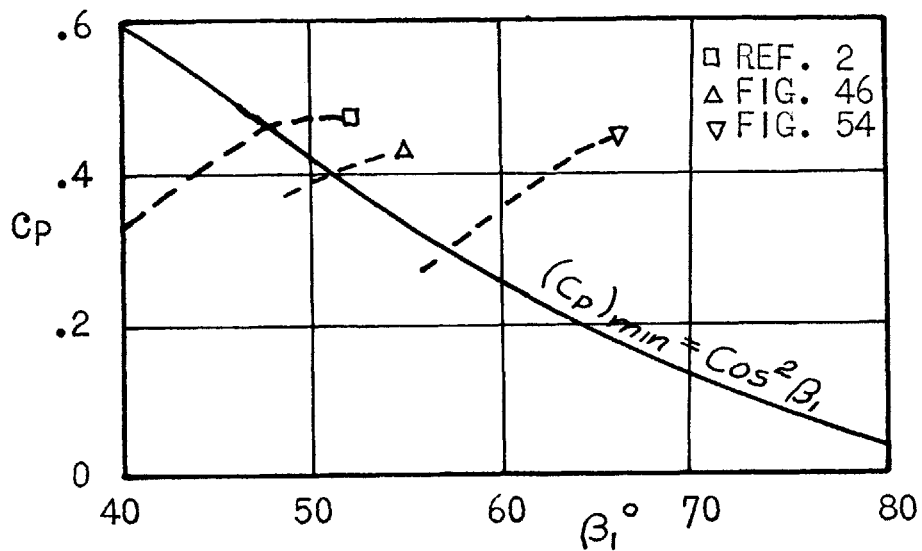FIG. 66   PROPAGATION VELOCITY VS β_c
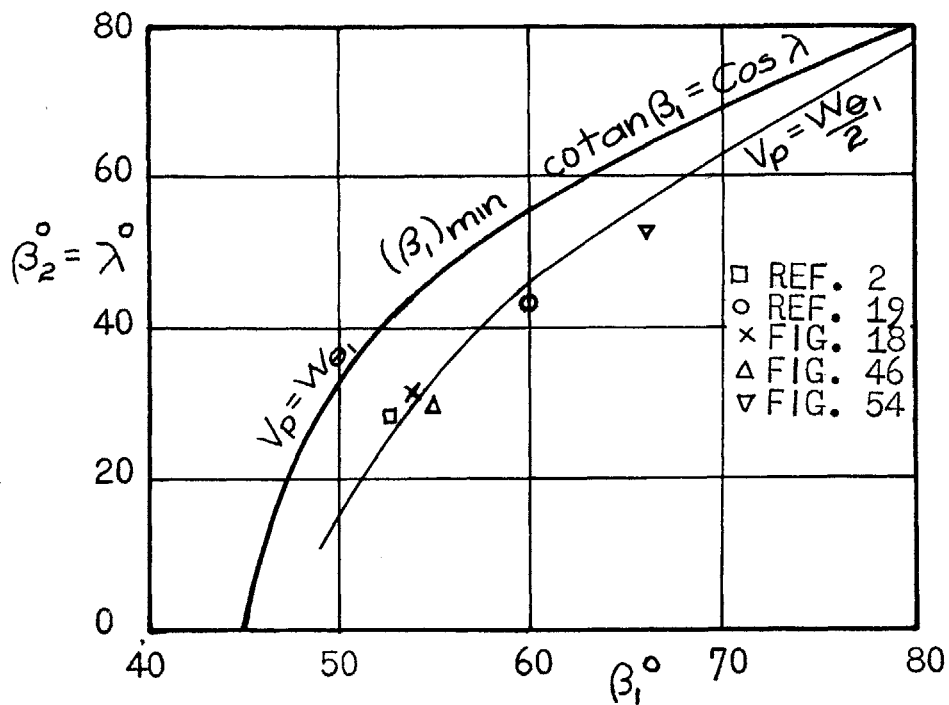
FIG. 67   MINIMUM c_p FOR STALL PROPAGATION VS β_1

FIG. 68   MINIMUM β_1 FOR STALL PROPAGATION VS λ